

# Analytical linear theory for the interaction of a planar shock wave with an isotropic turbulent vorticity field

J. G. Wouchuk\* and C. Huete Ruiz de Lira

*ETSII, Instituto de Investigaciones Energéticas (INEI), Universidad de Castilla La Mancha, Campus s/n, 13071 Ciudad Real, Spain*

A. L. Velikovich

*Plasma Physics Division, Naval Research Laboratory, Washington, DC 20375, USA*

(Received 13 February 2009; revised manuscript received 1 May 2009; published 26 June 2009)

An exact analytical model for the interaction between an isolated shock wave and an isotropic turbulent vorticity field is presented. The interaction with a single-mode two-dimensional (2D) divergence-free vorticity field is analyzed in detail, giving the time and space evolutions of the perturbed quantities downstream. The results are generalized to study the interaction of a planar shock wave with an isotropic three-dimensional (3D) or 2D preshock vorticity field. This field is decomposed into Fourier modes, and each mode is assumed to interact independently with the shock front. Averages of the downstream quantities are made by integrating over the angles that define the orientation of the upstream velocity field. The ratio of downstream/upstream kinetic energies is in good agreement with existing numerical and experimental results for both 3D and 2D preshock vorticity fields. The generation of sound and the sonic energy flux radiated downstream from the shock front is also discussed in detail, as well as the amplification of transverse vorticity across the shock front. The anisotropy is calculated for the far downstream fields of both velocity and vorticity. All the quantities characteristic of the shock-turbulence interaction are reduced to closed-form exact analytical expressions. They are presented as explicit functions of the two parameters that govern the dynamics of the interaction: the adiabatic exponent  $\gamma$  and the shock Mach number  $M_1$ . These formulas are further reduced to simpler exact asymptotic expressions in the limits of weak and strong shock waves ( $M_1 - 1 \ll 1$ ,  $M_1 \gg 1$ ) and high shock compressibility of the gas ( $\gamma \rightarrow 1$ ).

DOI: [10.1103/PhysRevE.79.066315](https://doi.org/10.1103/PhysRevE.79.066315)

PACS number(s): 47.40.Nm, 47.27.Sd, 47.20.Ma

## I. INTRODUCTION

The study of the interaction of planar shock waves with flow inhomogeneities dates back to more than fifty years, and a vast amount of experimental and theoretical work has been accumulated since then [1–52]. Without intending to be exhaustive, we usually recognize two general types of interactions: a planar shock wave may hit a localized perturbation at a material interface separating two homogeneous fluids, triggering the well-known Richtmyer-Meshkov instability (RMI) [7,8,10,11,48–52], or the shock wave may propagate into a weakly nonuniform fluid. In this latter case, the preshock perturbations may consist of sound waves [18], density inhomogeneities [19,23,44–47], or velocity/vorticity perturbations [12–21]. In either case, the initially planar shock front gets rippled as it propagates into the nonuniform fluid, generating additional vorticity, entropy, and sonic perturbations [37]. To conserve mass, momentum, and energy, the corrugated shock will generate sound pressure waves downstream that may behave as evanescent waves or escape from the shock front as traveling waves. The entropy and vorticity perturbations would remain frozen to the fluid elements. This type of problems is of fundamental importance in fluid dynamics as it appears in several fields, such as inertial confinement fusion [23], astrophysics [36,46], and turbulence research [30–33,35]. In this work we study the interaction of a planar shock wave that enters a half-space

filled with random rotational and divergence-free velocity perturbations (see Fig. 1).

The shock/turbulence interaction problem has been pioneered with the analytical works of Ribner and others [12–28], who decomposed the weak turbulent field ahead of the shock front as a Fourier superposition of infinitely small statistically independent single-mode shear waves. Each of these modes, interacting with the shock front, generates behind it a combination of vortical, entropic, and sonic perturbation eigenmodes. The transfer functions, which determine the amplitudes of these postshock eigenmodes for the given amplitude of the incident shear wave, depend on the angle  $\theta$

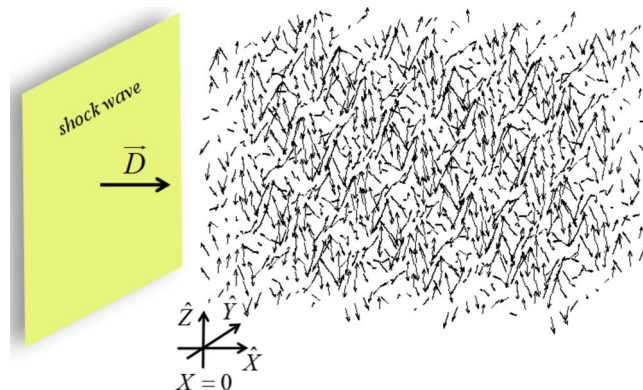


FIG. 1. (Color online) A planar shock moving with velocity  $D\hat{X}$  in the laboratory reference frame, hits a turbulent velocity field located in the half-space  $X \geq 0$ .

\*gustavo.wouchuk@uclm.es

between the wave vector  $\vec{k}$  of the perturbation mode in the gas upstream and the normal  $\vec{n}$  to the shock front, the equation of state of the shocked medium (for the ideal-gas case expressed by the adiabatic exponent  $\gamma$ ), and the shock strength expressed by the Mach number  $M_1$ . For given values of  $\gamma$  and  $M_1$ , the result of the shock interaction with the whole spectrum of such modes could then be deduced by properly averaging the downstream quantities over the angle  $\theta$ .

In the pioneering Ribner's papers, the "rather cumbersome" [17] transfer functions of  $\theta$ ,  $\gamma$ , and  $M_1$  have been first tabulated for  $\gamma=7/5$  [14]. Then, these functions were used to calculate the amplification of the turbulent kinetic energy [16] and the generation of sound in shock-turbulence interaction [17] by averaging them over the angle  $\theta$ , which for the isotropic preshock turbulence required a single integration, performed numerically. These results have not been reduced to simplified analytical expressions in either weak-shock or strong-shock limit. In [17], Ribner proved the first weak-shock analytical asymptotic formula proposed by Lighthill [13] for sound emission in shock-turbulence interaction to be incorrect.

The renewed interest to shock-turbulence interaction in the last two decades was stimulated by the progress in inertial confinement fusion/high-energy-density physics and astrophysics (see [23,35,38] and references therein). Starting from the 1990s, the opportunities for direct numerical [19–21,28–33,36] and experimental [22,39,40] studies of shock-turbulence interaction emerged. It turned out then that practical use of Ribner's linear interaction analysis for comparison with the new results required re-derivation of his model, as done by the authors of [30–32]. Since few details of this new derivation have been published, it was not obvious even to Ribner himself whether or not this new linear model of shock-turbulence interaction was fully equivalent to his earlier one [42]: "*The LIA (linear interaction analysis) theory as reconstituted in Ref. [5] (our Ref. [30]) is somewhat ambiguous, and details are lacking.*" Other models have also been developed to deal with the amplification of the turbulent kinetic energy, among them the rapid distortion theory (RDT) by Jacquin *et al.* [41]. However, the authors themselves recognized the inadequacy of their treatment for the problem we consider in this article. As extracted from their conclusions [41]: "*Qualitative comparisons have been made with Ribner's LIA and DNS. They show that homogeneous RDT is not suited for predicting the kinetic-energy amplification in a free shock/turbulence interaction. It gives results very different from those given by Ribner's LIA. In particular, it leads to a large overestimation of the amplification at high Mach numbers. However, the theory developed here could be more compatible with other flow configurations in which noncontinuous compressions or expansions occur, e.g., in compression or expansion ramps or in underexpanded or overexpanded jets, in which RDT-like amplifications are observed.*" Other researchers, who did not re-derive Ribner's model on their own, apparently did not find predictions of the linear theory available, even though their work would have clearly benefited from comparison to it (e.g., see [19,35]). Such practical unavailability of an important theoretical instrument indicates a gap in the

literature on shock-turbulence interaction that our present article aims to close.

We present a complete analytical theory of shock interaction with a weak isotropic turbulent velocity field. The underlying physics is the same as in the model originally developed by Ribner [14–17] and later reconstituted in [30] (we demonstrate the equivalence by direct comparison). Similarly as in Ribner's analysis, we only consider the linear interaction between the shock wave front and the turbulent field in front of it. This assumption is justified by the fact that the velocity perturbations in the turbulent fluid before compression are assumed to be subsonic. The theoretical formulation is distinguished by the following important aspects. First, we used the analytical technique that has been developed over the last decade, and which has been shown to be successful in order to understand the linear dynamics of the RMI and related phenomena [23,48,50–52], to solve an initial-value problem, with a shock wave incident from a uniform fluid into a half-space containing a divergence-free vorticity field. We demonstrate how the asymptotic space and time periodicity is established for any single mode. At the same time, we describe the transient processes, most notably the Richtmyer-Meshkov instability growth at the interface separating the initially quiescent vorticity-free fluid from the turbulent zone. An exact expression for the asymptotic growth rate of this instability is presented. Second, all the results of our linear theory averaged over the isotropic preshock velocity field are derived as exact closed-form analytical solutions, expressed via elementary functions of  $\gamma$  and  $M_1$ . This analytical representation allows us to evaluate the amplification of turbulent kinetic energy, the postshock sonic energy flux, and other variables of interest in the whole range of variation in parameters  $1 \leq \gamma < \infty$  and  $1 \leq M_1 < \infty$ . Near the boundaries of this two-dimensional (2D) domain, our general analytical expressions are reduced to simple explicit formulas corresponding to the limiting cases of weak shock  $M_1 \rightarrow 1$ , strong shock  $M_1 \rightarrow \infty$ , and strong shock compressibility of the gas  $\gamma \rightarrow 1$ . Most of our results are given below for a realistic case of three-dimensional (3D) isotropic preshock turbulence. In a numerical simulation, one can also consider a 2D isotropic turbulence, with preshock and postshock vorticities parallel to the incident shock front, as done in [19]. We present formulas applicable to this 2D case, too. Our results confirm the accuracy of the numerical simulations done recently for both 3D [31,32] and 2D [19] preshock turbulence. They are also in agreement with the available experimental data [40]. Our model is exact, it contains no fitting parameters, and therefore it represents a convenient analytical tool, helpful for benchmarking of the existing or future hydrodynamic codes developed to model the interaction of shock fronts with flow inhomogeneities.

Formulas presented below refer to the variables, which are invariant with respect to the preshock-turbulence energy spectrum  $E(k)$ , such as the amplification coefficient of kinetic energy, sonic emission coefficient, and postshock anisotropy of velocity and vorticity. They can be readily applied to calculate the preshock to postshock transformation of spectrum, amplification of the average wave number, and other quantities, but these calculations, as well as many possible generalizations of our model, are beyond the scope of the present work.

The paper is structured as follows. In Sec. II, the basic blocks needed to construct the 2D single-mode model are presented and developed. Exact temporal evolution of the different perturbed quantities is shown since  $t=0+$ , and the explicit asymptotic expressions are derived. The generation of vorticity and sound waves downstream are discussed in detail. The RMI growth that ensues at the weak discontinuity formed at the boundary that separates the turbulent field with the initially quiescent fluid is described. In Sec. III, these results are used to calculate the quantities averaged over an either 3D or 2D isotropic preshock velocity distribution. Euler angles are used to represent the most general divergence-free velocity/vorticity field in front of the shock, in terms of elementary shear waves. This representation is greatly simplified by an adequate rotation on the plane of the shock to deal with the isotropic spectrum upstream. The ratio of the averages of the kinetic energy (downstream/upstream) are obtained either for a 3D or a 2D preshock turbulent vorticity field and are studied as explicit functions of the shock strength and the compressibility of the gas. The contribution of the sonic waves is also discussed in detail. The sound energy flux radiated into the fluid downstream is analyzed in both the compressed fluid reference and the shock front reference frames. An analysis of the amplification of the vorticity perturbations is presented. An anisotropy parameter is defined both for the downstream velocity and vorticity fields. It is found that the compressed velocity field may remain isotropic for specific choices of the two parameters that govern the dynamics of the interaction,  $\gamma$  and  $M_1$ , whereas the postshock vorticity field is always anisotropic. In Sec. IV we conclude with a summary. It is emphasized that all the line and surface plots shown in this work are generated using exact closed-form analytical formulas. Their complete expressions are given in the Appendices, which have been included in the auxiliary file attached to this work [57].

## II. INTERACTION OF A PLANAR SHOCK WITH A SINGLE-MODE 2D VORTICITY FIELD

### A. Boundary conditions

We refer to Fig. 2(a) where we consider a shock wave that comes from the left with velocity  $D\hat{x}'$ , as measured in the laboratory frame of reference (coordinates variables  $x'$  and  $y$ ). The fluid is an ideal gas, which is homogeneous for  $x' < 0$  and is only perturbed in the half-space  $x' > 0$  (see Fig. 1). Therefore, the surface located at  $x'=0$  is a weak contact discontinuity that separates two regions inside the same fluid [37]. The perturbations consist of steady-state, rotational, and divergence-free velocity fluctuations. In the space  $x' < 0$ , the velocity of the compressed fluid measured in the laboratory is  $U\hat{x}'$ , the density and pressure ahead of the shock are  $\rho_1$  and  $p_1$ , and their compressed values are  $\rho_2$  and  $p_2$ . The shock Mach number with respect to the fluid ahead of the shock is denoted by  $M_1$ , and that with respect to the compressed fluid by  $M_2$ . The sound speed ahead of the shock is  $c_1$ , and the compressed fluid sound speed is  $c_2$ . Before the shock arrives to the interface  $x'=0$ , the following relationships hold between the quantities at both sides of the shock front [37],

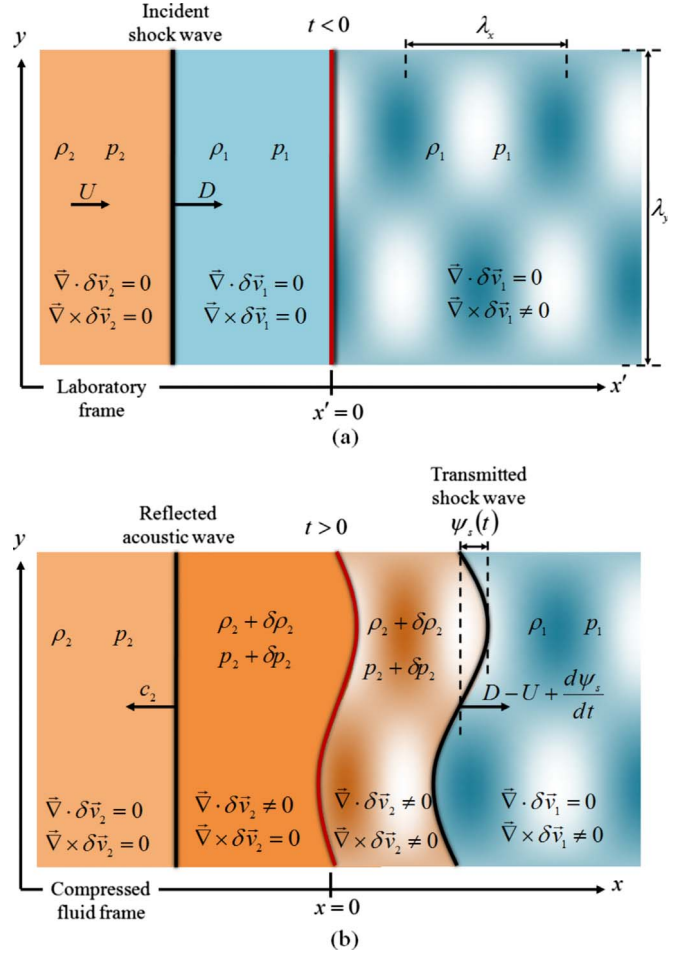


FIG. 2. (Color online) (a) The incident planar shock travels to the right in the laboratory system of reference with velocity  $D\hat{x}'$ . The fluid to the right of the surface  $x'=0$  has a rotational velocity perturbation field with no density disturbances. The situation is shown at  $t < 0$  in the laboratory frame of reference. (b) The transmitted shock front travels inside the perturbed fluid and the reflected sound wave travels to the left. The situation is shown for  $t > 0$  in the compressed fluid frame of reference.

$$R = \frac{\rho_2}{\rho_1} = \frac{D}{D-U} = \frac{(\gamma+1)M_1^2}{(\gamma-1)M_1^2+2}, \quad (1)$$

$$\frac{p_2}{p_1} = \frac{2\gamma M_1^2 - \gamma + 1}{\gamma + 1}, \quad (2)$$

$$\frac{c_2}{c_1} = \sqrt{\frac{2\gamma M_1^2 - \gamma + 1}{(\gamma+1)R}} = \frac{\sqrt{(2\gamma M_1^2 - \gamma + 1)[(\gamma-1)M_1^2 + 2]}}{(\gamma+1)M_1}, \quad (3)$$

$$M_2 = \frac{D-U}{c_2} = \sqrt{\frac{(\gamma-1)M_1^2 + 2}{2\gamma M_1^2 - \gamma + 1}}. \quad (4)$$

To the right of the surface  $x'=0$ , the perturbed velocity field is described by

$$v_{1x} = \delta v_{1x}(x', y) = c_2 u_1 \cos(k_x x') \cos(k_y y),$$

$$v_{1y} = \delta v_{1y}(x', y) = c_2 u_1 \frac{k_x}{k_y} \sin(k_x x') \sin(k_y y), \quad (5)$$

where “ $x'$ ” in the above two equations is the normal coordinate measured in the laboratory frame and  $u_1 = u_1(k_x, k_y)$  is a dimensionless parameter that quantifies the magnitude of the velocity perturbations. To remain within the limits of validity of the linear theory, we assume that  $u_1 \ll 1$ . It can be easily verified that the above velocity field is solenoidal ( $\nabla \cdot \delta \vec{v}_1 = 0$ ). The quantities  $k_x$  and  $k_y$  are the longitudinal and transverse wave numbers, defined as

$$k_x = \frac{2\pi}{\lambda_x}, \quad k_y = \frac{2\pi}{\lambda_y}, \quad (6)$$

where  $\lambda_x$  and  $\lambda_y$  are the characteristic longitudinal and transverse lengths of the vorticity profile upstream. The vorticity associated to the velocity components given by Eq. (5) is

$$\delta \omega_1(x', y) = k_y c_2 u_1 \left[ 1 + \left( \frac{k_x}{k_y} \right)^2 \right] \cos(k_x x') \sin(k_y y). \quad (7)$$

Once the shock enters the space  $x' \geq 0$ , the velocity perturbations in front of it will induce postshock velocity fluctuations downstream, and its shape will be distorted, generating at the same time pressure and density perturbations in the compressed fluid. We assume that these fluctuations are always much smaller than the background values corresponding to a nondistorted shock. We introduce the following definitions, where the subscript 1 always refers to quantities in front of the shock front and the subscript 2 refers to the quantities behind it. We factor out the linear dependence with the dimensionless parameter  $u_1$ ,

$$\begin{aligned} \frac{\delta v_{1x}}{c_2} &= u_1 \cos(k_x x') \cos(k_y y), \\ \frac{\delta v_{1y}}{c_2} &= u_1 \frac{k_x}{k_y} \sin(k_x x') \sin(k_y y), \\ \frac{\delta \rho_2}{\rho_2} &= u_1 \tilde{\rho}(x', t) \cos k_y y, \\ \frac{\delta p_2}{\rho_2 c_2^2} &= u_1 \tilde{p}(x', t) \cos k_y y, \\ \frac{\delta v_{2x}}{c_2} &= u_1 \tilde{v}_x(x', t) \cos k_y y, \\ \frac{\delta v_{2y}}{c_2} &= u_1 \tilde{v}_y(x', t) \sin k_y y, \end{aligned} \quad (8)$$

and we defined  $\tilde{v}_{1x} = \cos(k_x x')$  and  $\tilde{v}_{1y} = (k_x/k_y) \sin(k_x x')$ . In Fig. 2(a) we show the perturbation field before the incident shock refraction at the weak contact discontinuity located at  $x' = 0$ . The position of the unperturbed shock in the laboratory frame is  $x'_s(t) = Dt$  for  $t < 0$ . We assume that the shock enters the half-space filled with the perturbed fluid, at  $t = 0$ . For simplicity in the calculations, the linearized equations of

motion are written in a frame of reference that moves with the compressed fluid, with coordinates  $x$  and  $y$  as shown in Fig. 2(b). Unless the contrary is explicitly said, the perturbed equations in the fluid downstream will be solved in the reference frame co-moving with the compressed fluid. After defining the dimensionless time  $\tau = k_y c_2 t$ , we write

$$\begin{aligned} \frac{\partial \tilde{\rho}}{\partial \tau} &= - \frac{\partial \tilde{v}_x}{\partial (k_y x)} - \tilde{v}_y, \\ \frac{\partial \tilde{v}_x}{\partial \tau} &= - \frac{\partial \tilde{p}}{\partial (k_y x)}, \\ \frac{\partial \tilde{v}_y}{\partial \tau} &= \tilde{p}, \end{aligned} \quad (9)$$

representing, respectively, the mass,  $x$ -momentum, and  $y$ -momentum conservation equations. Besides, we assume adiabatic flow in the fluid behind the shock, and therefore, the following relationship holds between the density and pressure perturbations,

$$\frac{\partial \tilde{\rho}}{\partial \tau} = \frac{\partial \tilde{p}}{\partial \tau}. \quad (10)$$

At  $t = 0+$  a shock is transmitted into the space to the right and a neutrally stable sound wave is reflected back into the space  $x < 0$ . The transmitted shock is deformed as it propagates into the disturbed fluid. As a consequence, pressure fluctuations will be generated behind its surface which propagate downstream in the form of sound waves. If the shock/turbulence interaction is started by a planar shock wave entering the weak perturbation field from a quiescent fluid, as shown in Fig. 2(a), then none of these waves gets reflected to the right, when they arrive at the interface  $x = 0$ . This constraint is known as the isolated shock boundary condition. (Examples of different boundary conditions, applicable when the incident shock is driven by a piston, are found in [23]). The sound perturbations radiated by the corrugated front go into the fluid downstream, eventually reaching the surface  $x = 0$ , and are transmitted into the space  $x < 0$  without being reflected toward the shock. Those perturbations will travel at the local sound velocity behind the neutral sound wave mentioned above. Pressure and normal velocity perturbations are continuous on both sides of it. However, the distorted front generates vorticity and entropy perturbations and the neutral sound wave to the left does not. Hence, the  $x$  derivative of  $v_y$  and the density perturbation are discontinuous at  $x = 0$ . The perturbed conservation equations across the neutral sound wave that travels to the left are the simplest to write,

$$\begin{aligned} \tilde{v}_x + \tilde{p} &= 0, \\ \tilde{v}_y &= 0, \end{aligned} \quad (11)$$

and both are valid just to the right of the left-facing sound wave, at the position  $x = -c_2 t$ , in the reference frame of the compressed fluid. There remain the boundary conditions at the corrugated shock front moving to the right. The unperturbed shock front position, as seen by an observer co-

moving with the fluid downstream, is given by:  $x_s(t)=(D-U)t$ . Its shape is deformed and is a function of  $y$  and  $t$ . We denote the shock ripple by  $\psi_s(t)\cos k_y y$ , and its dimensionless amplitude ( $\xi_s$ ) is defined by:  $k_y \psi_s(t)=u_1 \xi_s(t)$ . The boundary conditions at the corrugated shock front are obtained in the usual way, linearizing the Rankine-Hugoniot equations, supplemented with the conservation of tangential velocity across the shock ripple, as done in [7]. The perturbed quantities in Eqs. (12)–(15) below are evaluated at the shock front position. The linearized mass conservation is written as

$$(R-1)\frac{d\xi_s}{d\tau}=R\tilde{v}_x-\tilde{v}_{1xs}-M_2R\tilde{\rho}, \quad (12)$$

where  $\tilde{v}_{1xs}=\cos(k_x Dt)$ , and the  $x$ -momentum conservation is given by

$$\tilde{v}_x=\tilde{v}_{1xs}+\frac{1}{2M_2}\tilde{p}+\frac{M_2}{2}\tilde{\rho}. \quad (13)$$

The perturbation of the Rankine-Hugoniot curve gives us a relationship between  $\tilde{p}$  and  $\tilde{\rho}$ ,

$$\tilde{\rho}=\frac{1}{M_1^2 M_2^2}\tilde{p}. \quad (14)$$

Finally, the conservation of the tangential velocity across the shock front is written in the form

$$\tilde{v}_y=\tilde{v}_{1ys}+M_2(R-1)\xi_s, \quad (15)$$

where  $\tilde{v}_{1ys}=(k_x/k_y)\sin(k_x Dt)$ . It is understood that the downstream perturbation quantities  $\tilde{v}_x$ ,  $\tilde{\rho}$ , and  $\tilde{p}$  in Eqs. (12)–(15) above are given at the shock front position.

### B. Wave equation inside the compressed fluid

As can be seen from the last equations, the boundary conditions at the shock front are written at a moving surface. This fact certainly complicates the mathematical analysis in Cartesian coordinates  $(x, t)$ . Therefore, we change to a system of variables in which the shock front position does not depend on both independent variables. One of the possible options, as suggested for the first time in this type of problems in [5] and used later on in several works [6,9,23,51], is the transformation given by

$$\begin{aligned} k_y x &= r \sinh \chi, \\ \tau &= r \cosh \chi. \end{aligned} \quad (16)$$

It is easy to see that any surface  $\chi=const$  actually represents a planar front defined (in the compressed fluid frame of reference) by  $x=c_2 t \sinh \chi$ . This mathematical surface moves along the  $x$  axis with a velocity  $c_2 \tanh \chi$ , which for the shocked gas is lower than the speed of the shock front with respect to the compressed fluid,  $M_2 c_2$ . It is noted that the new shock front coordinate ( $\chi_s$ ) can be actually written in terms of the downstream shock Mach number as:  $\tanh \chi_s=M_2$ . Further, from Eq. (16), we see that

$$\tau=r_s \cosh \chi_s=\frac{r_s}{\sqrt{1-M_2^2}}. \quad (17)$$

We define the auxiliary function  $\tilde{h}$  by [51]

$$\tilde{h}=\frac{1}{r}\frac{\partial \tilde{p}}{\partial \chi}, \quad (18)$$

and the equations of motion [Eqs. (9) and (10)] can be rewritten in the new coordinates  $r, \chi$ . The mass conservation is recast as

$$-\sinh \chi \tilde{h}+\cosh \chi \frac{\partial \tilde{p}}{\partial r}+\frac{\cosh \chi}{r} \frac{\partial \tilde{v}_x}{\partial \chi}-\sinh \chi \frac{\partial \tilde{v}_x}{\partial r}+\tilde{v}_y=0, \quad (19)$$

while the  $x$ -momentum equation is given by

$$-\frac{\sinh \chi}{r} \frac{\partial \tilde{v}_x}{\partial \chi}+\cosh \chi \frac{\tilde{v}_x}{r}+\cosh \chi \tilde{h}-\sinh \chi \frac{\partial \tilde{p}}{\partial r}=0, \quad (20)$$

and the  $y$ -momentum equation is rewritten as

$$-\frac{\sinh \chi}{r} \frac{\partial \tilde{v}_y}{\partial \chi}+\cosh \chi \frac{\partial \tilde{v}_y}{\partial r}=\tilde{p}. \quad (21)$$

The shock/vorticity interaction problem here is analyzed within the limits of validity of a linear theory. Hence, up to a first-order expansion in the small parameter  $u_1$ , either  $\delta p$ ,  $\delta v_x$ , or  $\delta \rho$  downstream is proportional to  $\cos k_y y$ , which appears as a common factor in Eqs. (19) and (20) and can be therefore dropped out from both sides of those equations. Similarly, the terms that compose the tangential momentum conservation equation are proportional to  $\sin k_y y$ , which can also be canceled out. Therefore, we have omitted the  $y$  dependence in all the equations, for simplicity, thus only relating quantities that depend exclusively on  $r$  and  $\theta$  (or equivalently, on  $x$  and  $t$ ). The last equations can be combined into a system of coupled differential equations involving  $\tilde{p}$  and  $\tilde{h}$ ,

$$\begin{aligned} r \frac{\partial^2 \tilde{p}}{\partial r^2}+\frac{\partial \tilde{p}}{\partial r}+r \tilde{p} &= \frac{\partial \tilde{h}}{\partial \chi}, \\ r \tilde{h} &= \frac{\partial \tilde{p}}{\partial \chi}. \end{aligned} \quad (22)$$

It is clear that the system of equations above is equivalent to the wave equation downstream, which we also write here in Cartesian coordinates [51],

$$\frac{\partial^2 \tilde{p}}{\partial \tau^2}=\frac{\partial^2 \tilde{p}}{\partial (k_y x)^2}-\tilde{p}. \quad (23)$$

To get the solutions of this problem, we use the Laplace transform. The advantage is that we get exact analytic closed-form expressions for the Laplace transforms of the perturbation fields. After some algebra in the complex plane, we get the complete temporal evolution with an inverse transformation, and the exact asymptotic behavior by looking at the singularities of the Laplace functions [23,52].

### C. Shock pressure and shock corrugation as a function of time

#### 1. Solution of the wave equation

For any quantity  $\phi(\chi, r)$ , we define its Laplace transform (indicated with capital letters) by [53–56]

$$\Phi(\chi, s) = \int_0^\infty \phi(\chi, r) \exp(-sr) dr. \quad (24)$$

It is convenient to make the variable change  $s = \sinh q$  and transform Eqs. (22), following [6,9,51]

$$\frac{\partial}{\partial q} (\cosh q \tilde{P}) + \frac{\partial \tilde{H}}{\partial \chi} = 0, \quad (25)$$

$$\frac{\partial}{\partial \chi} (\cosh q \tilde{P}) + \frac{\partial \tilde{H}}{\partial q} = 0. \quad (26)$$

As discussed in [51], a first integral is obtained for the above system of equations, and written as

$$\cosh(q + \chi) \tilde{P}(\chi, q + \chi) + \tilde{H}(\chi, q + \chi) = 2F_1(q), \quad (27)$$

$$\cosh(q - \chi) \tilde{P}(\chi, q - \chi) - \tilde{H}(\chi, q - \chi) = 2F_2(q). \quad (28)$$

The functions  $F_1$  and  $F_2$  must be determined with the help of the boundary and initial conditions. As discussed in [10,23,52], it can be seen that  $F_1$  represents the sound perturbations radiated by the shock into the compressed fluid and  $F_2$  corresponds to the sound waves that arrive to the shock from behind. These waves might be evanescent or traveling fronts, depending on the ratio  $k_x/k_y$ , the shock Mach number, and the gas compressibility [23]. In this work, we consider an isolated shock, to which no sound waves arrive from the left. Therefore, the most general form for the function  $F_2$  is a constant, which is used to adjust the initial conditions behind the front at  $t=0+$  [23]. After some additional algebra, the following decomposition for the pressure and pressure gradient fluctuations is obtained:

$$\tilde{P}(\chi, q) = \frac{F_1(q - \chi) + F_2}{\cosh q}, \quad (29)$$

$$\tilde{H}(\chi, q) = F_1(q - \chi) - F_2. \quad (30)$$

The expressions shown in Eqs. (29) and (30) are valid in the whole compressed fluid in the space  $0 \leq x \leq x_s(t) = (D - U)t$ . To get the values of  $F_1$  and  $F_2$  (equivalently, the values of  $\tilde{P}$  and  $\tilde{H}$ ), we have to work out the boundary and initial conditions both at the shock front and at the surface  $x=0$ .

#### 2. Boundary and initial conditions

We transform the boundary conditions [Eqs. (12)–(15)] into a system of coupled partial differential equations for the shock pressure perturbation and the shock corrugation. From now on, the variables that are evaluated at the shock front coordinate are denoted with the subscript “s.” We follow Richtmyer [7] and take the time derivative of Eq. (13) along

the shock front trajectory. After using Eq. (9) together with the rest of the boundary conditions at the shock [Eqs. (12)–(15)], we arrive to the system

$$\begin{aligned} \tilde{h}_s(\tau) = & -\frac{M_1^2 + 1}{2M_1^2 M_2 \sqrt{1 - M_2^2}} \frac{dp_s}{d\tau} - \frac{2\sqrt{1 - M_2^2}}{\gamma + 1} \xi_s(\tau) \\ & + \frac{2\sqrt{1 - M_2^2} k_x}{(\gamma + 1) M_2 k_y} \sin\left(R \frac{k_x}{k_y} M_2 \tau\right), \end{aligned} \quad (31)$$

$$\frac{d\xi_s}{d\tau} = \frac{(\gamma + 1)}{4M_2} p_s(\tau) + \cos\left(R \frac{k_x}{k_y} M_2 \tau\right). \quad (32)$$

We use the coordinates defined in Eqs. (16), noting that  $\tau = r_s / \sqrt{1 - M_2^2}$  according to Eq. (17), and recast the system above into

$$\begin{aligned} \tilde{h}_s(r_s) = & -\frac{(M_1^2 + 1) d\tilde{p}_s}{2M_1^2 M_2 dr_s} - \frac{2\sqrt{1 - M_2^2}}{\gamma + 1} \xi_s(r_s) \\ & + \frac{(R - 1)\zeta_0}{R} \sin(\zeta_0 r_s), \end{aligned} \quad (33)$$

$$\frac{d\xi_s}{dr_s} = \frac{\gamma + 1}{4M_2 \sqrt{1 - M_2^2}} p_s(r_s) + \frac{\cos(\zeta_0 r_s)}{\sqrt{1 - M_2^2}}, \quad (34)$$

where  $\zeta_0$  is a dimensionless frequency that takes into account the periodicity of the preshock velocity field, and is given by

$$\zeta_0 = \frac{RM_2 k_x}{\sqrt{1 - M_2^2} k_y}. \quad (35)$$

We take the Laplace transform of Eqs. (33) and (34), use  $s = \sinh q$ , and arrive to the following system:

$$\begin{aligned} \tilde{H}_s(q) = & -\frac{M_1^2 + 1}{2M_1^2 M_2} [\sinh q \tilde{P}_s(q) - \tilde{p}_{s0}] - \frac{2\sqrt{1 - M_2^2}}{\gamma + 1} \bar{\xi}_s(q) \\ & + \frac{(R - 1)\zeta_0^2}{R(\sinh^2 q + \zeta_0^2)}, \end{aligned} \quad (36)$$

$$\sinh q \bar{\xi}_s(q) = \frac{\gamma + 1}{4M_2 \sqrt{1 - M_2^2}} \tilde{P}_s(q) + \frac{\sinh q}{\sqrt{1 - M_2^2} (\sinh^2 q + \zeta_0^2)}, \quad (37)$$

where  $\bar{\xi}_s = \int_0^\infty \xi_s(t) \exp(-st) dt$  is the Laplace transform of the dimensionless shock ripple corrugation. The quantity  $\tilde{p}_{s0}$  is the initial pressure perturbation at  $t=0+$  just behind the shock front. As commented in the previous subsection, when the planar shock arrives to the surface  $x=0$ , a transmitted shock starts moving to the right and a planar sonic wave is reflected to the left. Taking into account the continuity of pressure and normal velocity, as well as the discontinuity of density at both sides of  $x=0$ , the value of  $\tilde{p}_{s0}$  is found to be

$$\tilde{p}_{s0} = -\frac{2M_1^2 M_2}{2M_1^2 M_2 + M_1^2 + 1}. \quad (38)$$

From Eqs. (29) and (30) it is easy to see that

$$\tilde{H}_s(q) = \cosh q \tilde{P}_s(q) - 2F_2, \quad (39)$$

in which the quantity  $F_2$  has to be a constant in order to satisfy the isolated shock boundary condition [23]. Using Eqs. (36) and (37), it is not difficult to deduce that  $2F_2 = \tilde{p}_{s0}$ . The final exact expressions for the Laplace transforms  $\tilde{P}_s$  and  $\tilde{\xi}_s$  are obtained,

$$\begin{aligned} \tilde{P}_s(s) = & \frac{-2M_1^2 M_2 s}{2M_1^2 M_2 s \sqrt{s^2 + 1} + (M_1^2 + 1)s^2 + M_1^2} \\ & + \frac{2M_1^2 M_2 \alpha_v s}{[2M_1^2 M_2 s \sqrt{s^2 + 1} + (M_1^2 + 1)s^2 + M_1^2](s^2 + \zeta_0^2)}, \end{aligned} \quad (40)$$

$$\begin{aligned} \tilde{\xi}_s(s) = & -\frac{M_1^2(\gamma + 1)}{2\sqrt{1 - M_2^2}} \frac{1}{2M_1^2 M_2 s \sqrt{s^2 + 1} + (M_1^2 + 1)s^2 + M_1^2} \\ & + \frac{M_1^2(\gamma + 1)}{2\sqrt{1 - M_2^2}} \\ & \times \frac{\alpha_v}{[2M_1^2 M_2 s \sqrt{s^2 + 1} + (M_1^2 + 1)s^2 + M_1^2](s^2 + \zeta_0^2)} \\ & + \frac{1}{\sqrt{1 - M_2^2}} \frac{1}{s^2 + \zeta_0^2}. \end{aligned} \quad (41)$$

The coefficient  $\alpha_v$  is given by

$$\alpha_v = \frac{2}{\gamma + 1} \left( \frac{M_1^2 - 1}{M_1^2} \zeta_0^2 - 1 \right). \quad (42)$$

The Laplace function defined in Eq. (40) is formally equivalent to the one obtained for a preshock density nonuniformity [23]. The only formal differences between both cases (velocity and density preshock inhomogeneity) lies in the value of the coefficient  $\alpha_v$  and the initial shock pressure perturbation  $\tilde{p}_{s0}$ .

#### D. Inverse Laplace transforms of $\tilde{P}_s$ and $\tilde{\xi}_s$

To solve the pressure and velocity profiles in the compressed fluid (that is, the sound pressure waves, the vorticity generated at each position, the spatial structure of the longitudinal and transverse velocities, etc.), we must obtain the dynamical evolution of the shock pressure perturbation, as the shock moves to the right. This information may be obtained after inverting the expressions for  $\tilde{P}_s$  and  $\tilde{\xi}_s$  in the complex plane [10,23]. From the Laplace transform theory, we know that the function  $\tilde{p}_s(r_s)$  is formally calculated from the integral in the complex plane

$$\tilde{p}_s(r_s) = \frac{1}{2\pi i} \int_{c-i\infty}^{c+i\infty} \tilde{P}_s(s) \exp(sr_s) ds, \quad (43)$$

where  $c$  is a real number to the right of the singularities of  $\tilde{P}_s(s)$  and  $i$  is the imaginary unit ( $i^2 = -1$ ). To get an algebraic expression from Eqs. (40)–(43), we close the integration contour to the left and use the residue theorem [53–56], tak-

ing care of the singularities enclosed by the integration path. For a shock moving into an ideal gas, the only singularities of  $\tilde{P}_s(s)$ , as can be seen from Eq. (40), are the branch points at  $s = \pm i$ , and the poles at  $s = \pm i\zeta_0$ . The branch-point singularities represent the generation of evanescent sound wave perturbations, which decay asymptotically in time like  $t^{-3/2}$ , much in the same way as Bessel functions [55]. On the other hand, the imaginary poles give rise to asymptotic constant amplitude oscillations [23]. These permanent oscillations of the shock ripple are due to the perturbations in velocity distributed periodically upstream. Besides, the denominator  $2M_1^2 M_2 s \sqrt{s^2 + 1} + (M_1^2 + 1)s^2 + M_1^2$  never contributes with additional singularities that could result in permanent oscillations for an ideal-gas equation of state [52]. We obtain

$$\begin{aligned} \tilde{p}_s(r_s) = & -\frac{2}{\pi} \int_0^1 f_p(z) \cos(zr_s) dz + \frac{2\alpha_v}{\pi} \int_0^1 f_p(z) \\ & \times \left[ \frac{\cos(zr_s) - \cos(\zeta_0 r_s)}{\zeta_0^2 - z^2} \right] dz, \end{aligned} \quad (44)$$

where, the auxiliary function  $f_p$  is given by

$$f_p(z) = \frac{4M_1^4 M_2^2 z^2 \sqrt{1 - z^2}}{4M_1^2 M_2^2 z^2 (1 - z^2) + [(M_1^2 + 1)z^2 - M_1^2]^2}. \quad (45)$$

From the expressions above, we can also get the formulas for the asymptotic functions. We have to distinguish between the long- ( $\zeta_0 < 1$ ) and short- ( $\zeta_0 > 1$ ) wavelength regimes. From Eq. (40), the asymptotic behavior of  $\tilde{p}_s$  is found from the residues at the poles  $s = \pm i\zeta_0$  [23],

$$\tilde{p}_s(r_s) \cong \begin{cases} e_{lr} \cos(\zeta_0 r_s) + e_{li} \sin(\zeta_0 r_s), & \zeta_0 \leq 1 \\ e_s \cos(\zeta_0 r_s), & \zeta_0 \geq 1, \end{cases} \quad (46)$$

where  $r_s = \tau \sqrt{1 - M_2^2}$ , according to Eq. (17). The coefficients  $e_{lr}$ ,  $e_{li}$ , and  $e_s$  are formally equivalent to those obtained in [23],

$$\begin{aligned} e_{lr} = & \frac{2M_1^2 M_2 [M_1^2 - (M_1^2 + 1)\zeta_0^2] \alpha_v}{4M_1^4 M_2^2 \zeta_0^2 (1 - \zeta_0^2) + [M_1^2 - (M_1^2 + 1)\zeta_0^2]^2}, \\ e_{li} = & \frac{4M_1^4 M_2^2 \zeta_0 \sqrt{1 - \zeta_0^2} \alpha_v}{4M_1^4 M_2^2 \zeta_0^2 (1 - \zeta_0^2) + [M_1^2 - (M_1^2 + 1)\zeta_0^2]^2}, \\ e_s = & -\frac{2M_1^2 M_2 \alpha_v}{2M_1^2 M_2 \zeta_0 \sqrt{\zeta_0^2 - 1} + (M_1^2 + 1)\zeta_0^2 - M_1^2}. \end{aligned} \quad (47)$$

It is easy to see that the asymptotic expressions above are actually functions of the argument  $\zeta_0 r_s \equiv Dk_x t$  [23]. Besides, it is worth to note here that the only difference between the coefficients in the above equations and the corresponding ones in [23] is the dependence of  $\alpha_v$  on the shock strength, gas compressibility, and on the dimensionless frequency  $\zeta_0$ . We show the time evolution of the shock front pressure perturbations for different regimes, comparing the exact solution with the asymptotic expressions. The parameter that distinguishes both cases (long and short wavelength) is the dimensionless frequency  $\zeta_0$ . We show the shock front pressure fluctuations in Fig. 3 for a shock moving into an ideal gas

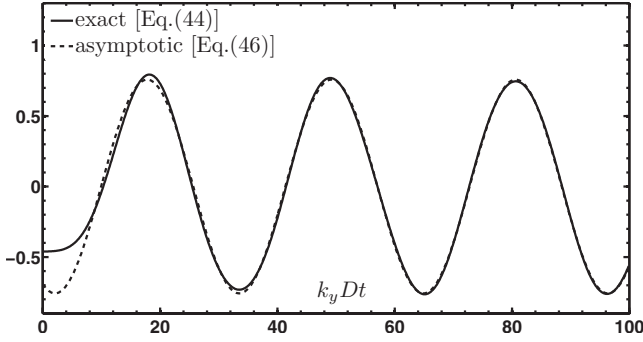


FIG. 3. Shock front pressure perturbations originating when a planar strong shock ( $M_1=3$ ) moves into an incompressible vorticity field in an ideal gas with  $\gamma=7/5$ . The ratio of longitudinal to transverse wave numbers is  $k_x/k_y=1/5$ , which gives  $\zeta_0=0.416\ 62$ .

with  $\gamma=7/5$ , the shock Mach number is  $M_1=3$ , and  $k_x/k_y=1/5$ , which gives  $\zeta_0=0.416\ 62$  (long wavelength). The solid curve is the exact solution given by Eq. (44), and the dotted curve is the asymptotic solution [Eq. (46)]. In Fig. 4 we show the shock pressure perturbations for the same gas and shock, but for a short-wavelength case ( $k_x/k_y=1$  and  $\zeta_0=2.083\ 10$ ), distinguishing between the exact and asymptotic functions of time. Similar calculations can be done to study the evolution of the shock ripple amplitude in both regimes. The details of the exact and asymptotic temporal evolution of the shock ripple amplitude together with the corresponding plots are shown in the Appendix A, which can be retrieved in the auxiliary file attached to this article [57].

#### E. Pressure perturbations radiated by the shock into the compressed fluid

As the shock ripple oscillates, pressure fluctuations are generated into the downstream fluid in the form of sound waves. In general, in the long-wavelength regime, those are evanescent waves that have an amplitude which decays in time like  $t^{-3/2}$  either at the shock front or at any other point in space in the compressed gas [5,6,10]. These are surface waves actually traveling along the  $\hat{y}$  axis and decaying spatially along the  $\hat{x}$  direction. As seen from an observer moving

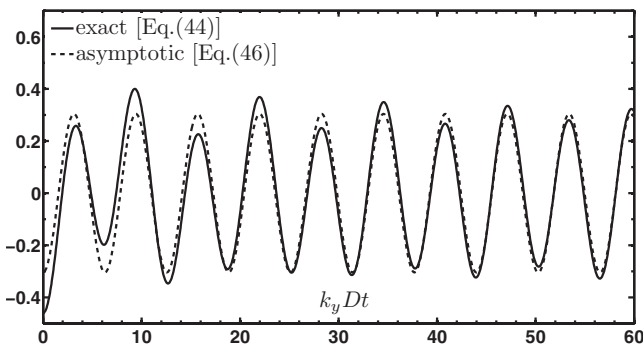


FIG. 4. Shock front pressure perturbations originating when a planar strong shock ( $M_1=3$ ) moves into an incompressible vorticity field in an ideal gas with  $\gamma=7/5$ . The ratio of longitudinal to transverse wave numbers is  $k_x/k_y=1$ , which gives  $\zeta_0=2.083\ 10$ .

with the shock, the pressure perturbations decay exponentially with the relative distance to the shock very near the front [23]. Nevertheless, as discussed in previous works too, there is the possibility for the oscillating shock to emit constant amplitude traveling sound waves into the compressed fluid. For this to happen, the frequency of oscillation at the shock front should be high enough, which in turn puts a lower limit to the spatial frequency of the vorticity modulation in the uncompressed gas [12,14–18,20,21,23]. We can easily find the mathematical structure of the sound waves, and understand the conditions under which those waves propagate, by studying the information provided by the Laplace transform  $\tilde{P}(\chi, q)$  in the space behind the shock. In fact, if we looked for the imaginary poles of the Laplace function, at any given value of the coordinate  $\chi$ , we would be able to write the analytical formula that represents the emitted sound perturbations, as well as to determine the necessary conditions for successful emission to occur. The procedure is equivalent to that used in [52], to study the spontaneous acoustic emission of a shock front moving into a fluid with a non-ideal-gas equation of state. With the help of Eqs. (27)–(29) and (40) we get  $F_1(q)$ . Then, we go back again to Eq. (29), valid for any value of  $\chi$ , in the interval  $0 \leq \chi \leq \chi_s = \tanh^{-1} M_2$ , to finally obtain  $\tilde{P}(\chi, q)$ . We have [23]

$$\tilde{P}(\chi, q) = \frac{\cosh(q + \chi_s - \chi)}{\cosh q} \tilde{P}_s(q + \chi_s - \chi), \quad (48)$$

where it is not difficult to realize [see Eq. (40)] that the right-hand side has a denominator of the form

$$\sinh^2(q + \chi_s - \chi) + \zeta_0^2 = [\sinh(q + \chi_s - \chi) + i\zeta_0] \times [\sinh(q + \chi_s - \chi) - i\zeta_0]. \quad (49)$$

After some elementary algebra, we can see that this term would contribute with imaginary poles at certain imaginary complex values for the Laplace variable  $s$  which we call  $s = \pm i\zeta_\chi$ , (hence contributing with constant amplitude oscillations) if and only if the following relationship holds:

$$\zeta_0 + \sqrt{\zeta_0^2 - 1} \geq \exp(\chi_s - \chi). \quad (50)$$

It is clear that the equation above implies that  $\zeta_0 > 1$ , which means that the running waves of constant amplitude can be emitted by the corrugated front only in the short-wavelength regime. Physically speaking, if  $\zeta_0 < 1$ , the longitudinal wave number associated to the sound wave would be a pure imaginary number, and the amplitude of the emitted perturbation would decay exponentially relative to the shock front position [23]. We define the auxiliary quantity  $\epsilon_0$  such that  $\zeta_0 = \cosh \epsilon_0$ . Then, the previous condition may be recast as

$$\zeta_0 \geq \cosh(\chi_s - \chi). \quad (51)$$

If Eq. (51) is fulfilled [or equivalently Eq. (50)], the mathematical surface defined by  $x/t = c_2 \tanh \chi$  would exhibit stable pressure oscillations. The frequency of those oscillations in the domain of the separable coordinates  $r, \chi$ , which

we name  $\zeta_\chi$ , is obtained by solving the equation:  $\sinh(q + \chi_s - \chi) = i\zeta_0$  (we remind that we here define  $\sinh q = \zeta_\chi$ ). We obtain

$$\begin{aligned}\zeta_\chi &= \cosh(\epsilon_0 - \chi_s + \chi) \\ &= \cosh(\epsilon_0 - \chi_s)\cosh \chi + \sinh(\epsilon_0 - \chi_s)\sinh \chi.\end{aligned}\quad (52)$$

Being constant amplitude oscillations defined on a moving surface, they actually represent traveling sound waves either to the right or to the left. Let us discern between these two possibilities, by explicitly working out their mathematical structure. In fact, when Eq. (50) [or Eq. (51)] is satisfied, the asymptotic pressure fluctuations are described in space and time by

$$\begin{aligned}\bar{p}(\chi, r) &= e_s \cos(\zeta_\chi r) \\ &= e_s \cos[\cosh(\epsilon_0 - \chi_s)\tau - \sinh(\chi_s - \epsilon_0)k_y x].\end{aligned}\quad (53)$$

Here,  $e_s$  is the asymptotic amplitude of the pressure perturbations at the shock front defined in Eq. (47). Looking inside the argument of the last equation, we realize that the function given in Eq. (53) represents propagating planar fronts in the  $(x, \tau)$  plane. If  $0 < \epsilon_0 < \chi_s$  (equivalently:  $1 < \zeta_0 < \cosh \chi_s = 1/\sqrt{1-M_2^2}$ ), the waves are emitted to the right, which then follow the shock front with a horizontal speed given by  $c_2 M_2 \tanh \chi < c_2 M_2$ . This last result is consistent with the fact that no sound waves impinge on the shock from behind. On the other hand, if  $\zeta_0 > \cosh \chi_s$  (equivalently:  $\epsilon_0 > \chi_s$ ), the sound waves are emitted to the left. In the absence of a reflecting surface at  $x=0$ , those waves escape toward  $x=-\infty$ . Furthermore, the frequency of oscillation of the compressed fluid particles downstream (when  $\zeta_0 > 1$ ) can be seen to be equal to

$$\zeta_1 = \cosh(\epsilon_0 - \chi_s) = \frac{\zeta_0 - M_2 \sqrt{\zeta_0^2 - 1}}{\sqrt{1 - M_2^2}},\quad (54)$$

and the longitudinal wave number of the sonic fronts ( $k_x^{ac}$ ) is equal to

$$\frac{k_x^{ac}}{k_y} = \sinh(\chi_s - \epsilon_0) = \frac{M_2 \zeta_0 - \sqrt{\zeta_0^2 - 1}}{\sqrt{1 - M_2^2}},\quad (55)$$

which is positive (and hence representing waves that travel to the right) if  $\epsilon_0 < \chi_s$ , and negative (representing waves to the left) if  $\epsilon_0 > \chi_s$ . We remind that the frequency of oscillation of the compressed fluid particles is  $\zeta_1 < \zeta_0$  due to the Doppler shift [37]. The boundary condition at  $x=0$  is that no sound waves arriving there get reflected. If the reflection was possible, because of the presence of a piston, for example, the reflected waves could have reached the shock from behind. For this to happen,  $\zeta_0$  should be greater than a certain value that would depend on the shock strength and the fluid compressibility. This possibility (as well as the possibility of having multiple reverberations between the shock and the reflecting surface) has been discussed in [23,52] and will be left for future study.

## F. Rotational and irrotational velocity perturbations in the compressed fluid

As the shock moves into the perturbed fluid upstream, additional velocity fluctuations are generated downstream. In this subsection we study the velocity field generated behind the shock front. At first, we discuss the velocity perturbations as a function of time at the surface  $x=0$ . In fact, the initial discontinuity in tangential velocity at that position will evolve like the contact surface of a RMI problem. In the next subsection, we analyze the vorticity deposition in the compressed gas and determine the rotational velocity profiles in both regimes of short and long wavelength. Finally, the velocity profiles associated to the sound waves emitted by the shock front are obtained.

### 1. RMI growth at $x=0$

To study the velocity perturbations that develop at the surface  $x=0$ , we consider the  $x$ -momentum equation in Eq. (20) and evaluate it at  $\chi=0$ . We take its Laplace transform, and with the help of Eqs. (27)–(29) and (40) we get the Laplace transform of the velocity fluctuations at the interface

$$\tilde{v}_x(x=0, s = \sinh q) = -\frac{\cosh(q + \chi_s)\tilde{P}_s(q + \chi_s)}{\sinh q}.\quad (56)$$

The exact temporal evolution since  $\tau=0+$  is formally given by

$$\bar{v}_{xi}(\tau) = \frac{1}{2\pi i} \int_{c-i\infty}^{c+i\infty} \tilde{v}_x(x=0, s)\exp(s\tau)ds,\quad (57)$$

where  $c$  is any real number to the right of all the singularities of the Laplace function  $\tilde{v}_x(x=0, s)$ . The procedure to calculate the integral in the complex plane above is the same as that used to calculate Eq. (43). We immediately recognize the existence of a pole at  $s = \sinh q = 0$ , and the possibility of having imaginary poles at  $s = \pm i\zeta_1$  if, and only if,  $\zeta_0 > 1/\sqrt{1-M_2^2}$  [see the discussion following Eq. (50)]. The physical origin of the pole at  $s=0$  is understood by realizing that there will be always RMI-like growth on that surface. In fact, once the transmitted shock starts to move to the right of it, the sound perturbations emitted by the corrugated front would progressively modify the instantaneous circulation, similarly as happens in a typical RMI problem, enhancing ripple growth. The difference here lies in the fact that the initial discontinuity at  $t=0+$  is on the longitudinal derivative of the transverse velocity, instead of being a discontinuity of the initial tangential velocity at both sides of  $x=0$ , as in the standard RMI problems [7,8,10,11,23,48–51]. In the long-wavelength regime, the pressure perturbations emitted by the shock fade away in time as  $t^{-3/2}$ , but they integrate to a final asymptotic rate of growth for the surface ripple, given by the pole at  $s=0$  of Eq. (56). In fact, we can get an explicit closed expression as a function of  $\gamma$  and  $M_1$ , after using Eq. (40),

$$\begin{aligned} \tilde{v}_{xi}^\infty &= -\frac{\tilde{P}_s(s = \sinh \chi_s)}{\sqrt{1 - M_2^2}} = \frac{(\gamma + 1)M_1^4}{[(2\gamma - 1)M_1^4 + 2M_1^2 + 1]} \frac{(k_x^2 + k_y^2)}{(R^2 k_x^2 + k_y^2)} \\ &= \frac{(\gamma + 1)M_1^4 [M_1^2 R + (M_1^2 - 1)\zeta_0^2]}{R[(2\gamma - 1)M_1^4 + 2M_1^2 + 1][M_1^2 + (M_1^2 - 1)R\zeta_0^2]}. \end{aligned} \quad (58)$$

It is stressed that in order to calculate the asymptotic rate of growth in Eq. (58), we need the exact complete expression for  $\tilde{P}_s$ . This means that the initial conditions are important to calculate the asymptotic normal velocity at  $x=0$ , similarly as occurs in any RMI problem [10,48–51]. In the short-wavelength regime, for those cases in which the dimensionless frequency  $\zeta_0$  satisfies  $\zeta_0 > 1/\sqrt{1 - M_2^2}$ , the sound waves traveling to the left would induce stable oscillations in time at any position  $x$  in the compressed fluid. In particular, the ripple at  $x=0$  will oscillate with frequency  $\zeta_1$ . Thus, in this regime, besides the pole at  $s=0$  in Eq. (56), giving rise to the asymptotic steady value of Eq. (58), we also have the contribution from the poles that would appear at  $s = \pm i\zeta_1$ . The amplitude of those oscillations can be calculated using the residue theorem on Eq. (56), or simply substituting Eq. (53) into the linearized  $x$ -momentum equation [see Eq. (9)], using Eq. (54). The asymptotic perturbed normal velocity at  $x=0$  for the short-wavelength situation is

$$\tilde{v}_{xi}(\tau \gg 1) \cong \tilde{v}_{xi}^\infty + Q_{ac} \cos(\zeta_1 \tau), \quad (59)$$

where

$$Q_{ac} = \frac{(M_2 \zeta_0 - \sqrt{\zeta_0^2 - 1})e_s}{\zeta_0 - M_2 \sqrt{\zeta_0^2 - 1}}, \quad (60)$$

in formal agreement with Eqs. (91) and (92) of [23]. We note the equivalence between  $Q_{ac}$  above, and the velocity amplitude  $v_{i1}$  in [23].

## 2. Downstream vorticity perturbations

Thanks to the conservation of tangential momentum across the shock front, it is not difficult to see that vorticity will be always generated behind a corrugated shock wave [23,48,50,51]. This vorticity will remain frozen to the fluid elements in the absence of viscosity, which we assume to be the case. The total vorticity in the compressed fluid will be composed of two terms, one due to an amplification of the upstream vorticity and the other one will be the result of the shock ripple oscillations. The first term, as will be seen in this subsection, is the result of the shock compression of the upstream vortices, in the direction of shock motion. The shock compression reduces the characteristic  $x$  length of the preshock eddies by a factor  $1/R = \rho_1/\rho_2$ . On the other hand, the second contribution comes from the shock oscillations, induced by the perturbations upstream. In fact, as the shock ripple oscillates, lateral pressure gradients are generated behind the shock, which induce an additional lateral velocity on the compressed fluid particles. Once the shock arrives at the point  $x$ , at the time  $t_0(x) = x/(D - U)$ , the vorticity that corresponds to the fluid element at that point will remain frozen to that fluid particle. We define the dimensionless vorticity for our 2D problem as

$$\tilde{\omega}(x, y) = \frac{\delta \omega_2}{k_y c_2} = g(k_y, x) \sin(k_y y), \quad (61)$$

where the function  $g$  is given by

$$g(k_y, x) = \left( \frac{\partial \tilde{v}_y}{\partial k_y x} \right)_{t=t_0(x)} + (\tilde{v}_x)_{t=t_0(x)}. \quad (62)$$

Both terms in the previous equation are evaluated just behind the shock front position, at the time  $t_0$  when the shock arrives to that position. The space derivative of the tangential velocity can be obtained by taking the time derivative of Eq. (15) following the shock trajectory [50,51]. We get

$$\begin{aligned} \left( \frac{\partial \tilde{v}_y}{\partial k_y x} \right)_{x=x_s} &= \left[ R \left( 1 + \frac{k_x^2}{k_y^2} \right) - 1 \right] \cos(Rk_x x) \\ &+ \left[ \frac{(M_1^2 - 1)R - 2M_1^2}{2M_1^2 M_2} \right] \tilde{p}_s[x, t_0(x)], \end{aligned} \quad (63)$$

where use has been made of the linearized Rankine-Hugoniot conditions [Eqs. (12)–(15)]. After some additional algebra, we obtain

$$g(k_y, x) = \Omega_1 \cos(Rk_x x) + \Omega_2 \tilde{p}_s \left( r_s = \frac{k_y x \sqrt{1 - M_2^2}}{M_2} \right), \quad (64)$$

where the quantities  $\Omega_{1,2}$  are given by

$$\begin{aligned} \Omega_1 &= R \left[ 1 + \left( \frac{k_x}{k_y} \right)^2 \right] = \frac{(\gamma + 1)M_1^2}{(\gamma - 1)M_1^2 + 2} + \frac{M_1^2 - 1}{M_1^2} \zeta_0^2, \\ \Omega_2 &= \frac{(M_1^2 - 1)^2 \sqrt{2\gamma M_1^2 - \gamma + 1}}{M_1^2 [(\gamma - 1)M_1^2 + 2]^{3/2}}. \end{aligned} \quad (65)$$

The calculation of the vorticity behind corrugated shock fronts had been studied in [24–26], and more recently reconsidered in [27,28]. In particular, the vorticity calculated in Eqs. (64) and (65) above coincides exactly with the prediction given by Eq. (2.18) of [28], with the baroclinic term equal to zero, as the upstream density is uniform in the problem treated here. Considering Eqs. (64) and (65), the term  $\Omega_1 \cos(Rk_x x)$  does explicitly depend on  $\zeta_0$ , as it quantifies the amplification of the preshock vorticity. The factor  $\Omega_2$  is the same quantity that appears in the calculation of the rate of growth of the RMI in [50,51], and also named  $\Omega$  in those references and represents the generation of vorticity due to shock curvature. In the long/short-wavelength regimes, both terms in Eq. (64) are oscillatory functions of  $x$ , very far from the weak/contact discontinuity at  $x=0$ . The characteristic length of the postshock eddies normal to the shock surface is  $\lambda_x/R$ . If there were a piston at  $x=0$ , reflecting the sound waves radiated by the corrugated shock, and if the conditions were adequate to make those reflected waves to impinge on the shock from behind, this effect would induce additional oscillations of the shock ripple with a lower frequency  $\zeta_2$  (because of the Doppler shift, it will be:  $\zeta_2 < \zeta_1 < \zeta_0$ , as discussed in [23,52]). These new oscillations would create an additional vorticity field with a larger characteristic longitudinal scale that would be superposed to that calculated using

Eq. (64). This possibility is left for future study. From the expression shown in Eq. (64), it is clear that the exact deposition of vorticity in the compressed fluid can be calculated using the formulas for  $\tilde{p}_s$  shown in Eqs. (44) and (45). We can also calculate the asymptotic behavior of the function  $g$ , using the asymptotic expressions given by Eq. (46) or alternatively, by looking at the poles of the Laplace transform of the function  $g(k_y x)$ . In fact, the transform of  $g$  is given by

$$G(\sigma) = \int_0^\infty g(k_y x) \exp(-\sigma k_y x) d(k_y x) \\ = \frac{\Omega_1 \zeta_0 \sinh^2 \chi_s}{\sigma^2 \sinh^2 \chi_s + \zeta_0^2} + \Omega_2 \tilde{P}_s(\sigma \sinh \chi_s). \quad (66)$$

The only poles of the right-hand side of Eq. (66) above are located at  $\sigma = \pm i R k_x / k_y$ . After substituting for  $\tilde{P}_s$  from Eq. (40) into Eq. (66), and using the residue theorem, we can also get the asymptotic dependence of the function  $g$  on the coordinate  $x$ . We use Eqs. (40), (66), and (46) to obtain

$$g(k_y x) \equiv \begin{cases} \sqrt{(\Omega_1 + \Omega_2 e_{lr})^2 + (\Omega_2 e_{li})^2} \cos(R k_x x - \phi_{rot}), & \zeta_0 \leq 1 \\ (\Omega_1 + \Omega_2 e_s) \cos(R k_x x), & \zeta_0 \geq 1, \end{cases} \quad (67)$$

where

$$\tan \phi_{rot} = \frac{\Omega_2 e_{li}}{\Omega_1 + \Omega_2 e_{lr}}. \quad (68)$$

The expressions for the coefficients  $e_{lr}$ ,  $e_{li}$ , and  $e_s$  have been given in Eq. (47). Once we have the exact and asymptotic expressions for the vorticity generated downstream, it is customary to calculate the associated velocity field.

### 3. Rotational velocity perturbations in the compressed fluid

When the shock front moves through the preshock vortices to the right of  $x=0$ , it generates tangential and normal velocity perturbations in order to satisfy the conservation equations across the front to match with the upstream fluctuations. This process creates a pressure gradient along the shock surface, distorting the shock shape. The shock pressure perturbations escape into the fluid downstream in the form of evanescent or traveling waves, depending on the specific value of the ratio  $k_x/k_y$ . Thus, we expect that when the shock is far enough from  $x>0$ , the asymptotic velocity at the position  $x$  will have two sources: on one hand, a rotational component attributed to the vorticity left in that fluid element by the corrugated shock, and on the other hand, the integration of all the impulses given to it, by the sound pressure waves. Therefore, the situation at any  $x>0$  is similar to the RMI growth that occurs at the ripple located at  $x=0$ . For the moment we only consider the long-wavelength situation. For simplicity, we name the rotational normal and tangential velocities by  $u$  and  $v$ , respectively. It is clear that the following identities hold, once the shock is far from the point with abscissa  $x$ , and the effect of the evanescent sound waves has vanished,

$$\tilde{v}_x[x, y, t \gg t_0(x)] = u(x) \cos(k_y y),$$

$$\tilde{v}_y[x, y, t \gg t_0(x)] = v(x) \sin(k_y y). \quad (69)$$

In the long-wavelength regime, the asymptotic velocity field is incompressible and the relationship  $v(x) = -u'(x)$  holds, where the prime indicates differentiation with respect to the argument. Using Eqs. (62) and (69), and the incompressibility condition, it is easy to get the ordinary differential equations satisfied by  $u$  and  $v$ ,

$$\frac{d^2 u}{d(k_y x)^2} - u = -g(k_y x), \quad (70)$$

$$\frac{d^2 v}{d(k_y x)^2} - v = g'(k_y x). \quad (71)$$

We concentrate in the solution of Eq. (70), as  $v$  is obtained from  $u$  by differentiation. The most general solution of Eq. (70) is written in the form

$$u(k_y x) = A \exp(-k_y x) + u_p(x), \quad (72)$$

where  $u_p$  is a particular solution and the constant  $A$  is chosen to match with the value of the asymptotic velocity at  $x=0$ , given in this case by Eq. (58). By direct substitution into Eq. (70), it is straightforward to see that a particular solution can be written as

$$u_p(k_y x) = \frac{\Omega_1 \sinh^2 \chi_s}{\sinh^2 \chi_s + \zeta_0^2} \cos\left(\frac{\zeta_0 k_y x}{\sinh \chi_s}\right) \\ + \frac{2\Omega_2 \alpha_v}{\pi} \int_0^1 \frac{f_p(z) j_u(z, x)}{(z^2 - \zeta_0^2)} dz \\ - \frac{2\Omega_2 \sinh^2 \chi_s}{\pi} \int_0^1 \left[ \frac{f_p(z)}{z^2 + \sinh^2 \chi_s} \cos\left(\frac{z k_y x}{\sinh \chi_s}\right) \right] dz, \quad (73)$$

where the auxiliary function  $j_u$  is

$$j_u(z, x) = \frac{\sinh^2 \chi_s}{\zeta_0^2 + \sinh^2 \chi_s} \cos\left(\frac{\zeta_0 k_y x}{\sinh \chi_s}\right) \\ - \frac{\sinh^2 \chi_s}{z^2 + \sinh^2 \chi_s} \cos\left(\frac{z k_y x}{\sinh \chi_s}\right), \quad (74)$$

and we remind that the argument  $\zeta_0 k_y x / \sinh \chi_s$  is equal to  $R k_x x$ . Besides, using Eq. (58) and (77) below, it can be seen that:  $u_p(0) = 2\tilde{v}_{xi}^\infty$ . From the arguments given above, it is clear that in order to match the velocity perturbation at  $x=0$ , we have the following expression for the asymptotic longitudinal velocity in the compressed fluid:

$$u(k_y x) = u_p(k_y x) - \tilde{v}_{xi}^\infty \exp(-k_y x). \quad (75)$$

Equation (75) is the exact result for the normal velocity in the fluid downstream, once the shock is very far from the point  $x$ , for long-wavelength perturbations. In agreement with Fraley [10], the velocity is seen to decay exponentially very near the surface  $x=0$ , but is dominated by the vorticity ahead of it, which in this case induces an oscillatory behavior

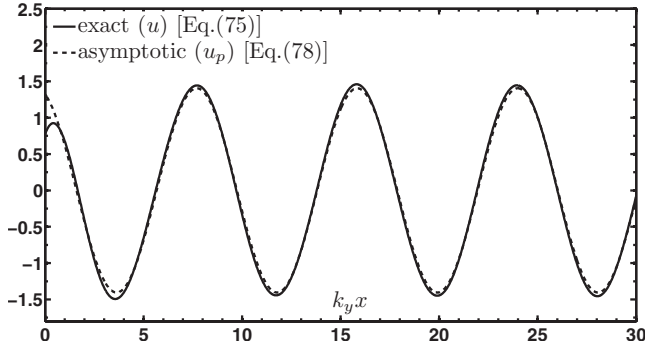


FIG. 5. Exact and asymptotic normal velocity perturbation as a function of the coordinate  $x$ , for a planar strong shock ( $M_1=3$ ) that moves into an incompressible vorticity field in an ideal gas with  $\gamma=7/5$ . The ratio of longitudinal to transverse wave numbers is  $k_x/k_y=1/5$  which gives  $\zeta_0=0.41662$ .

as a function of  $x$  with a spatial frequency equal to  $Rk_x$ . That is, very far from  $x=0$ , the asymptotic behavior is dominated by the particular solution  $u_p$ , as the effect of the exponential term can be safely neglected. To get the asymptotic form of  $u_p(k_y x)$ , it is instructive to work with its Laplace transform. If we go back to Eq. (70), multiply both sides by  $\exp(-\sigma k_y x)$  and integrate between  $x=0$  and  $x=\infty$ , we get

$$U_p(\sigma) = \frac{u_p(0) - G(\sigma)}{\sigma^2 - 1}, \quad (76)$$

where we have used the result:  $u_p'(0)=0$  [see Eq. (73)]. The value of  $G$  is taken from Eq. (66). It is easy to see that the right-hand side of the above equation must be defined for  $\sigma=1$ , as it cannot be a pole. Then, we get the relationship

$$u_p(0) = G(1) = \frac{\Omega_1 \zeta_0}{1 + \left(R \frac{k_x}{k_y}\right)^2} + \Omega_2 \tilde{P}_s(\sinh \chi_s). \quad (77)$$

From Eqs. (66) and (76) we realize that there are two imaginary poles for  $U_p$  located at  $\sigma = \pm iRk_x/k_y$ . After some algebra we find the asymptotic expressions in the long-wavelength regime,

$$\begin{aligned} u_p(x \gg \lambda_y) &\cong Q_{rot}^l \cos(Rk_x x - \phi_{rot}), \\ v_p(x \gg \lambda_y) &\cong Q_{rot}^l R \frac{k_x}{k_y} \sin(Rk_x x - \phi_{rot}), \end{aligned} \quad (78)$$

where

$$Q_{rot}^l = \frac{\sqrt{(\Omega_1 + \Omega_2 e_{lr})^2 + (\Omega_2 e_{li})^2}}{1 + \left(R \frac{k_x}{k_y}\right)^2}, \quad (79)$$

and  $\phi_{rot}$  has been defined in Eq. (68). The coefficients  $e_{lr}$  and  $e_{ls}$  can be found in Eq. (47). In Fig. 5 we show the normal velocity  $u(x)$ , calculated exactly, using Eq. (75), and compare it with the asymptotic expression given by Eq. (78) for the long-wavelength case, with the same parameters as in Fig. 3. Near the weak discontinuity at  $x=0$  the velocity perturbation is dominated by the complete expression of  $u$  given in Eq. (75), in which the exponential term cannot be ne-

glected [10]. This is a characteristic common to RMI problems: the asymptotic growth very near the contact surface at  $x=0$  is dependent on the whole history of the pressure perturbations evolving between the shock front(s) and the contact surface ripple [10,48,49,51]. That is, initial conditions are necessary to calculate asymptotic velocity perturbations at  $x=0$ . For  $x \gg \lambda_y$ , on the other hand, the velocity perturbations show a periodic asymptotic, only driven by the combined effects of the amplified upstream vorticity and the vorticity-generated downstream because of shock curvature. In this case, the shock has already entered its asymptotic regime and hence, initial conditions are not necessary to determine the velocity perturbations far from  $x=0$ .

In the short-wavelength regime, the rotational asymptotic velocity field is described by

$$\begin{aligned} u_p(x \gg \lambda_y) &\cong Q_{rot}^s \cos(Rk_x x), \\ v_p(x \gg \lambda_y) &\cong Q_{rot}^s R \frac{k_x}{k_y} \sin(Rk_x x), \end{aligned} \quad (80)$$

where  $Q_{rot}^s$  in the short-wavelength regime is given by

$$Q_{rot}^s = \frac{\Omega_1 + \Omega_2 e_s}{1 + \left(R \frac{k_x}{k_y}\right)^2}. \quad (81)$$

The value of  $e_s$  can be found in Eq. (47).

#### 4. Irrotational velocity profiles in the short-wavelength regime

For short enough wavelengths (that is, when  $\zeta_0 \geq 1$ ), the shock front successfully radiates traveling sonic perturbations. We know that depending on the value of  $\zeta_0$  as compared to that of  $1/\sqrt{1-M_2^2}$ , the pressure waves travel to the right, following the shock with a lower  $x$  velocity, or travel to the left, escaping from the shock to  $x=-\infty$ . As the sound wave fluctuations will contribute with velocity fluctuations, they do contribute to the downstream kinetic energy. It will later be seen that, actually, the contribution of the sonic velocity field is negligible compared to the rotational contribution calculated in the last subsection. Nevertheless, the sound wave field dominates the kinetic-energy budget for very weak shocks ( $M_1 - 1 \ll 1$ ). Thus, it is necessary to unveil the details of the sonic perturbation field. To this scope, we write the equations of motion [Eqs. (9) and (10)] in a more compact form. We define the dimensionless differential operator,

$$\vec{\nabla}_{2D} = \hat{x} \frac{\partial}{\partial(k_y x)} + \hat{y} \frac{\partial}{\partial(k_y y)}, \quad (82)$$

and Eqs. (9) and (10) can be rewritten in the form [56]

$$\frac{\partial^2 \vec{v}}{\partial \tau^2} = \vec{\nabla}_{2D} \times [g(x) \sinh(k_y y) \hat{z}] + \nabla_{2D}^2 \vec{v}, \quad (83)$$

where the product symbol  $\times$  indicates vector product and the operator  $\nabla_{2D}^2$  is defined by

$$\nabla_{2D}^2 = \frac{\partial^2}{\partial(k_y x)^2} + \frac{\partial^2}{\partial(k_y y)^2}. \quad (84)$$

Evaluating the  $x$  component of Eq. (83), we get

$$\frac{\partial^2 \tilde{v}_x}{\partial \tau^2} = \nabla_{2D}^2 \tilde{v}_x + g(x) \cos(k_y y). \quad (85)$$

The solution to this last equation can always be put in the form

$$\tilde{v}_x(x, y, t) \equiv \tilde{v}_x^{ac}(\tau, x) \cos(k_y y) + u(k_y x) \cos(k_y y), \quad (86)$$

where the function  $\tilde{v}_x^{ac}$  satisfies the homogeneous wave equation in 2D,

$$\frac{\partial^2 \tilde{v}_x^{ac}}{\partial \tau^2} = \frac{\partial^2 \tilde{v}_x^{ac}}{\partial (k_y x)^2} - \tilde{v}_x^{ac}. \quad (87)$$

The function  $u(k_y x)$  satisfies Eq. (70) and is also formally given by Eq. (75) in the short-wavelength regime. Summing up, Eq. (86) expresses the fact that the velocity field is decomposed in two parts: a steady rotational contribution, which is also divergence free and has been calculated in the last subsection, plus a second term which does not add vorticity but travels in the compressed fluid with the local sound speed. When  $\zeta_0 < 1$ , this potential contribution is actually an evanescent sound wave that vanishes asymptotically in time like  $t^{-3/2}$  at any position  $x$ , and it is only the rotational part  $u(k_y x) \cos(k_y y)$  that remains as a permanent velocity perturbation when the shock is far away. On the other hand, when  $\zeta_0 > 1$ , the solutions to Eq. (87) add a nonzero contribution to  $v_x$  consisting of constant amplitude oscillations, for  $t \gg t_0(x)$ . These oscillations travel as planar fronts with a definite orientation in space, which is a function of  $\zeta_0$ . In fact, in accordance to the previous discussion, the function  $\tilde{v}_x^{ac}$  can be written, asymptotically in time, as

$$\tilde{v}_x^{ac}(x, t \gg t_0) \equiv Q_{ac} \cos(\pm k_y x \sqrt{\zeta_1^2 - 1} + \zeta_1 \tau), \quad (88)$$

where  $Q_{ac}$  has been defined in Eq. (60). Equation (88) can be verified substituting it into Eq. (87). Further, we recognize the wave vector of the traveling sound wave, defined by

$$\tilde{k}_{ac} = (k_x^{ac}, k_y), \quad (89)$$

where  $|k_x^{ac}| = k_y \sqrt{\zeta_1^2 - 1}$ . The sonic front described by Eq. (88) actually represents the superposition of two planar waves running in opposite directions along the  $y$  axis, each of which has a ray inclined with respect to the  $x$  direction through an angle  $\pm \theta_{ac}$ . According to Eq. (55), the value of  $\theta_{ac}$  is given by

$$\tan \theta_{ac} = \frac{k_y}{k_x^{ac}} = \frac{\sqrt{1 - M_2^2}}{M_2 \zeta_0 - \sqrt{\zeta_0^2 - 1}}. \quad (90)$$

To conclude this subsection, we write both components of the total velocity field when  $\zeta_0 \geq 1$ , for  $x \gg \lambda_y$  and  $t \gg t_0(x)$ ,

$$\tilde{v}_x(x, y, t) \equiv [Q_{rot}^s \cos(Rk_x x) + Q_{ac} \cos(k_x^{ac} x - \zeta_1 \tau)] \cos(k_y y),$$

$$\begin{aligned} \tilde{v}_y(x, y, t) \equiv & \left[ Q_{rot}^s \frac{Rk_x}{k_y} \sin(Rk_x x) - \frac{Q_{ac} \sqrt{1 - M_2^2}}{\sqrt{\zeta_0^2 - 1} - M_2 \zeta_0} \right. \\ & \left. \times \sin(k_x^{ac} x - \zeta_1 \tau) \right] \sin(k_y y), \end{aligned} \quad (91)$$

where  $Q_{ac}$  is given by Eq. (60) and  $Q_{rot}^s$  is given by Eq. (81).

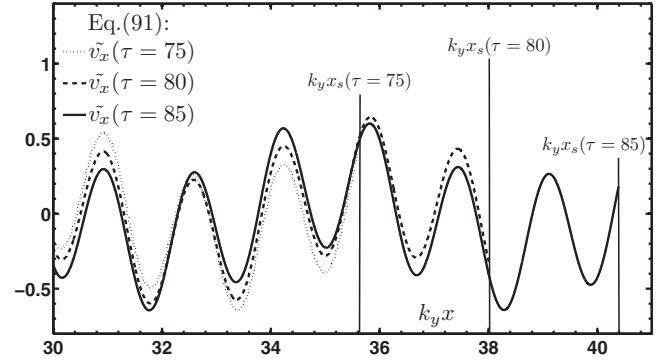


FIG. 6. Asymptotic normal velocity perturbation as a function of the coordinate  $x$ , at different times, for a planar strong shock ( $M_1=3$ ) that moves into an incompressible vorticity field in an ideal gas with  $\gamma=7/5$ . The ratio of longitudinal to transverse wave numbers is  $k_x/k_y=1$  which gives  $\zeta_0=2.083$ . For this case, the sound waves fill the whole compressed gas, which induce oscillations around steady-state value (80) with a beat determined by  $\zeta_1$ .

When  $1 \leq \zeta_0 < 1/\sqrt{1-M_2^2}$ ,  $k_x^{ac} > 0$  and the waves travel to the right. For  $\zeta_0 \geq 1/\sqrt{1-M_2^2}$ ,  $k_x^{ac} < 0$  and they move to the left. If  $\zeta_0 = 1/\sqrt{1-M_2^2}$ , the waves that escape from the shock actually travel along the  $y$  direction in the frame co-moving with the compressed fluid.

To illustrate Eq. (91), we show the normal velocity ( $\tilde{v}_x$ ) for a short-wavelength case in Fig. 6 for a case in which the sound waves emitted by the front fill the whole space downstream. The velocity curves are shown quite far from the weak discontinuity at  $x=0$ , and enough time has passed such that the shock entered its own asymptotic regime, oscillating with the dimensionless frequency  $\zeta_0 \sqrt{1-M_2^2}$ . We show the normal velocity profiles given by  $\tilde{v}_x$  in Eq. (91), at different values of the dimensionless time  $\tau$ . The solid vertical lines indicate the instantaneous shock front positions at the corresponding values of  $\tau$ . We can see that the velocity field is a superposition of an average steady profile [corresponding to  $u_p$  in Eq. (80)] plus an oscillation driven by the sound waves in Eq. (88).

### III. SHOCK COMPRESSION OF TURBULENT 2D/3D RANDOM VORTICITY FIELDS

In this section we study the interaction of a planar shock with a fully turbulent rotational 3D velocity field upstream. At first, we describe analytically the most general of such velocity fields in front of the shock, in terms of the Euler angles. This description is helpful to represent any arbitrary incompressible velocity perturbation field with prescribed vorticity, with any degree of anisotropy in terms of three orientation angles. The discussion will be later greatly simplified to deal only with isotropic distributions of velocity and vorticity. Nevertheless, the way is prepared in order that it is possible to analyze the interaction of a planar shock wave with arbitrary anisotropic velocity fields in future works.

#### A. General 3D upstream/downstream perturbation flows: geometrical representation

Let us consider a rotational and incompressible 3D velocity field in the space  $X \geq 0$ , with arbitrarily oriented coordi-

nates axes  $\{X, Y, Z\}$ , and the planar shock moving along the  $\hat{X}$  direction. Without loss of generality, the upstream velocity field may be assumed to consist of shear waves with a wave number given by the vector  $\vec{k} = (k_X, k_Y, k_Z)$ . Because of incompressibility, each  $\vec{k}$  defines a planar wave, perpendicular to it, on which the velocity perturbations are prescribed. These velocity disturbances may be assumed to be of the form

$$\vec{v}_1(X, Y, Z) = \delta\vec{v}_1 \exp[i(k_X X + k_Y Y + k_Z Z)]. \quad (92)$$

The components of the velocity vector  $\delta\vec{v}_1 = (\delta v_{1X}, \delta v_{1Y}, \delta v_{1Z})$  are not arbitrary. In fact, from the incompressibility of the upstream perturbations, we have:  $\vec{\nabla} \cdot \vec{v}_1 = 0$ , which may be recast as:  $\vec{k} \cdot \delta\vec{v}_1 = 0$ , after using Eq. (92). We also compute the vorticity of the upstream field,

$$\delta\vec{\omega}_1 = \vec{k} \times \delta\vec{v}_1 \exp[i(k_X X + k_Y Y + k_Z Z)], \quad (93)$$

where use has been made of the definition of vorticity ( $\vec{\omega}_1 = \vec{\nabla} \times \vec{v}_1$ ) and Eq. (92). We denote the unit vectors in the directions of the wave number, the upstream velocity, and the upstream vorticity by:  $\hat{k}$ ,  $\hat{v}_1$ , and  $\hat{\omega}_1$ , respectively. It is clear that the set of vectors  $\{\hat{k}, \hat{v}_1, \hat{\omega}_1\}$  constitutes a set of rigid axes with the same geometrical properties as the right-handed system of Cartesian coordinates  $\{X, Y, Z\}$ . Thus, we can specify the orientation of one of them with respect to the other set of unit vectors, in terms, for example, of the Euler angles [58,59]. In this way, the task of representing an arbitrary velocity/vorticity field in front of the shock can be accomplished by means of three rotation angles:  $\varphi$ ,  $\theta$ , and  $\psi$ . To write the components of the velocity and the wave-number vector as a function of these rotation angles, the best option is to start with the simplest configuration for the unit vectors  $\{\hat{k}, \hat{v}_1, \hat{\omega}_1\}$ . We can initially choose  $\hat{k} = \hat{X}$ ,  $\hat{v}_1 = \hat{Y}$ , and  $\hat{\omega}_1 = \hat{Z}$ , shown in Fig. 7(a). The first transformation is a counterclockwise rotation of angle  $\varphi$  on the shock plane around the vector  $\hat{k} \equiv \hat{X}$ . In this way, we rotate the velocity and vorticity vectors on the shock plane around the wave-number vector. The transformed vectors are  $\hat{v}'_1$  and  $\hat{\omega}'_1$ . Next, we perform a rotation of angle  $\theta$ , around the vector  $\hat{v}'_1$  (in this second transformation the vector  $\hat{v}'_1$  is unchanged), which takes the vorticity away from the surface of the shock, making it to point into the uncompressed fluid, as shown in Fig. 7(b). The new rotated vectors after this second motion are  $\hat{k}''$  and  $\hat{\omega}''_1$ . The last axes transformation is a rotation of angle  $\psi$  around the vector  $\hat{k}''$ , which makes the final vector  $\hat{v}'''_1$  to point into the fluid ahead of the shock surface, as well as the new vectors  $\hat{k}''' = \hat{k}$  and  $\hat{\omega}'''_1$ , indicated in Fig. 7(c). The composition of these three motions gives us the most general set of vectors  $\{\hat{k}, \hat{v}_1, \hat{\omega}_1\}$ , which are arbitrarily oblique to the shock surface and simultaneously satisfy the incompressibility condition. It is not difficult to write the components of the rotated vectors, in terms of the rotation angles [58,59],

$$k_X = k \cos \theta,$$

$$k_Y = -k \sin \psi \sin \theta,$$

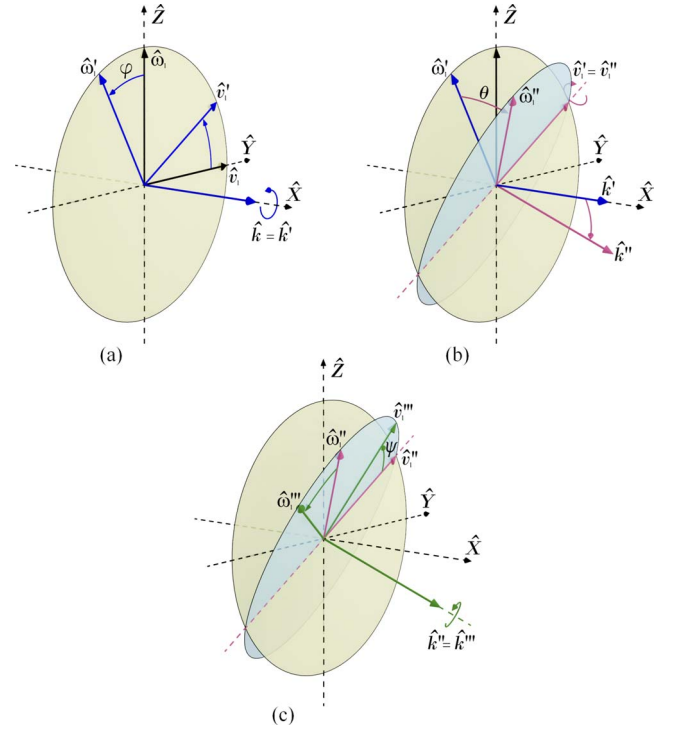


FIG. 7. (Color online) Sequence of space rotations characterized by the Euler angles describing the most general rotational velocity field in front of the incident shock.

$$k_Z = -k \cos \psi \sin \theta, \quad (94)$$

where we have defined:  $k = |\vec{k}|$ . In Fig. 7 we show the rotations that define the components of the upstream velocity and vorticity fields in terms of the Euler angles as presented in Eqs. (94)–(96). The components of the velocity vector are (we omit the exponential factor  $\exp[i(k_X X + k_Y Y + k_Z Z)]$  in each component, for simplicity in the notation)

$$\delta v_{1X} = -\delta v_1 \sin \varphi \sin \theta,$$

$$\delta v_{1Y} = \delta v_1 (\cos \psi \cos \varphi - \sin \psi \sin \varphi \cos \theta),$$

$$\delta v_{1Z} = \delta v_1 (-\sin \psi \cos \varphi - \cos \psi \sin \varphi \cos \theta), \quad (95)$$

where  $\delta v_1 = |\delta\vec{v}_1|$ . The upstream vorticity components are given by

$$\delta \omega_{1X} = k \delta v_1 \cos \varphi \sin \theta,$$

$$\delta \omega_{1Y} = k \delta v_1 (\cos \psi \sin \varphi - \sin \psi \cos \varphi \cos \theta),$$

$$\delta \omega_{1Z} = k \delta v_1 (-\sin \psi \sin \varphi + \cos \psi \cos \varphi \cos \theta), \quad (96)$$

where the complex exponential factors have also been omitted in the vorticity components for simplicity in the notation. The angle  $\varphi$  describes rigid rotations in the plane of the shock front and its range of variation is  $0 \leq \varphi < 2\pi$ . The angle  $\theta$  is equivalent to the azimuthal angle in spherical coordinates, with the  $x$  axis taken as the polar axis, and the range of variation is  $0 \leq \theta \leq \pi$ . Finally, the angle  $\psi$  describes rotations in a plane perpendicular to the wave-number vector

$\vec{k}$ , and it takes values inside the interval:  $0 \leq \psi < 2\pi$ . Each choice of the set  $\{\varphi, \theta, \psi\}$  represents a different planar shear wave in front of the shock. The advantage of disposing of the analytical form given by Eqs. (94)–(96) is the fact that they could be eventually used to account for non axisymmetric or nonisotropic conditions upstream. However, if we consider an isotropic distribution of velocities in front of the shock, we may assume isotropy of rotations in the plane of the shock and in the plane perpendicular to the wave-number vector  $\vec{k}$ . Then, for given values of  $\delta v_1$  and  $k$ , the probability that the set of vectors  $\vec{k}$ ,  $\delta \vec{v}_1$ , and  $\delta \vec{\omega}_1$  will be oriented according to Eqs. (94)–(96) is taken proportional to the solid angle, which in terms of the angle differentials is equal to

$$\frac{1}{8\pi^2} \sin \theta d\theta d\varphi d\psi. \quad (97)$$

Thus, we can easily compute the mean values of the squares of the components of the velocity and the vorticity vectors. For the velocity upstream, we get the averages,

$$\langle \delta v_{1X}^2 \rangle = \langle \delta v_{1Y}^2 \rangle = \langle \delta v_{1Z}^2 \rangle = \frac{\delta v_1^2}{3}, \quad (98)$$

and for the vorticity components we obtain

$$\langle \delta \omega_{1X}^2 \rangle = \langle \delta \omega_{1Y}^2 \rangle = \langle \delta \omega_{1Z}^2 \rangle = \frac{(k \delta v_1)^2}{3}, \quad (99)$$

where isotropy is evident, either for the velocity or the vorticity fields. With Eqs. (94)–(96) at our disposal, the formal procedure to study the interaction of a planar shock wave with a 3D field of shear waves consists of solving the wave equation in the compressed fluid domain and impose the corresponding boundary conditions at the shock front and far downstream. It is further not difficult to realize that when passing from 2D to 3D,  $k_Y$  must be replaced by  $k_\perp = \sqrt{k_Y^2 + k_Z^2} = k \sin \theta$ . Linearized Rankine-Hugoniot conditions (31)–(34) remain formally the same, except for the new value of  $\zeta_0$ , in which  $k_\perp$  is used,

$$\zeta_0 = \frac{RM_2}{\sqrt{1 - M_2^2}} \frac{k_X}{k_\perp}. \quad (100)$$

Furthermore, due to linearity, the interaction of the shock front with the velocity field represented by Eqs. (94)–(96) may be seen as a linear transformation that takes the input vector  $\delta \vec{v}_1 \exp[i(k_X X + k_Y Y + k_Z Z)]$  upstream, into the velocity vector downstream,

$$\delta \vec{v}_2 = \delta \vec{v}_2^{rot} \exp[i(Rk_X X + k_Y Y + k_Z Z)] + \delta \vec{v}_2^{ac}(X, Y, Z, t), \quad (101)$$

where we emphasized that the velocity perturbations behind the shock are written as the sum of incompressible rotational perturbations frozen to the fluid particles (which account for the vorticity) plus an irrotational part that travels in space with the local sound speed (which corresponds to the sound waves emitted downstream). The superscript “rot” in Eq. (101) refers to the amplitude of the downstream vorticity shear waves. The longitudinal wave number of the rotational perturbations is amplified by a factor  $R$ . From now on, we

will concentrate in the asymptotic velocity fields behind the shock, assuming that the transient for each mode has passed. Therefore, the potential part of the decomposition above can be written, asymptotically in time, as

$$\delta \vec{v}_2^{ac}(X, Y, Z, t \gg t_0) \cong \delta \vec{v}_2^{ac} \exp[i(\pm k_\perp X \sqrt{\zeta_0^2 - 1} + \zeta_1 k_\perp c_2 t + k_Y Y + k_Z Z)], \quad (102)$$

where the possibility of having right facing waves or left-facing waves only depends on whether  $\zeta_0$  is smaller or greater than  $1/\sqrt{1 - M_2^2}$ , as discussed in the last section. The superscript “ac” in Eq. (102) refers to the amplitude of the downstream acoustic velocity waves. Due to linearity, it is clear that the values of the downstream velocity amplitudes  $\delta \vec{v}_2^{rot}$  and  $\delta \vec{v}_2^{ac}$  can be obtained from the amplitude of the upstream velocity vector  $\delta \vec{v}_1$ , through appropriate linear transformations,

$$\begin{aligned} \delta \vec{v}_2^{rot} &= \bar{M}_{rot}(\vec{k}, \zeta_0, M_1) \delta \vec{v}_1, \\ \delta \vec{v}_2^{ac} &= \bar{M}_{ac}(\vec{k}, \zeta_0, M_1) \delta \vec{v}_1, \end{aligned} \quad (103)$$

where  $\bar{M}_{rot}$  and  $\bar{M}_{ac}$  are square matrices of dimension three, whose components may be derived after some tedious algebra, by generalizing the calculations of the last Section. However, taking profit of the symmetry of rotations in the plane of the shock, for an isotropic field upstream, we can substantially simplify the algebra, reducing the 3D situation to an equivalent 2D problem. This task, and the calculation of the averages of the different quantities in the fluid downstream is presented in the following subsections.

## B. Reduction to an equivalent 2D problem

The former representation of the velocity field can be drastically simplified so as to deal with an equivalent 2D description. In fact, we can always rotate counterclockwise the set of axes  $\{X, Y, Z\}$  around the normal to the shock, by an angle  $\pi/2 - \psi$  to get a new set of axes, which we name  $\{x, y, z\}$ . The new components of the wave-number vector in front of the shock are

$$\begin{aligned} k_x &= k \cos \theta, \\ k_y &= -k \sin \theta, \\ k_z &= 0, \end{aligned} \quad (104)$$

where we see that the  $z$  component of the wave-number vector is zero. The new components of the upstream velocity field are

$$\begin{aligned} \delta v_{1x} &= -\delta v_1 \sin \theta \sin \varphi, \\ \delta v_{1y} &= -\delta v_1 \cos \theta \sin \varphi, \\ \delta v_{1z} &= -\delta v_1 \cos \varphi. \end{aligned} \quad (105)$$

Thanks to isotropy, the dependence on the angle  $\psi$  has been eliminated, and this is all we need to convert the original 3D

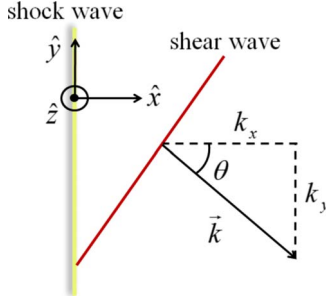


FIG. 8. (Color online) A planar shear wave with wave number  $\vec{k}$  intersects a planar shock wave with an incidence angle  $\theta$ . The shock moves from left to right along the  $\hat{x}$ -axis.

situation into an equivalent 2D problem. This trick had been also noticed in earlier works [30]. In Fig. 8 we show the geometry corresponding to an incident shear wave with wave-number vector  $\vec{k}$  that is hit by the incident shock wave. The incidence angle  $\theta$  is shown as the angle formed by  $\vec{k}$  and the  $\hat{x}$  axis.

We also write the components of the vorticity upstream in the rotated system of coordinates,

$$\begin{aligned}\delta\omega_{1x} &= k\delta v_1 \sin\theta \cos\varphi, \\ \delta\omega_{1y} &= k\delta v_1 \cos\theta \cos\varphi, \\ \delta\omega_{1z} &= -k\delta v_1 \sin\varphi,\end{aligned}\quad (106)$$

where we see that only the angles  $\theta$  and  $\varphi$  are necessary. As before, the mean values of the new components of the upstream velocity and vorticity are easily calculated, taking into account that the probability of having a given orientation  $\theta, \varphi$  is proportional to the new solid angle, which is equal to:  $\sin\theta d\theta d\varphi / (4\pi)$ . We get

$$\begin{aligned}\langle\delta v_{1x}^2\rangle &= \frac{\delta v_1^2}{3}, \langle\delta v_{1y}^2\rangle = \frac{\delta v_1^2}{6}, \langle\delta v_{1z}^2\rangle = \frac{\delta v_1^2}{2}, \\ \langle\delta\omega_{1x}^2\rangle &= \frac{(k\delta v_1)^2}{3}, \langle\delta\omega_{1y}^2\rangle = \frac{(k\delta v_1)^2}{6}, \langle\delta\omega_{1z}^2\rangle = \frac{(k\delta v_1)^2}{2}.\end{aligned}\quad (108)$$

The new axes are not equivalent to the old ones, and hence, the average on each direction is different (except for the  $x$  direction), but their sum is invariant. Regarding the components of the vectors downstream, we realize that in the new set of rotated axes  $\{x, y, z\}$ , there is no  $z$  component for the wave-number vector. This means, physically, that the shock front ripple does not depend on the coordinate  $z$ , and thus its partial derivative  $\partial/\partial z$  is identically zero. Then, thanks to the conservation of tangential momentum across the front [7,37], the upstream  $z$  component of the velocity is conserved:  $\delta v_{2z} = \delta v_{1z}$ . In consequence, we only need to understand how the other two components  $\delta v_{1x}$  and  $\delta v_{1y}$  transform across the shock. Therefore, the original 3D problem has been reduced to the interaction of a shock with a 2D vorticity field in the new system of coordinates. The new wave-number vector in the equivalent two-dimensional problem is

$(k \cos\theta, -k \sin\theta)$ . The value of  $\zeta_0$  given in Eq. (100) can be re-expressed in terms of  $\theta$ ,

$$\zeta_0 = \frac{RM_2}{\sqrt{1-M_2^2}} \frac{1}{|\tan\theta|}. \quad (109)$$

Each choice of the ‘‘incidence’’ angle  $\theta$  defines a set of shear waves in front of the shock (the elements within this set have different values of the angle  $\varphi$ ). It is also easy to see that the intervals  $0 \leq \theta \leq \pi/2$  and  $\pi/2 \leq \theta \leq \pi$  are physically indistinguishable. Besides, the value  $\zeta_0=1$  defines a critical value for the incidence angle of the shear wave upstream, which we call  $\theta_{cr}$ . For angles of incidence greater than  $\theta_{cr}$ , the pressure perturbations behind the shock front are evanescent, as they would be associated to values  $\zeta_0 < 1$ . On the other hand, for  $\theta < \theta_{cr}$ , the shock oscillates and radiates traveling sound waves downstream, in agreement with previous works [12,14–18,20,21]. The value of  $\theta_{cr}$  is given by

$$\sin\theta_{cr} = M_1^2 \sqrt{\frac{\gamma+1}{2\gamma M_1^4 + (3-\gamma)M_1^2 - 2}}. \quad (110)$$

Furthermore, we note that the dimensionless velocity factor of the upstream field  $u_1$  defined for the single-mode 2D problem before, is changed into  $\tilde{v}_{1k} \sin\theta \sin\varphi$  for the 3D problem. The normalization  $\tilde{v}_{1k} = v_{1k}/c_2$  is understood, and the subindex  $k$  indicates the dependence of the quantity  $v_1$  on  $k=|\vec{k}|$ .

### C. Interaction of a shock with a 3D turbulent velocity field: average kinetic energy of the downstream perturbations

We deal now with a fully random 3D preshock vorticity field, for which we have the representation given by Eqs. (104)–(106). The rotational velocities downstream are given by

$$\begin{aligned}|\delta v_{2x}^{rot}| &= c_2 \tilde{v}_{1k} |Q_{rot}(\gamma, M_1, \zeta_0)| \sin\theta \sin\varphi, \\ |\delta v_{2y}^{rot}| &= c_2 \tilde{v}_{1k} R \frac{k_x}{k_y} |Q_{rot}(\gamma, M_1, \zeta_0)| \sin\theta \sin\varphi, \\ |\delta v_{2z}^{rot}| &= |\delta v_{1z}|,\end{aligned}\quad (111)$$

for arbitrary values of  $\varphi$  and  $\theta$  in the intervals  $0 \leq \varphi < 2\pi$  and  $0 \leq \theta < \pi$ . The function  $Q_{rot}$  is defined with the aid of Eqs. (79) and (81).

By analogy, we have for the sound waves emitted downstream

$$\begin{aligned}|\delta v_{2x}^{ac}| &= c_2 \tilde{v}_{1k} |Q_{ac}(\gamma, M_1, \zeta_0)| \sin\theta \sin\varphi, \\ |\delta v_{2y}^{ac}| &= c_2 \tilde{v}_{1k} \frac{|Q_{ac}(\gamma, M_1, \zeta_0)|}{\sqrt{\zeta_1^2 - 1}} \sin\theta \sin\varphi, \\ |\delta v_{2z}^{ac}| &= 0,\end{aligned}\quad (112)$$

where  $Q_{ac}$  is given in Eq. (60). From now on, we denote any dimensionless velocity component  $j$ , in the compressed fluid as  $\tilde{v}_{2j} = \delta v_{2j}/c_2$ . We can write the dimensionless kinetic en-

ergy (per unit mass) of the compressed fluid elements, associated to the rotational part of the velocity field, as an explicit function of the orientation angles  $\theta$  and  $\varphi$ , the isentropic exponent  $\gamma$ , and the shock Mach number  $M_1$ ,

$$\begin{aligned} \tilde{T}_{3D}^{rot} &= \frac{1}{2}[(\tilde{v}_{2x}^{rot})^2 + (\tilde{v}_{2y}^{rot})^2 + (\tilde{v}_{2z}^{rot})^2], \\ &= \frac{\tilde{v}_{1k}^2}{2} \left\{ \left[ 1 + \left( R \frac{k_x}{k_y} \right)^2 \right] |Q_{rot}|^2 \sin^2 \theta \sin^2 \varphi + \cos^2 \varphi \right\}, \end{aligned} \quad (113)$$

where we used the fact that  $\tilde{v}_{2z}^{rot} = \tilde{v}_{1z}^{rot} = \tilde{v}_{1k} \cos \varphi$ , according to the discussion following Eqs. (107) and (108). We proceed similarly to the sound waves' contribution to the kinetic energy,

$$\begin{aligned} \tilde{T}_{3D}^{ac} &= \frac{1}{2}[(\tilde{v}_{2x}^{ac})^2 + (\tilde{v}_{2y}^{ac})^2], \\ &= \frac{\tilde{v}_{1k}^2}{2} e_s^2 \sin^2 \theta \sin^2 \varphi. \end{aligned} \quad (114)$$

Equations (113) and (114) give the kinetic energies (rotational and potential) of the compressed fluid elements, for a single choice of the incidence angles  $\theta$  and  $\varphi$ . As we have not considered viscosity in the equations of motion and the boundary conditions at the shock, these expressions do not take into account the viscous decay that would inevitably occur far downstream [35]. For a shock interacting with a full spectrum of shear/vorticity waves, we can calculate the statistical averages of the interesting quantities, by averaging over the angles  $\theta$  and  $\varphi$ . The averages so obtained would be valid not very far from the shock front, so that viscosity did not have enough time to act on the fluid particles [12,14–18,20,35]. To get the average of the kinetic energy we multiply Eqs. (113) and (114) by the probability density for a uniform distribution on the unit sphere, given by  $\sin \theta d\theta d\varphi / (4\pi)$  and integrate over the angles. It is also convenient to express the integral over  $\theta$  as an integral over the variable  $\zeta_0$ . Using Eq. (109), it can be seen that

$$\sin^3 \theta d\theta = \frac{M_1^4 R^2 \sqrt{M_1^2 - 1}}{[RM_1^2 + (M_1^2 - 1)\zeta_0^2]^{5/2}} d\zeta_0. \quad (115)$$

We define the kinetic energy amplification factor for the rotational part

$$\begin{aligned} A_{3D}^{rot}(\gamma, M_1) &= \frac{2\langle \tilde{T}_2^{rot} \rangle_{\theta, \varphi}}{\tilde{v}_{1k}^2} \\ &= \frac{1}{2} \int_0^\infty \left[ \frac{|Q_{rot}|^2 [(M_1^2 - 1)R\zeta_0^2 + M_1^2] M_1^2 R^2 \sqrt{M_1^2 - 1}}{[RM_1^2 + (M_1^2 - 1)\zeta_0^2]^{5/2}} \right] d\zeta_0 \\ &\quad + \frac{1}{2}. \end{aligned} \quad (116)$$

The term 1/2 comes from the average of the  $z$  component,

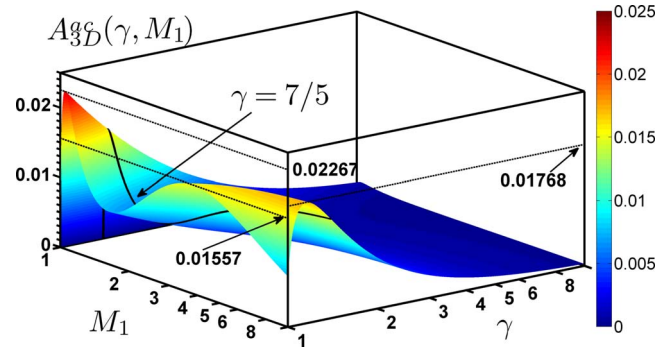


FIG. 9. (Color online) Sonic contribution to the kinetic-energy amplification factor as a function of  $\gamma$  and  $M_1$  [Eq. (117)].

which is conserved through compression. Thus, one half of the kinetic energy per unit mass is not modified across the shock front. We do similarly for the contribution of the sound waves,

$$A_{3D}^{ac}(\gamma, M_1) = \frac{2\langle \tilde{T}_2^{ac} \rangle_{\theta, \varphi}}{\tilde{v}_{1k}^2} = \frac{1}{2} \int_1^\infty \frac{e_s^2 M_1^4 R^2 \sqrt{M_1^2 - 1}}{[RM_1^2 + (M_1^2 - 1)\zeta_0^2]^{5/2}} d\zeta_0. \quad (117)$$

We define the total turbulent kinetic-energy amplification factor across the shock front as

$$A_{3D}(\gamma, M_1) = A_{3D}^{rot}(\gamma, M_1) + A_{3D}^{ac}(\gamma, M_1). \quad (118)$$

In [57], Appendix C, we show the closed-form analytical expressions for both  $A_{3D}^{rot}$  and  $A_{3D}^{ac}$ , as a function of  $\gamma$  and  $M_1$ . The amplification factor  $A_{3D}$  can then be calculated either after a numerical evaluation of Eqs. (116)–(118), or using the analytical expressions shown in [57], Appendix C. This is the first time that complete and explicit formulas are presented for the energy amplification factor across a shock front interacting with a weakly turbulent compressible fluid. The same will be shown for the other quantities of interest, in the following subsections. In Fig. 9 we show the acoustic waves' contribution to the kinetic-energy amplification factor as a function of  $\gamma$  and  $M_1$ . We can clearly see an interesting topography for the 2D surface in the weak-shock limit and highly compressible fluids, where a double peak structure is evident. The exact asymptotic scalings, characterizing these mathematical structures, will be discussed later on in the following sections. We show the amplification factors (long/short-wavelength intervals, acoustic contribution and total) at different Mach numbers for several ideal gases in [57], Table I in Appendix F, inside the auxiliary file. In Fig. 10 we plot the total amplification factor for an incident shock moving into air ( $\gamma=7/5$ ) given by Eq. (118) and compare it with recent experiments and direct numerical simulations. The experimental result at  $M_1=3$  is taken from [40]. The simulation results are taken from [30]. The agreement with the experiments and simulations is seen to be very good. The theoretical curve is also compared with simulation curves obtained with the CALE code by means of adjustable drag coefficients, as reported in [35]. The kinetic-energy amplification predicted by CALE as a function of  $M_1$  is approximated by a

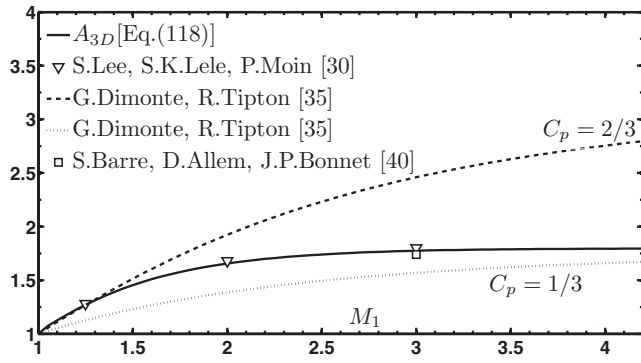


FIG. 10. Kinetic-energy amplification factor [Eq. (118)] for a shock moving into air ( $\gamma=7/5$ ), as a function of the shock strength. We compare with recently published results: experiments from [40], and numerical simulations from [30,35].

simple formula  $R C_p$  [35], where  $R = \rho_2 / \rho_1$  is the density compression ratio [Eq. (1)] across the shock front, and  $C_p$  is a heuristic drag coefficient. As can be inferred from the plots, the kinetic energy seems to be amplified across a shock moving into an ideal gas and reaches an asymptotic value for very strong shocks, which is dependent on the value of  $\gamma$ . In Fig. 11 we show the different contributions to  $A_{3D}$  for a shock moving into air, as a function of the shock Mach number  $M_1$ . We can see that for weak shocks, the short-wavelengths part of the upstream spectrum contributes the most to the kinetic-energy amplification. As the shock-strength increases and the Mach number stays above 1.3, both contribute approximately the same. The sound waves contribution to the kinetic-energy budget downstream is negligible. The long and short-wavelength integrals for the rotational contribution ( $A_{3D}^l$ , and  $A_{3D}^s$ ) are calculated explicitly in [57], Appendix C. There are other related questions that we may answer, taking profit of the analytical model presented here. In fact, it is natural to ask whether the kinetic energy gets amplified without bounds as the shock strength increases, or if it saturates at some finite value. What is the behavior for highly compressible gases and very strong shocks? Does it peak at some finite value? It would be natural to think that the increase in the kinetic energy must be

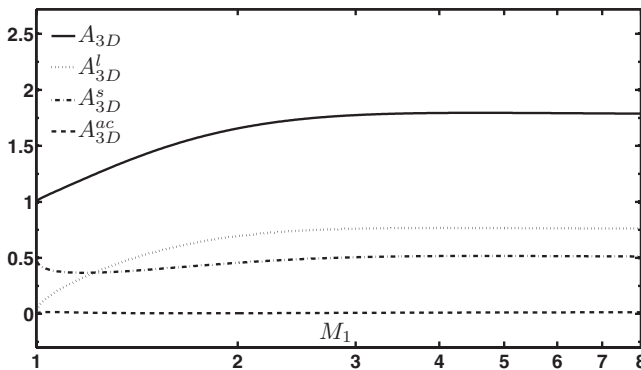


FIG. 11. Comparison between the long/short wavelength and acoustic contributions to the total kinetic-energy amplification coefficient for a shock moving into air ( $\gamma=7/5$ ), as a function of the shock Mach number  $M_1$ .

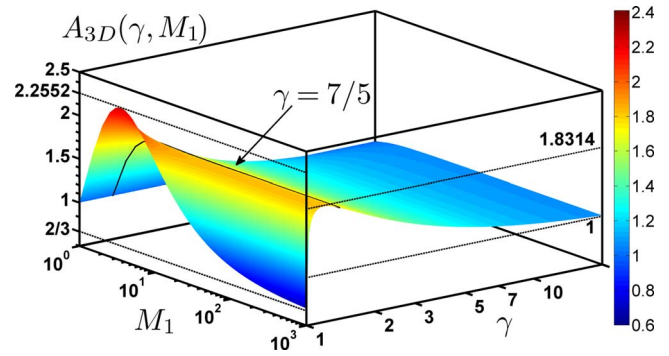


FIG. 12. (Color online) Behavior of the total kinetic-energy amplification factor [Eq. (118)] as a function of  $\gamma$  and the shock Mach number  $M_1$ .

larger the more compressible the gas. To have an idea of the behavior of the amplification coefficient in the space of parameters, we show a two-dimensional logarithmic plot, where the coefficient  $\gamma$  and the shock Mach number  $M_1$  are varied within the limits  $1 \leq \gamma \leq 20$  and  $1 \leq M_1 \leq 1000$ , in Fig. 12. We can clearly recognize the curve corresponding to the one shown in Fig. 10, shown as a black curve superposed on the 3D surface.

Furthermore, we see the interesting result that for  $\gamma$  very near unity and very strong shocks, the kinetic energy gets reduced, instead of being amplified. The asymptotic value obtained in that limit is actually  $2/3$  which can be easily predicted noting that for a highly compressible fluid and a very strong shock, the shock ripple amplitude and the value of  $v_{2x}$  go simultaneously to zero. As the shock would not add additional  $y$ -velocity perturbations to those already existing upstream, and as the  $z$  component does not change, the total average is just the sum of  $1/6$  (corresponding to the average in the  $y$  direction) plus  $1/2$  (from the  $z$  component). The tendency of decreasing the kinetic energy instead of amplifying it as we approach the most compressible conditions can also be understood by examining the two contributions to the vorticity in the equivalent 2D problem. In fact, we have to go back to Eqs. (64) and (65). The first term in Eq. (64) always corresponds to an amplification of the upstream eddy. The second term is due to the shock oscillation dynamics, and hence, is always present whenever the shock surface is cor-

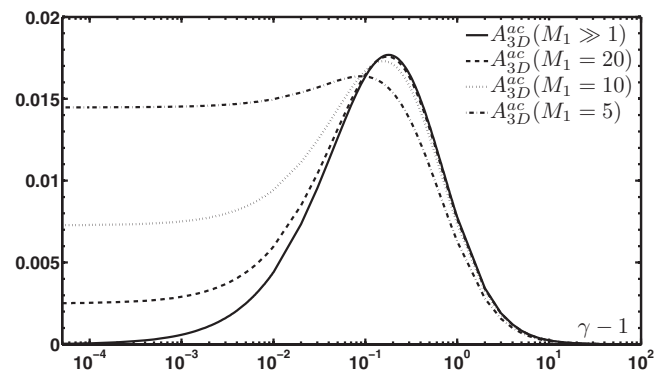


FIG. 13. Strong-shock asymptotic of the acoustic contribution to the kinetic-energy amplification factor [Eq. (121)]. We also show different curves corresponding to shocks of finite strength.

rugated, as is usually the case in RMI-like flows. For the problem considered in this work, this second term has opposite phase with respect to the first term, in most of the spectrum, giving rise to the possibility of negative interference between them. This effect is seen in the sums  $\Omega_1 + \Omega_2 e_{lr}$  and  $\Omega_1 + \Omega_2 e_{rs}$ , which appear in the expressions for  $Q_{rot}^l$  and  $Q_{rot}^s$  in Eqs. (79) and (81). As will be seen in [57], Appendix C, it is the interference between the  $\Omega_1$  and  $\Omega_2$  terms (both in the short and in the long-wavelength regimes) that can give rise to a decrease in the energy content of the downstream eddies as compared to the upstream vorticity. This interference is positive only within very narrow ranges of values of  $\gamma$  and  $M_1$ , and only for  $\theta$  close to  $\theta_{cr}$ .

With the help of the analytical expressions obtained in [57], Appendix C, we can get the approximations corresponding to different physical limits and show their explicit dependence on  $\gamma$  and  $M_1$ . We show at first the strong-shock limit of the kinetic-energy amplification, as an explicit function of  $\gamma$ . In fact, taking the corresponding limit  $M_1 \rightarrow \infty$  either in the defining integrals, or in the analytical expressions in [57], Appendix C, we get the asymptotics of the different contributions to the amplification factor. We show at first the strong-shock asymptotics. The results for the long ( $0 \leq \xi_0 \leq 1$ ) and short ( $1 \leq \xi_0 < \infty$ ) wavelength intervals of the rotational contribution are, respectively,

$$A_{3D}^l(\gamma, M_1 \gg 1) \cong \frac{1}{2} \left[ (2 - \gamma) \ln \frac{\gamma + 1}{\gamma - 1} + \frac{(\gamma - 1)(12\gamma^2 + 15\gamma - 1)}{6\gamma(\gamma + 1)^2} \right] \sqrt{2\gamma(\gamma - 1)}, \quad (119)$$

$$\begin{aligned} A_{3D}^s(\gamma, M_1 \gg 1) \cong & \frac{(\gamma - 1)(\gamma + 1)^2}{\sqrt{\gamma}(2\gamma - 1)^2} \tan^{-1} \left( \frac{1}{\sqrt{\gamma}} \right) + \frac{(2 - \gamma)(10\gamma^4 - 23\gamma^3 + 16\gamma^2 - 3\gamma - 1)}{(2\gamma - 1)^2} \sqrt{2\gamma(\gamma - 1)} \\ & \times \ln \left[ \frac{\gamma(\gamma - 1) + \sqrt{2\gamma(\gamma - 1)}}{\gamma(\gamma + 1)} \right] + \frac{60\gamma^6 - 108\gamma^5 - 98\gamma^4 + 178\gamma^3 + 25\gamma^2 - 56\gamma + 3}{6(2\gamma - 1)(\gamma + 1)^2} \\ & - \frac{120\gamma^6 - 156\gamma^5 - 284\gamma^4 + 222\gamma^3 + 165\gamma^2 - 46\gamma - 5}{12(2\gamma - 1)(\gamma + 1)^2} \sqrt{\frac{2(\gamma - 1)}{\gamma}}, \end{aligned} \quad (120)$$

and the strong-shock asymptotic of the acoustic waves' contribution is ( $1 \leq \xi_0 < \infty$ )

$$\begin{aligned} A_{3D}^{ac}(\gamma, M_1 \gg 1) \cong & (\gamma - 1)^{5/2} (5\gamma^2 - 10\gamma + 2) \sqrt{2\gamma} \ln \left[ \frac{\gamma(\gamma - 1) + \sqrt{2\gamma(\gamma - 1)}}{\gamma(\gamma + 1)} \right] - \frac{2(\gamma - 1)}{3(\gamma + 1)^2} (15\gamma^5 - 15\gamma^4 - 29\gamma^3 + 21\gamma^2 + 10\gamma - 6) \\ & + \frac{(\gamma - 1)^{3/2}}{3(\gamma + 1)^2} \sqrt{\frac{2}{\gamma}} (30\gamma^5 - 15\gamma^4 - 68\gamma^3 + 8\gamma^2 + 25\gamma - 2). \end{aligned} \quad (121)$$

The asymptotic curve given by Eq. (121) is shown in Fig. 13, together with the acoustic contribution at other large but finite strengths as a function of  $\gamma$ .

Collecting all the terms together and rearranging, we get the strong-shock limit of the total kinetic-energy amplification factor, as an explicit function of  $\gamma$ ,

$$\begin{aligned} A_{3D}(\gamma, M_1 \gg 1) \cong & - \frac{60\gamma^7 - 180\gamma^6 + 58\gamma^5 + 277\gamma^4 - 236\gamma^3 - 59\gamma^2 + 84\gamma - 12}{3(2\gamma - 1)(\gamma + 1)^2} \\ & + \frac{60\gamma^7 - 150\gamma^6 - 22\gamma^5 + 282\gamma^4 - 99\gamma^3 - 121\gamma^2 + 47\gamma - 1}{3(2\gamma - 1)(\gamma + 1)^2} \sqrt{\frac{2(\gamma - 1)}{\gamma}} \\ & + \gamma \sqrt{2\gamma(\gamma - 1)} \frac{(2\gamma - 3)(10\gamma^4 - 40\gamma^3 + 58\gamma^2 - 36\gamma + 9)}{(2\gamma - 1)^2} \\ & \times \ln \left[ \frac{\gamma(\gamma - 1) + \sqrt{2\gamma(\gamma - 1)}}{\gamma(\gamma + 1)} \right] + (2 - \gamma) \sqrt{\frac{\gamma(\gamma - 1)}{2}} \ln \left( \frac{\gamma + 1}{\gamma - 1} \right) + \frac{(\gamma - 1)(\gamma + 1)^2}{(2\gamma - 1)^2 \sqrt{\gamma}} \tan^{-1} \left( \frac{1}{\sqrt{\gamma}} \right). \end{aligned} \quad (122)$$

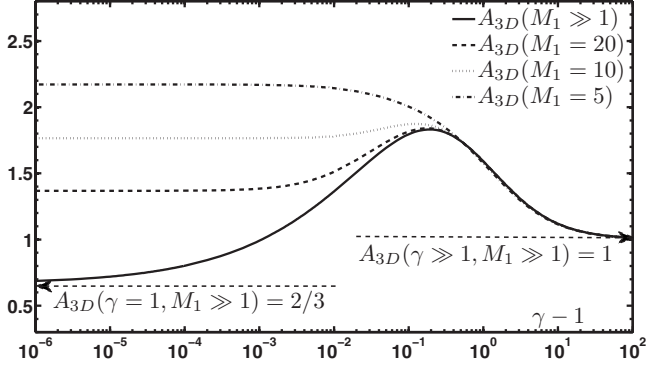


FIG. 14. Kinetic-energy amplification coefficient limiting curve for very strong shocks as a function of  $\gamma$ . We also show different curves corresponding to shocks of finite strength.

The result given by [Eq. (122)] is shown in Fig. 14, where we also show different curves corresponding to strong shocks with  $M_1 \geq 5$ . The analytical expressions of the integrals for finite values of  $M_1$  can be found in [57], Appendix C. The amplification factor reaches its maximum on the  $M_1 = \infty$  curve, equal to 1.831 43, at  $\gamma = 1.190$  39. For very high values of  $\gamma$  the amplification tends to unity because the

shock wave leaves the upstream vorticity unchanged for poorly compressible fluids,

$$A_{3D}(\gamma \gg 1, M_1 \gg 1) \cong 1 + \frac{4}{3\gamma} + \frac{4(34 - 27\sqrt{2})}{105\gamma^2} + O\left(\frac{1}{\gamma^3}\right). \quad (123)$$

In the opposite limit of high compressibility ( $\gamma - 1 \ll 1$ ), the amplification coefficient goes through unity (at  $\gamma = 1.001$  07) to reach the asymptotic value  $2/3$  at  $\gamma \rightarrow 1$ , as discussed above. The asymptotic expression of the amplification factor in this limit is

$$A_{3D}(\gamma - 1 \ll 1, M_1 \gg 1) \cong \frac{2}{3} + \sqrt{2} \left( \ln 2 - \frac{1}{3} \right) \sqrt{\gamma - 1} - \sqrt{2} \ln(\gamma - 1) \sqrt{\gamma - 1} + O(\gamma - 1). \quad (124)$$

Other interesting limit is the highly compressible case ( $\gamma \rightarrow 1$ ) considered as a function of  $M_1$ . The amplification coefficient of the different contributions can be obtained as before, directly from the defining integrals or from the explicit analytical expressions derived in [57], Appendix C. For the rotational contribution, we get for both, long- and short-wavelength intervals,

$$A_{3D}^l(\gamma = 1, M_1) \cong \frac{\sqrt{M_1^2 - 1}(25M_1^{10} + 12M_1^8 - 37M_1^6 + 8M_1^4 + 6M_1^2 - 2)}{6(M_1^4 + M_1^2 - 1)^{3/2}(M_1^2 + 1)^2 M_1^4} + \frac{2M_1^2(M_1^2 - 1)}{(M_1^2 + 1)^{5/2}} \ln \left( \frac{\sqrt{M_1^4 - 1} + \sqrt{M_1^4 + M_1^2 - 1}}{M_1} \right), \quad (125)$$

$$\begin{aligned} A_{3D}^s(\gamma = 1, M_1) \cong & \frac{(M_1 - 1)}{6M_1^4(M_1^2 + 1)^4(M_1^4 + M_1^2 - 1)} (M_1^{15} + 9M_1^{14} - 6M_1^{13} + 22M_1^{12} + 13M_1^{11} - 75M_1^{10} + 53M_1^9 - 23M_1^8 - 10M_1^7 \\ & + 142M_1^6 - 37M_1^5 - 85M_1^4 + 8M_1^3 + 8M_1^2 + 2M_1 + 2) - \frac{\sqrt{M_1^2 - 1}}{6M_1^4(M_1^2 + 1)^4(M_1^4 + M_1^2 - 1)^{3/2}} (12M_1^{16} - 23M_1^{14} \\ & - 50M_1^{12} + 156M_1^{10} + 42M_1^8 - 199M_1^6 + 94M_1^4 - 6M_1^2 - 2) + \frac{2(M_1^2 - 1)(M_1^6 - 3M_1^4 - 6M_1^2 + 4)}{(M_1^2 + 1)^{9/2}} \\ & \times \ln \left[ \frac{(\sqrt{M_1^4 + M_1^2 - 1} + \sqrt{M_1^4 - 1})(1 + M_1 \sqrt{M_1^2 + 1})}{(1 + \sqrt{M_1^2 + 1})\sqrt{M_1^4 + M_1^2 - 1}} \right] + \frac{4M_1^8}{\sqrt{M_1^2 - 1}(M_1^2 + 1)^{9/2}} \\ & \times \left[ \tan^{-1}(\sqrt{M_1^4 - 1}) + \tan^{-1}\left(\frac{\sqrt{M_1^4 - 1}}{M_1}\right) - \tan^{-1}\left(\frac{(M_1^2 - 1)\sqrt{M_1^2 + 1}}{\sqrt{M_1^4 + M_1^2 - 1}}\right) \right], \end{aligned} \quad (126)$$

and the acoustic waves' contribution is given by

$$\begin{aligned} A_{3D}^{ac}(\gamma = 1, M_1) \cong & \frac{4}{3M_1^2(M_1^2 - 1)(M_1 + 1)(M_1^2 + 1)^3(M_1^4 + M_1^2 - 1)} (M_1^{13} - 3M_1^{12} + 7M_1^{11} - 5M_1^{10} + 5M_1^9 + 25M_1^8 - 14M_1^7 + 20M_1^6 \\ & - 9M_1^5 - 33M_1^4 + 5M_1^3 + 5M_1^2 + M_1 + 1) - \frac{2(3M_1^{14} + 41M_1^{12} + 58M_1^{10} - 80M_1^8 - 77M_1^6 + 77M_1^4 - 8M_1^2 - 2)}{3M_1^2(M_1^2 - 1)^{3/2}(M_1^2 + 1)^3(M_1^4 + M_1^2 - 1)^{3/2}} \\ & + \frac{8M_1^2(2M_1^4 + 3M_1^2 - 4)}{(M_1^2 - 1)^2(M_1^2 + 1)^{7/2}} \ln \left[ \frac{(\sqrt{M_1^4 + M_1^2 - 1} + \sqrt{M_1^4 - 1})(1 + M_1 \sqrt{M_1^2 + 1})}{(1 + \sqrt{M_1^2 + 1})\sqrt{M_1^4 + M_1^2 - 1}} \right]. \end{aligned} \quad (127)$$

In Fig. 15 we show the prediction of Eq. (127) for  $\gamma=1$  and other gases with  $\gamma$  values near unity, as a function of the shock strength. The total amplification factor in the limit  $\gamma=1$  is given below,

$$\begin{aligned}
A_{3D}(\gamma=1, M_1) \cong & \frac{1}{3M_1^4(M_1-1)(M_1+1)^2(M_1^2+1)^4(M_1^4+M_1^2-1)} (2M_1^{19} + 6M_1^{18} + 6M_1^{17} - 4M_1^{16} + 51M_1^{15} - 81M_1^{14} + 54M_1^{13} \\
& + 150M_1^{12} - 98M_1^{11} + 226M_1^{10} - 77M_1^9 - 251M_1^8 + 23M_1^7 + 51M_1^6 - 24M_1^4 + 6M_1^3 + 6M_1^2 + M_1 + 1) \\
& - \frac{2}{3M_1^2(M_1^2+1)^4(M_1^2-1)^{3/2}(M_1^4+M_1^2-1)^{3/2}} (3M_1^{18} - 15M_1^{16} + 43M_1^{14} + 179M_1^{12} - 98M_1^{10} - 215M_1^8 + 135M_1^6 \\
& - 17M_1^4 + 13M_1^2 - 4) + \frac{2(M_1^{12} - 6M_1^{10} + 14M_1^8 + 32M_1^6 - 31M_1^4 + 2M_1^2 - 4)}{(M_1^2-1)^2(M_1^2+1)^{9/2}} \\
& \times \ln \left[ \frac{(\sqrt{M_1^4-1} + \sqrt{M_1^4+M_1^2-1})(1+M_1\sqrt{M_1^2+1})}{(1+\sqrt{M_1^2+1})\sqrt{M_1^4+M_1^2-1}} \right] + \frac{2M_1^2(M_1^2-1)}{(M_1^2+1)^{5/2}} \ln \left( \frac{\sqrt{M_1^4-1} + \sqrt{M_1^4+M_1^2-1}}{M_1} \right) \\
& + \frac{4M_1^8}{(M_1^2+1)^{9/2}\sqrt{M_1^2-1}} \left\{ \tan^{-1}(M_1^4-1) - \tan^{-1} \left[ \frac{(M_1^2-1)\sqrt{M_1^2+1}}{\sqrt{M_1^4+M_1^2-1}} \right] + \tan^{-1} \left( \frac{\sqrt{M_1^4-1}}{M_1} \right) \right\}. \quad (128)
\end{aligned}$$

In Fig. 16 a plot of the last formula is shown, with other curves obtained for  $\gamma$  values near 1.

The function has a maximum equal to 2.25519 at  $M_1 = 3.5116$ . It reaches the value  $2/3$  for very large values of  $M_1$ , and the expansion in powers of  $1/M_1$  is

$$A_{3D}(\gamma-1 \ll 1, M_1 \gg 1) \cong \frac{2}{3} + \frac{12 \ln(2M_1) - 2}{3M_1} + O\left(\frac{1}{M_1^2}\right). \quad (129)$$

For very weak shocks and highly compressible gases, Eq. (128) has the expansion

$$\begin{aligned}
A_{3D}(\gamma-1 \ll 1, M_1-1 \ll 1) \\
\cong 1 + \frac{2\sqrt{2}}{15} \sqrt{M_1-1} + O(M_1-1). \quad (130)
\end{aligned}$$

In the very weak-shock limit, and for arbitrary  $\gamma$ , the main contribution comes from the sound waves ( $\sim \sqrt{M_1-1}$ ),

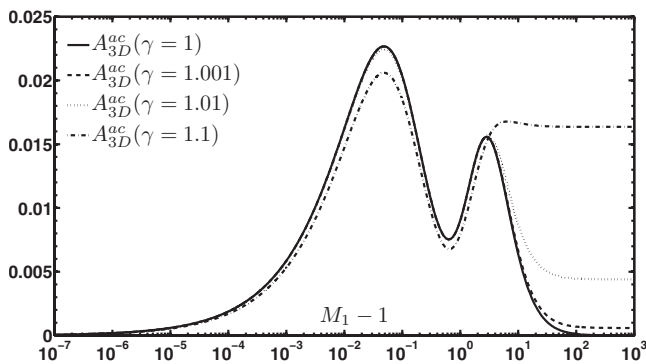


FIG. 15. Acoustic contribution to the kinetic-energy amplification coefficient as a function of the shock strength for a highly compressible gas  $\gamma=1$  [Eq. (127)], and for other gases with  $\gamma$  near unity [Eq. (117)].

as the rotational contribution is smaller in that limit [ $\sim (M_1-1)$ ]. In fact, we have

$$A_{3D}(\gamma, M_1-1 \ll 1) \cong 1 + \frac{8\sqrt{2}}{15(\gamma+1)^2} \sqrt{M_1-1} + O(M_1-1). \quad (131)$$

#### D. Root mean square of the sound wave pressure perturbations downstream

We can also compute the average of the square of the pressure perturbations in the short-wavelength interval, together with the entropic density perturbations.

##### 1. Pressure fluctuations

The corrugated shock will emit traveling sound waves downstream for wavelengths short enough, which corresponds to incident angles  $0 \leq \theta \leq \theta_{cr}$  ( $1 \leq \zeta_0 < \infty$ ). For this

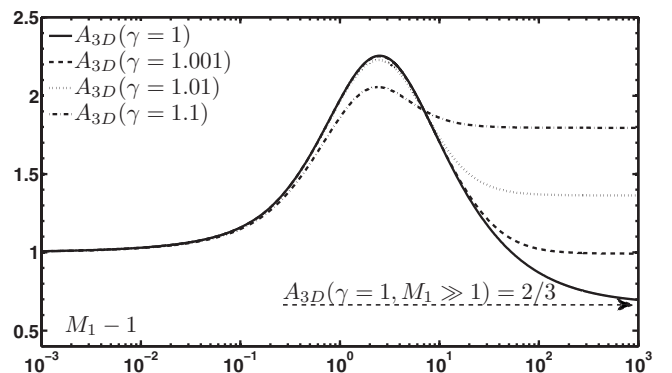


FIG. 16. Total kinetic-energy amplification coefficient as a function of the shock strength for a highly compressible gas  $\gamma=1$  [Eq. (128)], and for other gases with  $\gamma$  near unity [Eq. (118)].

part of the spectrum we can calculate the root mean square of the dimensionless pressure fluctuations associated to the traveling acoustic fronts,

$$\Pi_2 = \sqrt{\frac{\langle \tilde{p}_2^2 \rangle}{\tilde{v}_{1k}^2}} = \sqrt{\frac{1}{2} \int_1^\infty \frac{e_s^2 M_1^4 R^2 \sqrt{M_1^2 - 1}}{[RM_1^2 + (M_1^2 - 1)\zeta_0^2]^{5/2}} d\zeta_0}. \quad (132)$$

The quantity inside the square root of the above equation can be easily recognized as the sonic contribution to the amplification factor  $A_{3D}^{ac}$  given in Eq. (117). Hence, all the results shown in the previous subsection for the sonic contribution are valid for the behavior of  $\Pi_2$  as a function of  $\gamma$  and  $M_1$ , and will not be repeated here. The maxima and minima of  $\Pi_2$  occur at the same values of  $\gamma$  and  $M_1$  as those shown in Fig. 13. The only difference is the height of the surface, due to the square root in Eq. (132). The exact asymptotics in the different interesting physical limits can be deduced from the expressions for  $A_{3D}^{ac}$ . We only note here that, using Eq. (131), we obtain the weak-shock scaling:  $\Pi_2 \sim (M_1 - 1)^{1/4}$ , in agreement with [15],

$$\begin{aligned} \Pi_2(\gamma, M_1 - 1 \ll 1) \\ \cong \frac{2^{7/4}}{\sqrt{15}(\gamma + 1)} (M_1 - 1)^{1/4} + O[(M_1 - 1)^{5/4}]. \end{aligned} \quad (133)$$

### E. Sound energy flux

As discussed in the previous section and also in [23], the generation of sonic perturbations by the corrugated shock is different in the long and short-wavelength regimes. As already discussed before, acoustic energy is being continuously radiated from the shock into the compressed fluid for any  $\zeta_0 > 1$ . In this section we will quantify the emission of sound energy as a function of the angle of emission, and as a function of  $\gamma$  and the shock strength  $M_1$ . We study the energy flux, as seen by an observer co-moving with the compressed fluid and also for an observer in the shock reference frame. An average over the angles of incidence  $\theta$  is performed and the results are compared with former predictions published in the literature [17].

#### 1. Energy flux in the compressed fluid reference frame

The energy flux which we denote by  $\vec{q}$ , which is transported by a planar sound wave in the frame of reference in which the fluid is at rest, is given by [37]

$$\vec{q} = c_2 E \hat{k}_{ac}, \quad (134)$$

where  $E$  is the energy density of the sound wave, equal to

$$E = \rho_2 c_2^2 \tilde{p}^2, \quad (135)$$

with  $\tilde{p}$  the pressure perturbation downstream, evaluated asymptotically in time. The unit vector  $\hat{k}_{ac}$  in the direction of propagation of the sound wave can be calculated with the aid of Eq. (55),

$$\begin{aligned} \hat{k}_{ac} &= \frac{k_x^{ac} \hat{x} + k_y \hat{y}}{\sqrt{(k_x^{ac})^2 + (k_y)^2}} = (\cos \theta_{ac}, \sin \theta_{ac}, 0) \\ &= \left( \frac{M_2 \zeta_0 - \sqrt{\zeta_0^2 - 1}}{\zeta_0 - M_2 \sqrt{\zeta_0^2 - 1}}, \frac{\sqrt{1 - M_2^2}}{\zeta_0 - M_2 \sqrt{\zeta_0^2 - 1}}, 0 \right). \end{aligned} \quad (136)$$

The projection of Eq. (134) along the direction of propagation of the shock front gives

$$q_x = \rho_2 c_2^3 \tilde{p}^2 \cos \theta_{ac}, \quad (137)$$

with  $\cos \theta_{ac}$  taken from Eq. (136) above. Positive values of  $q_x$  correspond to sound waves that follow the shock and negative values refer to sonic fronts that escape to the left. The amplitude of the traveling wavefronts can be retrieved from Eqs. (53) and (47). We can therefore write

$$q_x = \rho_2 c_2^3 \tilde{v}_1^2 e_s^2 \sin^2 \varphi \sin^2 \theta \cos \theta_{ac}. \quad (138)$$

For the sake of simplicity when comparing to previous results published in the literature, we normalize  $q_x$  above, expressing it in units of  $\rho_1 (\delta v_1)^2 D/2$ , which is the incident flux of turbulent kinetic energy upon a planar shock front that moves with velocity  $D\hat{x}$ . Using the auxiliary results

$$\sin^2 \theta = \frac{M_1^2 R}{M_1^2 R + (M_1^2 - 1)\zeta_0^2},$$

$$\rho_2 c_2^3 = \rho_1 c_1^3 \frac{(2\gamma M_1^2 - \gamma + 1)^{3/2} [(\gamma - 1)M_1^2 + 2]}{(\gamma + 1)^2}, \quad (139)$$

substituting into Eq. (138), and averaging over the polar angle  $\varphi$ , we obtain

$$\begin{aligned} \langle \tilde{q}_x \rangle_\varphi &= \frac{\langle q_x \rangle_\varphi}{\frac{1}{2} \rho_1 (\delta v_1)^2 D} \\ &= \frac{16 M_1^2 M_2 R (-M_2 \zeta_0 + \sqrt{\zeta_0^2 - 1})}{(\gamma + 1)^2 (\zeta_0 - M_2 \sqrt{\zeta_0^2 - 1}) [M_1^2 R + (M_1^2 - 1)\zeta_0^2]} \\ &\quad \times \left[ \frac{(M_1^2 - 1)^2 \zeta_0^2 - M_1^2}{M_1^2 - (M_1^2 + 1)\zeta_0^2 - 2M_2 M_1^2 \zeta_0 \sqrt{\zeta_0^2 - 1}} \right]^2. \end{aligned} \quad (140)$$

Before showing the behavior of the averaged energy flux as a function of the emission angle  $\theta_{ac}$ , it is convenient to have at hand the relationships that connect  $\theta_{ac}$  with the dimensionless frequency  $\zeta_0$ , and with the incidence angle of the upstream shear waves  $\theta$ . It is not difficult to get

$$\zeta_0(\theta_{ac}) = \frac{1}{\sqrt{1 - M_2^2}} \left( \frac{1 - M_2 \cos \theta_{ac}}{\sin \theta_{ac}} \right). \quad (141)$$

The interval  $\cos^{-1} M_2 \leq \theta_{ac} \leq \pi/2$  corresponds to the interval  $1 \leq \zeta_0 \leq 1/\sqrt{1 - M_2^2}$ , and hence, to right-facing sonic waves. On the other hand, the interval  $\pi/2 \leq \theta_{ac} \leq \pi$  corresponds to the interval  $\zeta_0 \geq 1/\sqrt{1 - M_2^2}$  for the left-facing sound waves. We recognize that the emitted energy is zero for  $\theta_{ac} = \pi/2$ , which is trivial, and for a particular value of  $\zeta_0$ ,

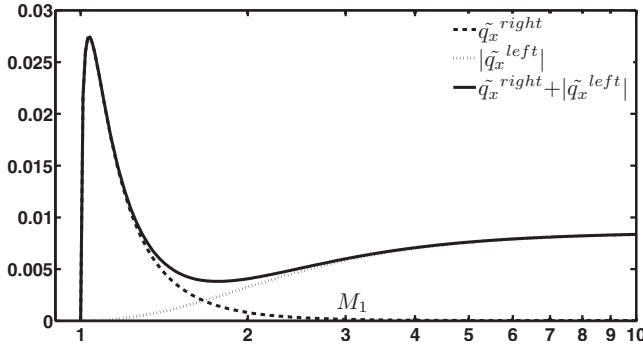


FIG. 17. Averaged longitudinal-acoustic flux emitted by a shock moving into air ( $\gamma=7/5$ ), as a function of the incident shock Mach number ( $M_1$ ) in the compressed fluid frame. We have also discriminated between the parts that corresponds to the right and left-facing sound waves.

$$\zeta_0^* = \frac{M_1}{\sqrt{M_1^2 - 1}}. \quad (142)$$

From the plot we deduce that the waves emitted to the right are more intense. As a general result, we see that the energy flux is never zero for  $\zeta_0=1$  in the reference frame of the compressed fluid at rest. Finally, let us calculate the average of the emitted flux over the incidence angle  $\theta$ . We define

$$\tilde{q}_x = \tilde{q}_x^{\text{right}} + \tilde{q}_x^{\text{left}}, \quad (143)$$

where the meaning of  $\tilde{q}_x^{\text{right}}$  and  $\tilde{q}_x^{\text{left}}$  is clear. We express the corresponding mean values as integrals over  $\zeta_0$ ,

$$\begin{aligned} \tilde{q}_x^{\text{right}} &= \int_1^{1/\sqrt{1-M_2^2}} \frac{\langle \tilde{q}_x \rangle_\varphi M_1^2 R \sqrt{M_1^2 - 1}}{[M_1^2 R + (M_1^2 - 1)\zeta_0^2]^{3/2}} d\zeta_0, \\ \tilde{q}_x^{\text{left}} &= \int_{1/\sqrt{1-M_2^2}}^\infty \frac{\langle \tilde{q}_x \rangle_\varphi M_1^2 R \sqrt{M_1^2 - 1}}{[M_1^2 R + (M_1^2 - 1)\zeta_0^2]^{3/2}} d\zeta_0. \end{aligned} \quad (144)$$

We plot both quantities in Fig. 17. We see that for weak shocks the energy is mainly directed to the right, while the opposite is true for stronger shocks.

## 2. Energy flux measured in the shock reference system

In some experimental conditions, the shock front may remain steady with respect to the laboratory walls, and it is the gas upstream that moves toward the shock [40]. Therefore, it is convenient to have the previous results expressed in the shock frame of reference. The modifications are minimal. In this system, the normal to the sound wave front (which coincides with  $\hat{k}_{ac}$ ) does not coincide with the direction of propagation of the energy. We write now the energy flux as

$$\vec{q} = \vec{v}_{ac} E_s, \quad (145)$$

where  $\vec{v}_{ac} = c_2 \hat{k}_{ac} + (U-D)\hat{x}$  and  $E_s$  is the energy density in the shock frame. According to [21], it is

$$E_s = (M_2 - \cos \theta_{ac}) E, \quad (146)$$

where  $E$  is given by Eq. (135). Collecting these results together, we get the dimensional energy flux in the shock

frame of reference, averaged over the angle  $\varphi$ ,

$$\langle q_x \rangle_\varphi = \frac{\rho_2 c_2^3}{2} e_s^2 \sin^2 \theta (1 - M_2 \cos \theta_{ac})(M_2 - \cos \theta_{ac}). \quad (147)$$

The above formula gives us the longitudinal flux in units of  $\rho_2 c_2^3$ . Let us express it, as before, in units of the turbulent intensity in front of the shock. After some additional algebra, we get, as an explicit function of  $\zeta_0$ ,

$$\begin{aligned} \langle q_x \rangle_\varphi &= \frac{1}{2} \rho_1 (\delta v_1)^2 D \\ &\times \frac{16 M_2 M_1^2 R (1 - M_2^2)^2 \zeta_0 \sqrt{\zeta_0^2 - 1}}{(\gamma + 1)^2 (\zeta_0 - M_2 \sqrt{\zeta_0^2 - 1})^2 [M_1^2 R + (M_1^2 - 1)\zeta_0^2]} \\ &\times \left[ \frac{(M_1^2 - 1)\zeta_0^2 - M_1^2}{M_1^2 - (M_1^2 + 1)\zeta_0^2 - 2M_1^2 M_2 \zeta_0 \sqrt{\zeta_0^2 - 1}} \right]^2. \end{aligned} \quad (148)$$

We note that in this reference frame, there is no need to distinguish between right facing or left-facing sound waves: for  $\zeta_0 \geq 1$  the shock oscillates and radiates all the waves to its left. The acoustic flux is zero for the same values of  $\zeta_0$  as before, but they correspond to different emission angles, as seen by an observer co-moving with the shock front. In fact, it is convenient to re-express the flux as a function of another angle  $\theta'$ , defined by the  $\hat{x}$  axis and the unit vector  $\hat{n}_{ac} = \vec{v}_{ac}/|\vec{v}_{ac}|$ . We get

$$\cos \theta' = \frac{\cos \theta_{ac} - M_2}{\sqrt{1 + M_2^2 - 2M_2 \cos \theta_{ac}}}. \quad (149)$$

When  $\zeta_0=1$  (that is,  $\cos \theta_{ac}=M_2$ ), it is easy to see that  $\theta' = \pi/2$ , and hence  $\langle q_x \rangle_\varphi = 0$ . When  $\zeta_0 = \infty$ , it is  $\theta_{ac} = \theta' = \pi$ , and we get  $\langle q_x \rangle_\varphi = 0$  again. It is only in the shock frame that the flux is zero when  $\zeta_0=1$  because  $\vec{v}_{ac}$ , the direction of propagation of energy, is perpendicular to the  $\hat{x}$  axis. However,  $\hat{k}_{ac} \neq 0$ , even for this value of  $\zeta_0$  simply because  $\hat{n}_{ac}$  and  $\hat{k}_{ac}$  are not parallel to each other. In Fig. 18 we show polar plots of the dimensionless flux  $\langle \tilde{q}_x \rangle_\varphi$ , emitted by the shock as a function of the angle  $\theta'$  in the shock frame of reference. We consider a shock moving into air for different values of the incident Mach number. The plot has rotational symmetry around the  $\hat{x}$  axis. There are two pairs of symmetrical wings, which are separated by a zero flux value, achieved when  $\zeta_0 = \zeta_0^*$  given by Eq. (142). The first wing corresponds to the waves facing to the right as seen by an observer at rest in the compressed fluid. On the contrary, in the shock frame, all the sound energy escapes to the left. Similarly as we have done in the previous Subsection, we can integrate the expressions of the acoustic energy over  $\zeta_0$  to have the total average as a function of the shock strength for a given  $\gamma$ . Following Ribner [17], we define the dimensional acoustic strength emitted downstream, as an integral over the incidence angle  $\theta$ , in the interval corresponding to the short wavelengths of the upstream spectrum:  $0 \leq \theta \leq \theta_{cr}$ ,

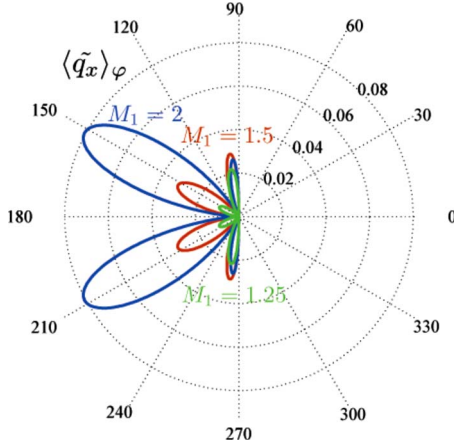


FIG. 18. (Color online) Polar plots of the dimensionless flux  $\langle \tilde{q}_x \rangle_\varphi$  as a function of the angle of emission  $\theta'$  in the frame comoving with the shock front. The shock moves into air ( $\gamma=7/5$ ) and the wings are shown for different shock strengths.

$$I_{ac} = \langle q_x \rangle_{\varphi, \theta} = \frac{\rho_2 c_2^3}{2} \int_0^{\theta_{cr}} e_s^2 (1 - M_2 \cos \theta_{ac}) (M_2 - \cos \theta_{ac}) \sin^3 \theta d\theta, \quad (150)$$

or as an integral over the dimensionless frequency  $\zeta_0$ , in the interval  $1 \leq \zeta_0 < \infty$ ,

$$I_{ac} = \langle q_x \rangle_{\varphi, \theta} = \frac{1}{2} \rho_1 (\delta v_1)^2 D \frac{16M_2^5 R^4 (M_1^2 - 1)^{5/2}}{(\gamma + 1)^2} \times \int_1^\infty \frac{\zeta_0 \sqrt{\zeta_0^2 - 1}}{[M_1^2 R + (M_1^2 - 1) \zeta_0^2]^{5/2} (\zeta_0 - M_2 \sqrt{\zeta_0^2 - 1})^2} \times \left[ \frac{(M_1^2 - 1) \zeta_0^2 - M_1^2}{M_1^2 - (M_1^2 + 1) \zeta_0^2 - 2M_1^2 M_2 \zeta_0 \sqrt{\zeta_0^2 - 1}} \right]^2 d\zeta_0. \quad (151)$$

With Ribner [17], we define a dimensional upstream turbulent energy flux as

$$I_{turb} = \frac{5}{6} \rho_1 (\delta v_1)^2 D. \quad (152)$$

We define the ratio between both fluxes, as a relative intensity,

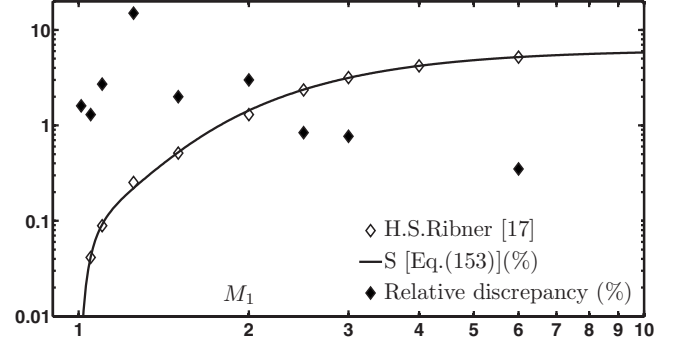


FIG. 19. Comparison between Eq. (153) and Ribner's results taken from [17] for shocks moving into air. We also show the relative discrepancy between both results.

$$S = \frac{I_{ac}}{I_{turb}}. \quad (153)$$

We plot the relative strength  $S$  in Fig. 19, for  $\gamma=7/5$ , as a function of  $M_1$ . Our results shown in Fig. 24 have been obtained using the exact analytical expressions for the sonic flux [Eq. (153)] given in [57], Appendix D. Their good agreement with the data from Table I of [17] confirms physical equivalence of our model and Ribner's. Figure 24 also shows the discrepancy between our and Ribner's results, which is very low for strong shocks,  $\sim 1-2\%$  for weak and moderate-strength shocks, and peaks at 15% for  $M_1=1.25$ . This discrepancy appears to be too high for a direct numerical integration of Eq. (151). Most likely it results from the evaluation of this integral in [17] using the interpolated [14] rather than the exact values of the integrand. As we have done before with the kinetic-energy amplification, it is interesting to analyze the behavior of  $S$  in the plane  $(\gamma, M_1)$ . To this scope, we plot  $S$  as a function of  $\gamma$  and  $M_1$  in Fig. 20.

In [57] Table II to be found in the Appendix F, we show numerical values of the relative sonic intensity emitted by the distorted shock as a function of the shock strength for three different gases. It is also worth to take advantage of the analytical expressions obtained for the acoustic flux, and examine its behavior in different physical limits. In fact, the limits of strong/weak shocks and highly compressible gases can be obtained either expanding the integral that leads to Eq. (153) or expanding the formulas shown in [57], Appendix D. In the limit of very strong shocks, the relative flux becomes a function of  $\gamma$ . We show its analytical expression,

$$S(\gamma, M_1 \gg 1) \cong \frac{(\gamma^2 - 1)(9 - 100\gamma + 187\gamma^2 + 8\gamma^3 - 240\gamma^4 + 120\gamma^5)}{20\gamma(2\gamma - 1)^2} - \frac{\sqrt{2(\gamma - 1)(\gamma + 1)}(-1 + 8\gamma - 43\gamma^2 + 57\gamma^3 + 22\gamma^4 - 75\gamma^5 + 30\gamma^6)}{5\gamma^{3/2}(2\gamma - 1)^2} - \frac{3(\gamma - 1)(\gamma + 1)^2(3 + 4\gamma - 13\gamma^2 + 10\gamma^3)}{20\gamma^{3/2}(2\gamma - 1)^3} \times \tan^{-1}\left(\frac{1}{\sqrt{\gamma}}\right) - \frac{3\sqrt{2}(\gamma + 1)^2(\gamma - 1)^{5/2}(-1 - 3\gamma + 2\gamma^2)(2 - 5\gamma + 5\gamma^2)}{5\sqrt{\gamma}(2\gamma - 1)^3} \ln\left[\frac{\gamma(\gamma - 1) + \sqrt{2\gamma(\gamma - 1)}}{\gamma(\gamma + 1)}\right]. \quad (154)$$

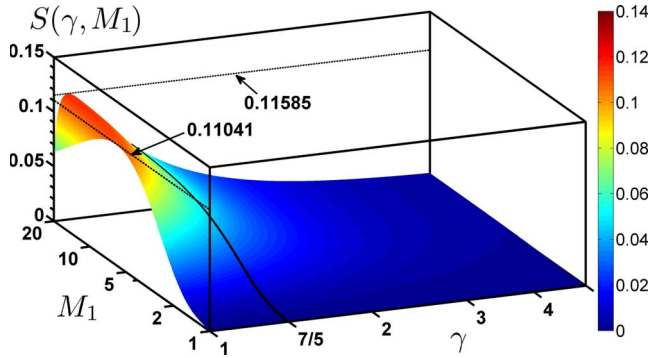


FIG. 20. (Color online) Relative acoustic flux as a function of  $\gamma$  and  $M_1$  [Eqs. (150)–(153)].

A plot of the above formula is shown in Fig. 21 together with the relative flux as a function of  $\gamma$  for shocks of large but finite strengths. The strong-shock limiting curve has a maximum at  $\gamma_{\max} \cong 1.06488$ , to which corresponds a relative

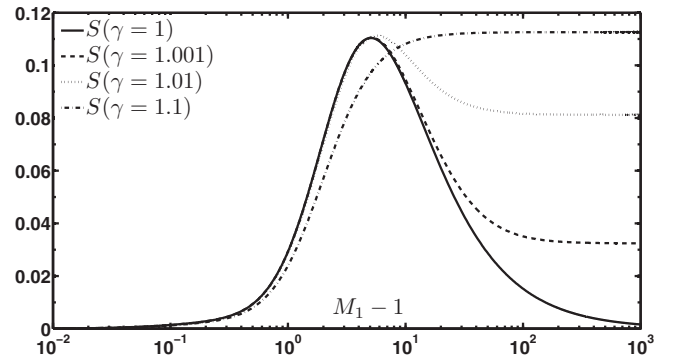


FIG. 22. Relative acoustic flux as a function of  $M_1$  for different values of  $\gamma$  in the highly compressible limit.

flux:  $S_{\max} \cong 0.11585$ . We can also there derive the analytical expressions for very compressible gases, in the limit  $\gamma \rightarrow 1$ , in which case the relative flux becomes a function of  $M_1$ . Its expression is

$$\begin{aligned}
 S(\gamma = 1, M_1) \cong & \frac{4}{5(M_1 - 1)(M_1^2 + 1)^5(M_1^4 + M_1^2 - 1)} (-4 + 4M_1 + 50M_1^2 - 86M_1^3 + 2M_1^4 + 72M_1^5 - 114M_1^6 + 116M_1^7 - 45M_1^8 - 3M_1^9 \\
 & + 34M_1^{10} - 26M_1^{11} + 19M_1^{12} - 6M_1^{13} + 2M_1^{14}) + \frac{4(-4 + 50M_1^2 - 54M_1^4 - 29M_1^6 + 19M_1^8 + 3M_1^{10})}{5(M_1^2 + 1)^5 \sqrt{(M_1^2 - 1)(M_1^4 + M_1^2 - 1)}} \\
 & - \frac{12M_1^6(-2 + 8M_1^2 - 2M_1^4 + M_1^6)}{5(M_1^4 - 1)^{3/2}(M_1^2 + 1)^4} \left[ \tan^{-1}(\sqrt{M_1^4 - 1}) + \tan^{-1}\left(\frac{\sqrt{M_1^4 - 1}}{M_1}\right) - \tan^{-1}\left(\frac{(M_1^2 - 1)\sqrt{M_1^2 + 1}}{\sqrt{M_1^4 + M_1^2 - 1}}\right) \right] \\
 & + \frac{48M_1^2(-3 + M_1^2 + 3M_1^4)}{5(M_1^2 + 1)^{11/2}} \ln \left[ \frac{(\sqrt{M_1^4 + M_1^2 - 1} + \sqrt{M_1^4 - 1})(1 + M_1\sqrt{M_1^2 + 1})}{(1 + \sqrt{M_1^2 + 1})\sqrt{M_1^4 + M_1^2 - 1}} \right].
 \end{aligned} \tag{155}$$

In Fig. 22 we show the envelope that corresponds to the limit  $\gamma = 1$ , together with other curves for  $\gamma$  near unity. The highly compressible envelope curve reaches a maximum value  $S_{\max} \cong 0.11041$  for  $M_1 \cong 6.08755$ . Finally, we show the weak-shock asymptotics for the sonic flux  $S$ , always in the shock reference frame, valid for any  $\gamma$ ,

$$\begin{aligned}
 S(\gamma, M_1 - 1 \ll 1) \cong & \frac{32}{25(\gamma + 1)^2} \left[ \frac{19}{7}(M_1 - 1)^2 \right. \\
 & \left. - 8\sqrt{2}(M_1 - 1)^{5/2} \right] + O[(M_1 - 1)^3].
 \end{aligned} \tag{156}$$

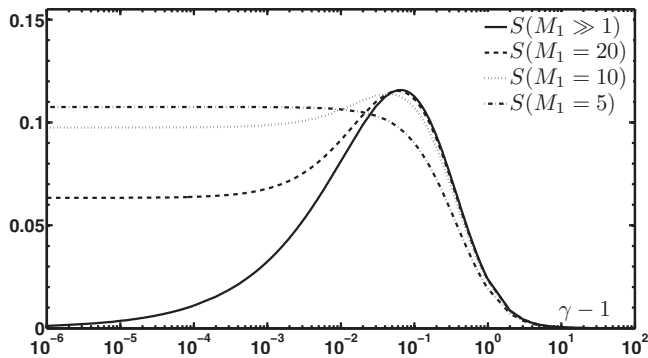


FIG. 21. Relative acoustic flux as a function of  $\gamma$  for  $M_1 \geq 1$  and different strong-shock strengths.

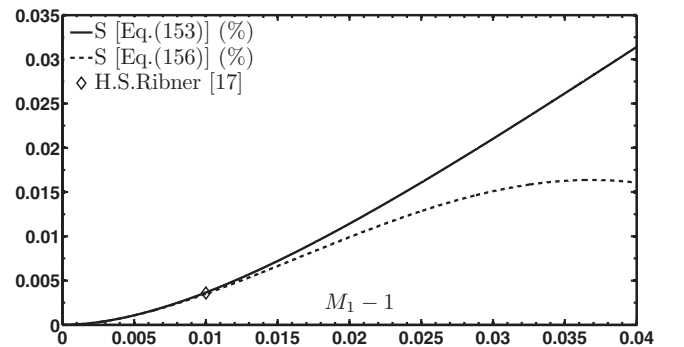


FIG. 23. Comparison between the exact solution Eq. (153) and the weak-shock limit approximation given by Eq. (156) for a shock moving into air ( $\gamma = 7/5$ ).

These are the first two terms of the weak-shock asymptotic formula that Lighthill [13] attempted to derive, and Ribner [17] later transformed into his Eq. (B10). The first term of expansion of Ribner's Eq. (B10) in powers of  $M_1 - 1 \ll 1$  is the same as in our Eq. (156). This confirms the accuracy of Lighthill's expression (as corrected by Ribner in [17]) for the energy scattered from the interaction of a small-amplitude sound wave with turbulence. The next term in this expansion,  $\sim (M_1 - 1)^{5/2}$ , represents the first correction to it due to small but finite strength of the shock wave. The numerical coefficient in this term in Ribner's Eq. (B10) is inaccurate (too small) by a factor of 32/15 compared to our Eq. (156). Due to this error, Ribner's estimate of  $S$  with the aid of the "converted Lighthill's" formula (B10) for  $M_1 = 1.01$  was off by 40% [17]. The correct weak-shock formula (156) is accurate within 4% for  $\gamma = 7/5$  and  $M_1 = 1.01$ . A comparison between Eqs. (153) and (156) is shown in Fig. 23 in the weak-shock limit, for a shock moving into air ( $\gamma = 7/5$ ). The Ribner's estimate at  $M_1 = 1.01$  is also shown.

### F. Downstream vorticity perturbations

In this subsection we compute the vorticity of the compressed fluid particles in the 3D problem. As discussed before, the downstream vorticity has two sources: one is the amplification of the upstream eddies, represented by the term proportional to  $\Omega_1$ , and the other source is the terms equal to  $\Omega_2 \tilde{p}_s$ , which is a consequence of the shock ripple oscillations. This second term is intrinsic to any RMI-like flow, whether the rippled shock moves into an homogeneous fluid or not, being proportional to the instantaneous shock front pressure perturbation [10,23,48,51,52]. At a first step, we calculate the components of the vorticity vector in the system of rotated axes  $\{x, y, z\}$  to later proceed with the 3D averaging. We note that we normalize the vorticity components with  $kc_2$ . The easiest to write is the component normal to the shock front, as it can be easily seen to be conserved across the shock surface:  $\omega_{2x} = \omega_{1x}$ . Besides, in the rotated axes there is no dependence on the  $z$  coordinate, a fact that allows us to get the value of  $\omega_{2y}$  very easily, from the divergence-free character of the vorticity vector,  $\vec{\nabla} \cdot \vec{\omega} = 0$ . In fact, we have

$$\begin{aligned} \tilde{\omega}_{1x} &= \tilde{v}_{1k} \sin \theta \cos \varphi, \\ \tilde{\omega}_{2y} &= -\frac{Rk_x}{k_y} \tilde{\omega}_{1x} = -\tilde{v}_{1k} R \cos \theta \cos \varphi. \end{aligned} \quad (157)$$

The remaining component  $\tilde{\omega}_{2z}$  is computed from the expressions given in Eq. (67), and taking into account that in passing from the 2D definition of  $\omega_z$  to the 3D problem, its amplitude is proportional to  $\sin^2 \theta$  because both  $k_y$  and  $u_1$  are proportional to  $\sin \theta$ . We can write

$$\begin{aligned} \tilde{\omega}_{2z}^2 &= \tilde{v}_{1k}^2 \sin^4 \theta \sin^2 \varphi \\ &\times \begin{cases} \Omega_1^2 + \Omega_2^2(e_{lr}^2 + e_{li}^2) + 2\Omega_1\Omega_2 e_{lr}, & \zeta_0 \leq 1 \\ \Omega_1^2 + \Omega_2^2 e_s^2 + 2\Omega_1\Omega_2 e_s, & \zeta_0 \geq 1, \end{cases} \end{aligned} \quad (158)$$

where the expressions for  $\Omega_{1,2}$  can be found in Eq. (65). The expressions for  $e_{lr}$ ,  $e_{li}$ , and  $e_s$  can be found in Eq. (47). As the normal component of the vorticity is unchanged through shock compression, we focus our attention on the component parallel to the shock front, given by:  $\omega_{\perp}^2 = \omega_{2y}^2 + \omega_{2z}^2$ , as done in [30]. To this purpose, we define

$$A_{\omega_{\perp}^2} = \frac{\langle \tilde{\omega}_{2y}^2 + \tilde{\omega}_{2z}^2 \rangle}{\langle \tilde{\omega}_{1y}^2 + \tilde{\omega}_{1z}^2 \rangle}, \quad (159)$$

as the amplification factor of the averaged squared vorticity, normal to the direction of shock motion. It is immediate to see, using Eqs. (108), (157), and (159) that

$$\begin{aligned} \langle \tilde{\omega}_{1y}^2 + \tilde{\omega}_{1z}^2 \rangle &= \frac{2}{3} \tilde{v}_{1k}^2, \\ \langle \tilde{\omega}_{2y}^2 + \tilde{\omega}_{2z}^2 \rangle &= \frac{R^2 \tilde{v}_{1k}^2}{6} + \langle \tilde{\omega}_{2z}^2 \rangle. \end{aligned} \quad (160)$$

We define:  $A_{\omega_z^2} = \langle \tilde{\omega}_{2z}^2 \rangle / \langle \tilde{\omega}_{1z}^2 \rangle$ , and using Eq. (157) again we can write

$$A_{\omega_{\perp}^2} = \frac{1}{4} R^2 + \frac{3}{4} A_{\omega_z^2}. \quad (161)$$

With the help of Eqs. (108) and (159), we can write

$$\begin{aligned} A_{\omega_z^2} &= \int_0^1 [\Omega_1^2 + \Omega_2^2(e_{lr}^2 + e_{li}^2) + 2\Omega_1\Omega_2 e_{lr}] \sin^5 \theta d\zeta_0 \\ &+ \int_1^{\infty} (\Omega_1^2 + \Omega_2^2 e_s^2 + 2\Omega_1\Omega_2 e_s) \sin^5 \theta d\zeta_0. \end{aligned} \quad (162)$$

It is not difficult to decompose the average in Eqs. (161) and (162) in the short and long-wavelength intervals. After some additional algebra we obtain

$$\begin{aligned} A_{\omega_{\perp}^2}^l &= \frac{R^2}{4} \cos^3 \theta_{cr} + \frac{3}{4} A_{\omega_z^2}^l, \\ A_{\omega_{\perp}^2}^s &= \frac{R^2}{4} (1 - \cos^3 \theta_{cr}) + \frac{3}{4} A_{\omega_z^2}^s, \end{aligned} \quad (163)$$

where  $A_{\omega_z^2}^{l,s}$  can be easily identified inside Eq. (162). Whether we integrate over the variable  $\zeta_0$  or over the incidence angle  $\theta$  is a matter of convenience. For numerical evaluation with commercial software, the above integrals over  $\zeta_0$  are easy to implement. However, in order to get analytical expressions, it is better to integrate over  $\theta$ , as has been done for the kinetic energy and the sonic flux before. The analytical expressions for  $A_{\omega_z^2}$  are shown in the auxiliary file attached to this work [57]. Besides, the vorticity amplification factors (long/short and total) for three gases, at different shock strengths are also shown in [57], Table III.

Expanding the analytical expressions found in the corresponding Appendix [57], we write the limit of very strong incident shocks. In this case, the amplification factor is only a function of the  $\gamma$  exponent. We show the contribution in that limit for the long and short-wavelength intervals, as well as their sum in Eq. (166) below,

$$A_{\omega_{\perp}}^l(\gamma, M_1 \gg 1) \cong \frac{240\gamma^6 + 120\gamma^5 - 725\gamma^4 - 630\gamma^3 + 104\gamma^2 + 6\gamma + 5}{40\gamma(\gamma+1)^2\sqrt{2\gamma(\gamma-1)}} - \frac{3\gamma(\gamma-2)(\gamma+1)(2\gamma-1)}{2\sqrt{2\gamma(\gamma-1)}} \ln\left(\frac{\gamma+1}{\gamma-1}\right), \quad (164)$$

$$A_{\omega_{\perp}}^s(\gamma, M_1 \gg 1) \cong \frac{1}{5(\gamma^2-1)^2}(105\gamma^8 - 210\gamma^7 - 275\gamma^6 + 575\gamma^5 + 224\gamma^4 - 480\gamma^3 - 27\gamma^2 + 115\gamma + 5) \\ - \frac{1}{40\gamma(\gamma-1)(\gamma+1)^2\sqrt{2\gamma(\gamma-1)}}(1680\gamma^9 - 2520\gamma^8 - 5800\gamma^7 + 6440\gamma^6 + 7051\gamma^5 - 4617\gamma^4 - 3002\gamma^3 \\ + 446\gamma^2 + 71\gamma - 5) - \frac{3\gamma(\gamma-2)(\gamma+1)(7\gamma^3 - 14\gamma^2 + 5\gamma + 1)}{\sqrt{2\gamma(\gamma-1)}} \ln\left[\frac{\gamma(\gamma-1) + \sqrt{2\gamma(\gamma-1)}}{\gamma(\gamma+1)}\right], \quad (165)$$

$$A_{\omega_{\perp}}^2(\gamma, M_1 \gg 1) \cong \frac{105\gamma^8 - 210\gamma^7 - 275\gamma^6 + 575\gamma^5 + 224\gamma^4 - 480\gamma^3 - 27\gamma^2 + 115\gamma + 5}{5(\gamma^2-1)^2} \\ - \frac{210\gamma^7 - 525\gamma^6 - 230\gamma^5 + 1050\gamma^4 - 63\gamma^3 - 526\gamma^2 + 59\gamma + 9}{5(\gamma^2-1)\sqrt{2\gamma(\gamma-1)}} - \frac{3\gamma(\gamma-2)(\gamma+1)(2\gamma-1)}{2\sqrt{2\gamma(\gamma-1)}} \ln\left(\frac{\gamma+1}{\gamma-1}\right) \\ - \frac{3\gamma(\gamma-2)(\gamma+1)(7\gamma^3 - 14\gamma^2 + 5\gamma + 1)}{\sqrt{2\gamma(\gamma-1)}} \ln\left[\frac{\gamma(\gamma-1) + \sqrt{2\gamma(\gamma-1)}}{\gamma(\gamma+1)}\right]. \quad (166)$$

Equation (166) scales in the strong compressible gas limit ( $\gamma \rightarrow 1$ ), as

$$A_{\omega_{\perp}}^2(\gamma-1 \ll 1, M_1 \gg 1) \cong \frac{8}{5(\gamma-1)^2} + O\left[\frac{1}{(\gamma-1)^{3/2}}\right], \quad (167)$$

and for very strong shocks and highly incompressible fluids, as

$$A_{\omega_{\perp}}^2(\gamma \gg 1, M_1 \gg 1) \cong 1 + \frac{4}{\gamma} + \frac{28-5\sqrt{2}}{5\gamma^2} + O\left(\frac{1}{\gamma^3}\right). \quad (168)$$

We show the total contribution to the vorticity amplification in the strong-shock limit, as a function of  $\gamma$  in Fig. 24, where the solid line corresponds to Eq. (166).

As is clear from Fig. 24, the vorticity amplification increases as  $\gamma \rightarrow 1$  and  $M_1$  increases. In fact, as the gas becomes infinitely compressible, the factor  $R^2$  that enters in the amplification factor of the upstream transverse vorticity component (given by the term  $\Omega_1 = R/\sin^2 \theta$ ) will diverge as  $1/(\gamma-1)^2$ . The reason for the divergence of the vorticity lies in the fact that the longitudinal characteristic length decreases to zero in that limit. However, the kinetic-energy content remains finite, as has been shown in the previous subsection. It is clear that a divergence of the vorticity amplification in the highly compressible limit is not physical. As  $\gamma$  approaches unity and the shock becomes stronger, the spatial gradients of the velocity components in the fluid

downstream increase almost without bound, due to the violent length scale reduction. Hence, the viscous stresses in the equations of motion become as important as the components of the pressure gradient, and the inviscid fluid approximation breaks down, invalidating the solution obtained in this work. The more realistic approach of considering the evolution of random downstream perturbations for a gas with non negligible viscosity has yet to be carried out. The influence of viscosity on shock ripple evolution and the magnitudes downstream has been treated in [34] for a single wavelength 2D shock corrugation, and its extension to the interaction with a turbulent spectrum is left for future work.

We show the highly compressible limit, which is obtained by making  $\gamma \rightarrow 1$ , at finite  $M_1$ , and we get

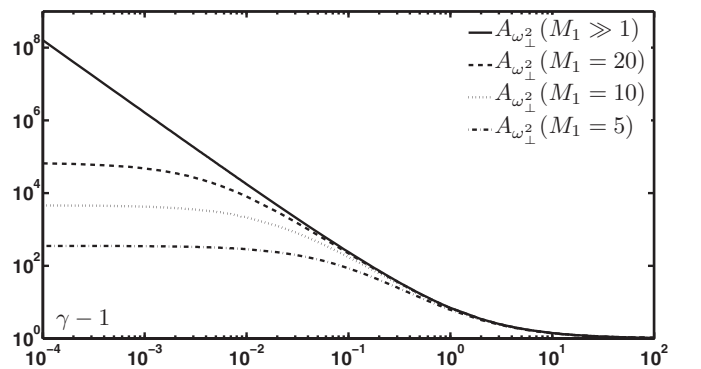


FIG. 24. Strong-shock ( $M_1 \gg 1$ ) asymptotic of the transverse vorticity amplification factor [Eq. (166)], together with other finite values of  $M_1$ .

$$A_{\omega_{\perp}}^l(\gamma=1, M_1) \cong \frac{\sqrt{M_1^2-1}}{20M_1^4(M_1^2+1)^2(M_1^4+M_1^2-1)^{5/2}}(55M_1^{18}-53M_1^{16}-333M_1^{14}+68M_1^{12}+388M_1^{10}-105M_1^8 - 112M_1^6+8M_1^4+32M_1^2-8) + \frac{3M_1^4(M_1^2-1)}{(M_1^2+1)^{5/2}} \ln\left(\frac{\sqrt{M_1^4+M_1^2-1}+\sqrt{M_1^2-1}}{M_1}\right), \quad (169)$$

$$A_{\omega_{\perp}}^s(\gamma=1, M_1) \cong \frac{1}{5M_1^4(M_1^2+1)^4(M_1^4+M_1^2-1)^2}(2M_1^{24}+2M_1^{23}+20M_1^{22}+14M_1^{21}+18M_1^{20}+109M_1^{19}-72M_1^{18} - 13M_1^{17}+181M_1^{16}-424M_1^{15}+416M_1^{14}+179M_1^{13}-532M_1^{12}+433M_1^{11}-366M_1^{10}-390M_1^9+586M_1^8 + 90M_1^7-168M_1^6-7M_1^4+2) - \frac{\sqrt{M_1^2-1}}{20M_1^4(M_1^2+1)^4(M_1^4+M_1^2-1)^{5/2}}(125M_1^{22}+43M_1^{20}-772M_1^{18} + 707M_1^{16}+2473M_1^{14}-2299M_1^{12}-1870M_1^{10}+2533M_1^8-676M_1^6-32M_1^4+8) + \frac{3M_1^2(M_1^2-1)(M_1^2+3)(M_1^4-4M_1^2+2)}{(M_1^2+1)^{9/2}} \ln\left[\frac{(\sqrt{M_1^4+M_1^2-1}+\sqrt{M_1^4-1})(1+M_1\sqrt{M_1^2+1})}{(1+\sqrt{M_1^2+1})\sqrt{M_1^4+M_1^2-1}}\right], \quad (170)$$

$$A_{\omega_{\perp}}^2(\gamma=1, M_1) \cong \frac{1}{5M_1^4(M_1^2+1)^4(M_1^4+M_1^2-1)^2}(2M_1^{24}+2M_1^{23}+20M_1^{22}+14M_1^{21}+18M_1^{20}+109M_1^{19}-72M_1^{18}-13M_1^{17} + 181M_1^{16}-424M_1^{15}+416M_1^{14}+179M_1^{13}-532M_1^{12}+433M_1^{11}-366M_1^{10}-390M_1^9+586M_1^8+90M_1^7-168M_1^6 - 7M_1^4+2) - \frac{(M_1^2-1)^{5/2}}{5M_1^2(M_1^2+1)^4(M_1^4+M_1^2-1)^{3/2}}(45M_1^{12}+70M_1^{10}-129M_1^8-110M_1^6+133M_1^4-20M_1^2-4) + \frac{3M_1^2(M_1^2-1)(M_1^2+3)(M_1^4-4M_1^2+2)}{(M_1^2+1)^{9/2}} \ln\left[\frac{(\sqrt{M_1^4+M_1^2-1}+\sqrt{M_1^4-1})(1+M_1\sqrt{M_1^2+1})}{(1+\sqrt{M_1^2+1})\sqrt{M_1^4+M_1^2-1}}\right] + \frac{3M_1^4(M_1^2-1)}{(M_1^2+1)^{5/2}} \ln\left(\frac{\sqrt{M_1^4-1}+\sqrt{M_1^4+M_1^2-1}}{M_1}\right). \quad (171)$$

The asymptotic expansion of the last formula in the weak-shock limit is

$$A_{\omega_{\perp}}^2(\gamma=1, M_1-1 \ll 1) \cong 1+4(M_1-1)+O[(M_1-1)^2], \quad (172)$$

where the linear term comes from  $\Omega_1$ , and is due to the amplification of the upstream vorticity by the factor  $R$ .

The total amplification of the transverse vorticity for highly compressible fluids is shown in Fig. 25, where the solid line corresponds to Eq. (171). The limiting curve for  $\gamma=1$  is shown together with curves for near  $\gamma$  values. At any  $\gamma>1$ , the amplification saturates at the value given by Eq. (166), but for  $\gamma=1$  it grows without limit like

$$A_{\omega_{\perp}}^2(\gamma=1, M_1 \gg 1) \cong \frac{2M_1^4}{5} + \frac{2M_1^3}{5} + O(M_1^2). \quad (173)$$

In Fig. 26 we show a 2D map of  $A_{\omega_{\perp}}^2$  as function of  $\gamma$  and  $M_1$ . We see that the vorticity grows unbounded in the limits of very strong shock and highly compressible gases in agreement with the previous equations and the graphs shown in Fig. 24 and 25. The black curve corresponds to a shock moving into air ( $\gamma=7/5$ ).

The weak-shock limit for arbitrary values of  $\gamma$  is given by

$$A_{\omega_{\perp}}^2(\gamma, M_1-1 \ll 1) \cong 1 + \frac{8}{\gamma+1}(M_1-1) + O[(M_1-1)^2]. \quad (174)$$

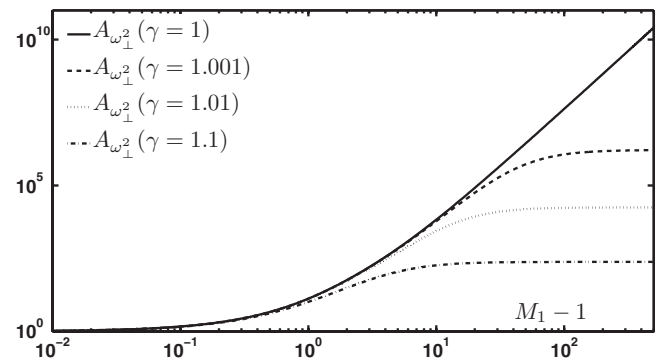


FIG. 25. Highly compressible asymptotic ( $\gamma=1$ ) of the transverse vorticity amplification factor [Eq. (171)], together with the amplification factor for other values of  $\gamma$  near unity.

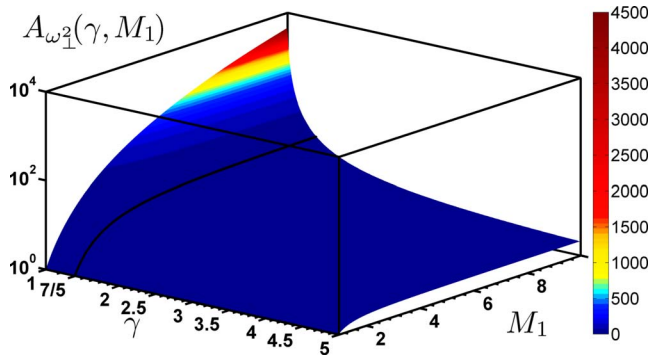


FIG. 26. (Color online) 2D map of the amplification factor for the transverse component of the vorticity ( $\delta\omega_{\perp}^2 = \delta\omega_y^2 + \delta\omega_z^2$ ) as a function of the shock strength and gas compressibility. The black curve corresponds to a shock moving into air ( $\gamma=7/5$ ).

### G. Anisotropy of the downstream perturbations

One of the questions that we may try to answer using the model presented here regards the isotropy of the compressed turbulent field. Being that there is a privileged direction in space, given by the direction of the shock motion, it seems natural to think that this fact may modify the isotropy of the upstream perturbations to some degree, which could be worth quantifying. Different choices of the “anisotropy parameter” have been used in the existing literature [14–17,40], which are actually *ad hoc* definitions aimed to characterize the level of anisotropy of the perturbations downstream. We define, with the same liberty, the following parameter:

$$\beta_v = \frac{\langle \bar{v}_{\perp}^2 \rangle - 2\langle \bar{v}_{\parallel}^2 \rangle}{\langle \bar{v}_{\perp}^2 \rangle + 2\langle \bar{v}_{\parallel}^2 \rangle} = 1 - 4 \frac{\langle \bar{v}_x^2 \rangle}{\langle \bar{v}^2 \rangle + \langle \bar{v}_x^2 \rangle}. \quad (175)$$

Here,  $v_{\perp}$  refers to the velocity component parallel to the shock surface and  $v_{\parallel}$  is actually equal to  $v_x$ . The anisotropy parameter varies between  $-1$  and  $1$ , and a zero value implies isotropy downstream. The upper limiting value of  $\beta_v=1$  is actually reached in the limit of strong shock and high compressibility,  $\gamma \rightarrow 1$  and  $M_1 \rightarrow \infty$ , where we know that the longitudinal motion of the compressed particles is suppressed. In this limit, the velocity vectors of the compressed fluid elements would be inclined toward the shock surface. In Fig. 27 we show the parameter  $\beta_v$  as a function of  $\gamma$  and  $M_1$ . We see that there are no situations for which this parameter might reach the limit  $\beta_v=-1$ , which would correspond to a completely longitudinal velocity field. This is quite natural, as we know that  $1/2$  of the kinetic energy (with components parallel to the shock surface) passes unchanged for any value of  $\gamma$  and any shock strength. In between both limits, we have the possibility of making  $\beta_v=0$ , corresponding to isotropic velocity perturbations downstream. This condition defines an isotropy curve (besides the trivial curve that is drawn at  $M_1=1$ ), which is shown in Fig. 28. Interestingly, we note the existence of an asymptote of this curve for very strong shocks, which defines a critical value  $\gamma^*=2.3646$ . For fluids with  $\gamma > \gamma^*$ , there is no shock wave that leaves the velocity perturbations isotropic during compression. If the gas under study is air, we would instead find regions of lateral and

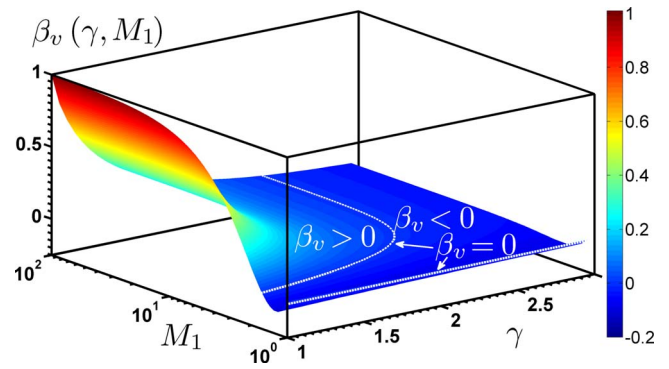


FIG. 27. (Color online) Downstream velocity anisotropy parameter [Eq. (175)] as a function of  $\gamma$  and  $M_1$ .

longitudinal anisotropy. As can be seen, for a shock moving into air with  $M_1 \cong 1.9332$ , the isotropy of the velocity perturbations will not be altered. Having defined an anisotropy parameter for the velocity field, it is straightforward to do similarly with the vorticity perturbations. We have already seen in Eqs. (98) and (99) that isotropy of the upstream velocities implies isotropy of the vorticity perturbations. As the shock may substantially change the isotropy of the velocity field, it is natural to ask whether the vorticity field isotropy is modified to a similar extent. Similarly as in Eq. (175), we define a downstream vorticity anisotropy parameter,

$$\beta_{\omega} = \frac{\langle \bar{\omega}_{\perp}^2 \rangle - 2\langle \bar{\omega}_{\parallel}^2 \rangle}{\langle \bar{\omega}_{\perp}^2 \rangle + 2\langle \bar{\omega}_{\parallel}^2 \rangle} = \frac{A_{\omega_{\perp}^2} - 1}{A_{\omega_{\perp}^2} + 1}. \quad (176)$$

We know that  $A_{\omega_{\perp}^2} \rightarrow \infty$  in the limit of very strong shocks and highly compressible fluids ( $M_1 \gg 1, \gamma \rightarrow 1$ ), which makes  $\beta_{\omega} \cong 1$  in that limit. In fact, in that case, the vorticity is essentially parallel to the shock front, as discussed previously. Besides, we know that the transverse vorticity amplification factor is always greater than 1 for any values of  $\gamma$  and  $M_1$ . Hence, it will be always  $\beta_{\omega} > 0$ , which means that the vorticity downstream is always essentially laterally anisotropic. In Fig. 29 we can see the behavior of  $\beta_{\omega}$  on the  $(\gamma, M_1)$  plane.

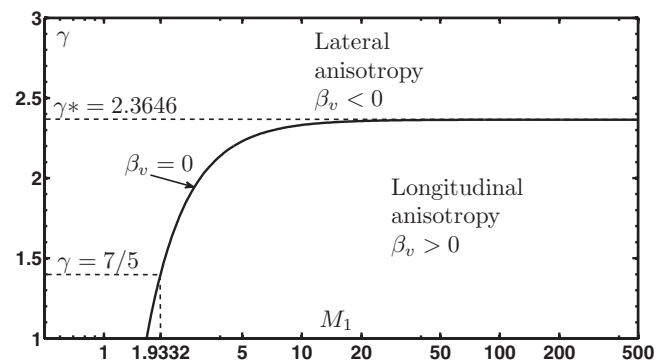


FIG. 28. Downstream velocity-isotropy curve, defined by the condition:  $\beta_v=0$ . We also show the regions of longitudinal and transverse anisotropy.

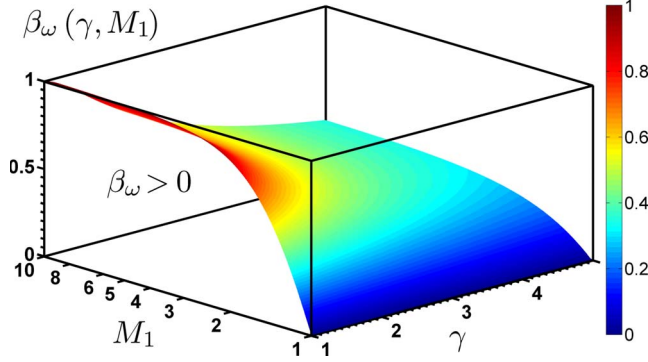


FIG. 29. (Color online) Downstream vorticity anisotropy parameter  $\beta_\omega$  [see Eq. (176)] for different values of  $\gamma$  and  $M_1$ .

### H. Interaction of a shock wave with a 2D turbulent velocity field: average kinetic energy of the downstream perturbations

Before finishing the work it is interesting to apply the formalism developed in the previous subsections to a simpler problem: a planar shock interacting with an isotropic turbulent field in 2D. Although this case may be considered non realistic, it is a convenient reference problem that might help with the understanding of numerical simulations [19]. Rotman studied this situation with the help of large scale eddy simulations (LES), in which he considered the interaction of a planar shock with two types of upstream inhomogeneities: vorticity and density. We concentrate here on the velocity fluctuations as the density case will be the subject of a future work. In our model, this 2D problem may be thought of as if the wave-number vector  $\vec{k}$  had only components  $k_x$  and  $k_y$  and simultaneously were  $\delta v_z = 0$ . This case is a particular subset of Eqs. (105)–(107) corresponding to the choice:  $\varphi = \pi/2$  and  $0 \leq \theta \leq \pi$ . This gives us a velocity field contained in the  $\{x, y\}$  plane and a vorticity vector only directed along the  $z$  axis. Assuming that the wave number  $\vec{k} \equiv (k_x, k_y)$  is uniformly distributed along the unit semicircle, it is easy to see that the probability of a particular orientation is just  $d\theta/\pi$ . Before proceeding, it is necessary to define the non dimensional velocities. For the downstream rotational perturbations, we define

$$\begin{aligned} \delta v_{2x}^{rot} &= c_2 u_1 \tilde{v}_{2x}^{rot}, \\ \delta v_{2y}^{rot} &= c_2 u_1 \tilde{v}_{2y}^{rot} = c_2 u_1 R \frac{k_x}{k_y} \tilde{v}_{2x}^{rot}, \end{aligned} \quad (177)$$

and for the sound waves

$$\begin{aligned} \delta v_{2x}^{ac} &= c_2 u_1 \tilde{v}_{2x}^{ac}, \\ \delta v_{2y}^{ac} &= c_2 u_1 \tilde{v}_{2y}^{ac}. \end{aligned} \quad (178)$$

In general, the amplitudes of the transformed velocities and of the sound wave pressure perturbations downstream will be complex numbers with real and imaginary parts because the input to the shock equations is chosen as a complex exponential as in the 3D problem. However, it is not difficult to realize that the absolute value of the complex amplitudes are

the same as the absolute values of the 2D downstream velocities obtained in Sec. II. We note that the small dimensionless amplitude is  $u_1 = \tilde{v}_{1k} \sin \theta$ , after using Eq. (105) with  $\varphi = \pi/2$ . We can therefore write, for the rotational part,

$$\begin{aligned} |\tilde{v}_{2x}^{rot}| &= |Q_{rot}(\gamma, M_1, \zeta_0)| \tilde{v}_{1k} \sin \theta, \\ |\tilde{v}_{2y}^{rot}| &= R \frac{k_x}{k_y} |Q_{rot}(\gamma, M_1, \zeta_0)| \tilde{v}_{1k} \sin \theta, \end{aligned} \quad (179)$$

The function  $Q_{rot}$  is defined with the aid of Eqs. (79) and (81). Similarly, we have for the sound waves emitted downstream,

$$\begin{aligned} |\tilde{v}_{2x}^{ac}| &= |Q_{ac}(\gamma, M_1, \zeta_0)| \tilde{v}_{1k} \sin \theta, \\ |\tilde{v}_{2y}^{ac}| &= \frac{|Q_{ac}(\gamma, M_1, \zeta_0)|}{\sqrt{\zeta_1^2 - 1}} \tilde{v}_{1k} \sin \theta, \\ \tilde{v}_{2z}^{ac} &= 0, \end{aligned} \quad (180)$$

where  $\zeta_1$  and  $Q_{ac}$  have been defined in Eqs. (54) and (60), respectively. The rotational kinetic energy of the compressed fluid particles (per unit mass) is

$$\begin{aligned} \tilde{T}_{2D}^{rot} &= \frac{1}{2} [(\tilde{v}_{2x}^{rot})^2 + (\tilde{v}_{2y}^{rot})^2], \\ &= \frac{\tilde{v}_{1k}^2}{2} \left\{ \left[ 1 + \left( R \frac{k_x}{k_y} \right)^2 \right] |Q_{rot}|^2 \sin^2 \theta \right\}, \end{aligned} \quad (181)$$

and the sound waves' contribution is

$$\begin{aligned} \tilde{T}_{2D}^{ac} &= \frac{1}{2} [(\tilde{v}_{2x}^{ac})^2 + (\tilde{v}_{2y}^{ac})^2], \\ &= \frac{\tilde{v}_{1k}^2 \zeta_1^2 Q_{ac}^2}{2 \zeta_1^2 - 1} \sin^2 \theta. \end{aligned} \quad (182)$$

It is noted that the functions defined above can be thought either as functions of  $\theta$  or  $\zeta_0$ , through the relationship that couples  $\zeta_0$  and  $\theta$  given by Eq. (109). The amplification coefficient is defined as the ratio between the averaged downstream kinetic energy and the preshock average kinetic energy per fluid particle,

$$A_{2D} = \frac{4}{\pi \tilde{v}_{1k}^2} \int_0^{\pi/2} (\tilde{T}_{2D}^{rot} + \tilde{T}_{2D}^{ac}) d\theta, \quad (183)$$

where we have used the fact that the intervals  $0 \leq \theta \leq \pi/2$  and  $\pi/2 \leq \theta \leq \pi$  are physically equivalent for the calculation of the kinetic energy. The last integral is better decomposed as

$$A_{2D} = A_{2D}^l + A_{2D}^s + A_{2D}^{ac}, \quad (184)$$

where, expressing each term as integrals over  $\zeta_0$ , we can write

$$A_{2D}^l = \frac{4}{\pi \tilde{v}_{1k}^2} \int_0^1 \frac{\tilde{T}_{2D}^{rot} M_1^3 R^{3/2} \sqrt{M_1^2 - 1}}{[R M_1^2 + (M_1^2 - 1) \zeta_0^2]^2} d\zeta_0,$$

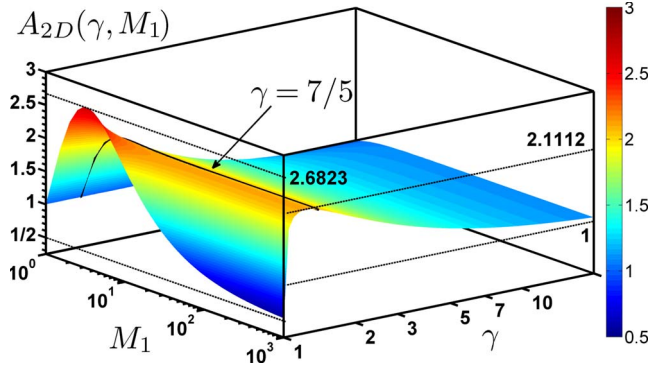


FIG. 30. (Color online) Kinetic-energy amplification factor for a shock interacting with a random 2D vorticity field, as a function of  $\gamma$  and  $M_1$  [Eq. (184)].

$$A_{2D}^s = \frac{4}{\pi \tilde{v}_{1k}^2} \int_1^\infty \frac{\tilde{T}_{2D}^{rot} M_1^3 R^{3/2} \sqrt{M_1^2 - 1}}{[RM_1^2 + (M_1^2 - 1)\zeta_0^2]^2} d\zeta_0,$$

$$A_{2D}^{ac} = \frac{4}{\pi \tilde{v}_{1k}^2} \int_1^\infty \frac{\tilde{T}_{2D}^{ac} M_1^3 R^{3/2} \sqrt{M_1^2 - 1}}{[RM_1^2 + (M_1^2 - 1)\zeta_0^2]^2} d\zeta_0. \quad (185)$$

in which  $A_{2D}^l$  stands for the integral of the rotational velocities over the long-wavelength interval  $0 \leq \zeta_0 \leq 1$ ,  $A_{2D}^s$  stands for the rotational integral over the short-wavelength interval  $1 \leq \zeta_0 < \infty$ , and  $A_{2D}^{ac}$  refers to the integral of the sonic contribution in the interval  $1 \leq \zeta_0 < \infty$ . It is clear that  $A_{2D}$  will be only a function of  $\gamma$  and  $M_1$ . The integrals corresponding to Eq. (185) does not pose difficulties for its numerical evaluation for arbitrary values of the governing parameters  $\gamma$  and  $M_1$ . We show a two-dimensional map of  $A_{2D}$  in the plane  $(\gamma, M_1)$  for the ranges  $1 \leq \gamma \leq 20$  and  $1 \leq M_1 \leq 1000$  in Fig. 30.

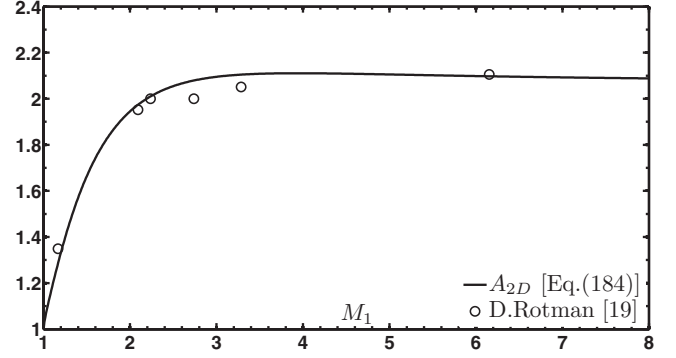


FIG. 31. 2D kinetic-energy amplification factor for a shock moving into air ( $\gamma=7/5$ ), as a function of  $M_1$ . Also shown are the LES results from [19].

Numerical values of the 2D kinetic-energy amplification factors (long/short wavelengths, acoustic contribution and total) are shown for three different gases, at different shock Mach numbers in the attached file to this work in [57], Table IV.

In Fig. 31 the amplification factor for a shock moving into air as a function of  $M_1$  is shown. We compare with the results obtained in [19] for this case. We see a very good agreement between the prediction of our model and the results of the LES shown in that reference for a weakly turbulent vorticity field ahead of the shock. The amplification factor can be integrated analytically in different important limits which we show below. We separate the contributions from the long/short-wavelength intervals and the contribution from the acoustic field.

Contribution to the amplification of the kinetic energy due to the vorticity produced by shock interaction with the long-wavelength preshock perturbation modes ( $0 < \zeta_0 < 1$ ) is

$$A_{2D}^l(\gamma, M_1 \gg 1) \cong -\frac{2\sqrt{\gamma-1}}{\pi(\gamma+1)^{3/2}} + \frac{(4\gamma^3 + \gamma^2 - 4\gamma + 1)}{\pi(\gamma+1)^2} \tan^{-1}(\sqrt{\gamma^2-1}) + \frac{4}{\pi} \sqrt{\frac{\gamma(\gamma-1)(2-\gamma)}{\gamma+1}} \ln \left[ \frac{1 + \sqrt{\gamma(2-\gamma)}}{\gamma-1} \right], \quad (186)$$

and the short-wavelength interval ( $1 < \zeta_0 < \infty$ ) gives

$$A_{2D}^s(\gamma, M_1 \gg 1) \cong \frac{4(\gamma^2-1)}{(2\gamma-1)^2} + \frac{2(8\gamma^3-6\gamma^2-10\gamma+1)\sqrt{\gamma-1}}{\pi(2\gamma-1)(\gamma+1)^{3/2}} - 2(4\gamma^3-9\gamma^2+3\gamma+1) \sqrt{\frac{\gamma-1}{\gamma+1}} \\ + \frac{2(32\gamma^7-72\gamma^6-16\gamma^5+104\gamma^4-40\gamma^3-23\gamma^2+16\gamma+1)}{\pi(2\gamma-1)^2(\gamma+1)^2} \tan^{-1} \left( \sqrt{\frac{\gamma+1}{\gamma-1}} \right) \\ - \frac{4(8\gamma^4-18\gamma^3+12\gamma^2-2\gamma-1)}{\pi(2\gamma-1)^2} \sqrt{\frac{\gamma(\gamma-1)(2-\gamma)}{\gamma+1}} \ln \left[ \frac{1 + \sqrt{\gamma(2-\gamma)}}{\gamma-1} \right]. \quad (187)$$

The acoustic contribution is

$$\begin{aligned}
 A_{2D}^{ac}(\gamma, M_1 \gg 1) \cong & -\frac{4}{\pi}(4\gamma^2 - 3)\left(\frac{\gamma-1}{\gamma+1}\right)^{3/2} + \frac{4\gamma(2\gamma-1)(2\gamma-3)(\gamma-1)^{3/2}}{\sqrt{\gamma+1}} \\
 & - \frac{8(\gamma-1)(4\gamma^5 - 4\gamma^4 - 7\gamma^3 + 5\gamma^2 + 2\gamma - 1)}{\pi(\gamma+1)^2} \tan^{-1}\left(\sqrt{\frac{\gamma+1}{\gamma-1}}\right) \\
 & - \frac{4}{\pi}(4\gamma^2 - 8\gamma + 1)(\gamma-1)^{5/2} \sqrt{\frac{\gamma}{(\gamma+1)(2-\gamma)}} \ln\left[\frac{1 + \sqrt{\gamma(2-\gamma)}}{\gamma-1}\right]. \quad (188)
 \end{aligned}$$

Collecting similar terms, and after some algebra, we present the final strong-shock limit asymptotic formula for the 2D turbulent kinetic-energy amplification coefficient,

$$\begin{aligned}
 A_{2D}(\gamma, M_1 \gg 1) \cong & \frac{16\gamma^5 - 8\gamma^4 - 8\gamma^3 + 21\gamma^2 - 16\gamma - 3}{(2\gamma-1)^2(\gamma+1)^2} - \frac{4(8\gamma^4 - 16\gamma^3 + \gamma^2 + 15\gamma - 4)\sqrt{\gamma-1}}{\pi(2\gamma-1)(\gamma+1)^{3/2}} + 2(8\gamma^4 - 28\gamma^3 + 31\gamma^2 - 9\gamma - 1) \\
 & \times \sqrt{\frac{\gamma-1}{\gamma+1}} - \frac{8(\gamma-1)}{\pi(2\gamma-1)^2(\gamma+1)^2} (16\gamma^7 - 40\gamma^6 + 2\gamma^5 + 62\gamma^4 - 30\gamma^3 - 12\gamma^2 + 12\gamma - 1) \tan^{-1}\left(\sqrt{\frac{\gamma+1}{\gamma-1}}\right) \\
 & - \frac{4(16\gamma^6 - 88\gamma^5 + 186\gamma^4 - 184\gamma^3 + 79\gamma^2 - 8\gamma - 3)}{\pi(2\gamma-1)^2} \sqrt{\frac{\gamma(\gamma-1)}{(\gamma+1)(2-\gamma)}} \ln\left[\frac{1 + \sqrt{\gamma(2-\gamma)}}{\gamma-1}\right]. \quad (189)
 \end{aligned}$$

In Fig. 32 we plot the total strong-shock amplification factor [Eq. (189)] as a function of  $\gamma$  together with the exact value for other very strong, but finite strength, shocks. In the 2D situation, the amplification factor reaches its maximum, equal to 2.111 16, at  $\gamma \cong 1.2298$ . Furthermore, for very low compressibility ( $\gamma \rightarrow \infty$ ), the amplification coefficient tends to unity, as it should,

$$A_{2D}(\gamma \gg 1, M_1 \gg 1) \cong 1 + \frac{2}{\gamma} - \frac{4}{3\pi\gamma^2} + O\left(\frac{1}{\gamma^3}\right). \quad (190)$$

In the opposite limit of very high compressibility ( $\gamma-1 \ll 1$ ), the amplification factor passes through unity at  $\gamma \cong 1.00161$ , and tends asymptotically to 1/2,

$$\begin{aligned}
 A_{2D}(\gamma-1 \ll 1, M_1 \gg 1) \cong & \frac{1}{2} + \frac{1}{\pi} \left[ 4 \ln\left(\frac{2}{\gamma-1}\right) + \pi - 4 \right] \\
 & \times \sqrt{2(\gamma-1)} + O(\gamma-1). \quad (191)
 \end{aligned}$$

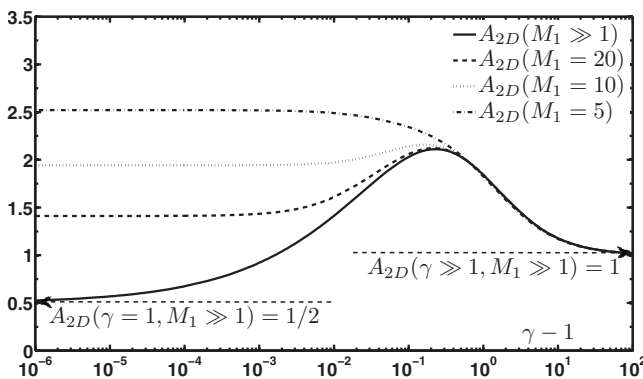


FIG. 32. Strong-shock limit ( $M_1 \gg 1$ ) of the 2D kinetic-energy amplification factor [Eq. (189)], together with other curves for large but finite shock Mach numbers.

The physical reason for this limit can be easily understood, as in the 3D problem. A very strong shock in the limit  $\gamma \rightarrow 1$  suppresses any longitudinal motion in the  $x$  direction, leaving the lateral velocity unchanged (this can be confirmed by looking at the expressions for  $\tilde{v}_x$  downstream and for the shock ripple amplitude  $\xi_s$ ). Hence, only 1/2 of the total kinetic energy per unit mass passes unchanged across the shock. As has been discussed in the full 3D case, we have two sources of vorticity in this problem: an amplification of the upstream vorticity, represented by the term  $\Omega_1$  in Eq. (64), and an intrinsic vorticity generated by the shock ripple oscillation, given by the term proportional to  $\Omega_2$  in that same equation. In fact, both terms are out of phase in the 2D problem too. That is, the vorticity added by the shock corrugation interferes destructively with the amplified vorticity upstream. This interference is maximum in the limit of very strong shock and highly compressible fluid, giving rise to the observed reduction. We present the high compressibility limit ( $\gamma \rightarrow 1$ ) formulas as a function of  $M_1$ . The different contributions are

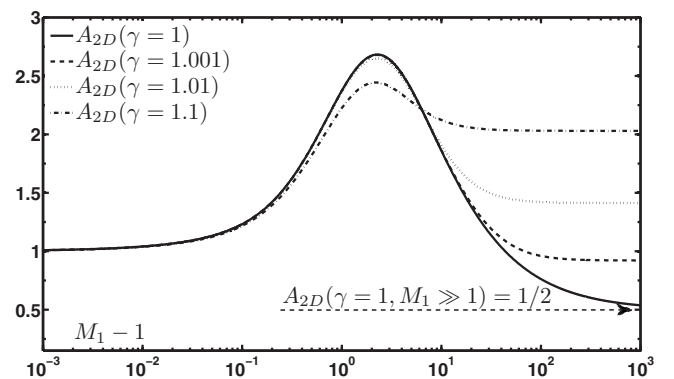


FIG. 33. Highly compressible limit ( $\gamma=1$ ) of the 2D kinetic-energy amplification factor [Eq. (195)], together with other curves corresponding to different  $\gamma$  values.

$$\begin{aligned}
A_{2D}^l(\gamma=1, M_1) \cong & -\frac{(M_1^2-1)^{7/2}}{\pi M_1^2(M_1^2+1)(M_1^4+M_1^2-1)} + \frac{8M_1(M_1^2-1)}{\pi(M_1^2+1)^2} \ln(M_1 + \sqrt{M_1^2-1}) \\
& + \frac{(M_1^8+14M_1^6-6M_1^4-2M_1^2+1)}{\pi M_1^4(M_1^2+1)^2} \tan^{-1}\left(\frac{\sqrt{M_1^2-1}}{M_1^2}\right), \tag{192}
\end{aligned}$$

$$\begin{aligned}
A_{2D}^s(\gamma=1, M_1) \cong & -\frac{(M_1^2-1)^{3/2}(7M_1^8-8M_1^6-22M_1^4+16M_1^2-1)}{\pi M_1^2(M_1^2+1)^3(M_1^4+M_1^2-1)} + \frac{2(M_1^{10}+2M_1^8-12M_1^6-8M_1^4+19M_1^2-6)}{M_1(M_1^2+1)^4\sqrt{M_1^4+M_1^2-1}} \\
& + \frac{8(M_1^2-1)(M_1^6-3M_1^4-5M_1^2+3)}{\pi M_1(M_1^2+1)^4} \ln(M_1 + \sqrt{M_1^2-1}) \\
& + \frac{(M_1^{12}-8M_1^{10}+15M_1^8+48M_1^6-49M_1^4+8M_1^2+1)}{\pi M_1^4(M_1^2+1)^4} \tan^{-1}\left(\frac{M_1^2}{\sqrt{M_1^2-1}}\right) \\
& + \frac{32M_1^6}{\pi(M_1^2+1)^4} \tan^{-1}\left(\sqrt{\frac{M_1+1}{M_1-1}}\right), \tag{193}
\end{aligned}$$

$$\begin{aligned}
A_{2D}^{ac}(\gamma=1, M_1) \cong & -\frac{4(M_1^8+16M_1^6+14M_1^4-16M_1^2+1)}{\pi(M_1^2-1)^{3/2}(M_1^2+1)^2(M_1^4+M_1^2-1)} - \frac{8M_1(M_1^4+3M_1^2-2)(M_1^4-3)}{(M_1^2-1)^2(M_1^2+1)^3\sqrt{M_1^4+M_1^2-1}} \\
& + \frac{4(M_1^{10}+9M_1^8-2M_1^6-34M_1^4+9M_1^2+1)}{\pi M_1^2(M_1^2-1)^2(M_1^2+1)^3} \tan^{-1}\left(\frac{M_1^2}{\sqrt{M_1^2-1}}\right) \\
& + \frac{32M_1(2M_1^4+3M_1^2-3)}{\pi(M_1^2-1)^2(M_1^2+1)^3} \ln(M_1 + \sqrt{M_1^2-1}). \tag{194}
\end{aligned}$$

Collecting and rearranging the above formulas, we get for the total amplification coefficient in the limit of highly compressible gases,

$$\begin{aligned}
A_{2D}(\gamma=1, M_1) \cong & -\frac{4(2M_1^{12}-7M_1^{10}+23M_1^8+44M_1^6-30M_1^4+3M_1^2-3)}{\pi(M_1^2-1)^{3/2}(M_1^2+1)^3(M_1^4+M_1^2-1)} \\
& + \frac{2(M_1^{14}-4M_1^{12}-31M_1^{10}+26M_1^8+79M_1^6-40M_1^4+7M_1^2-6)}{M_1(M_1^2-1)^2(M_1^2+1)^4\sqrt{M_1^4+M_1^2-1}} - \frac{M_1^8+14M_1^6-6M_1^4-2M_1^2+1}{2M_1^4(M_1^2+1)^2} \\
& + \frac{32M_1^6}{\pi(M_1^2+1)^4} \tan^{-1}\left(\sqrt{\frac{M_1+1}{M_1-1}}\right) + \frac{4(5M_1^{12}-20M_1^{10}-17M_1^8+72M_1^6-9M_1^4+4M_1^2-3)}{\pi M_1^2(M_1^2-1)^2(M_1^2+1)^4} \tan^{-1}\left(\frac{M_1^2}{\sqrt{M_1^2-1}}\right) \\
& + \frac{8(2M_1^{12}-7M_1^{10}+13M_1^8+30M_1^6-20M_1^4+M_1^2-3)}{\pi M_1(M_1^2-1)^2(M_1^2+1)^4} \ln(M_1 + \sqrt{M_1^2-1}). \tag{195}
\end{aligned}$$

In Fig. 33 we show a plot of the limiting curve for highly compressible gases as a function of  $M_1$  together with other  $\gamma$  values, near unity. Finally, we show the weak-shock limit for arbitrary  $\gamma$ ,

$$A_{2D}(\gamma, M_1-1 \ll 1) \cong 1 + \frac{32\sqrt{2}}{15\pi(\gamma+1)^2} \sqrt{M_1-1} + O(M_1-1). \tag{196}$$

#### IV. SUMMARY

A linear theory analytical model has been presented that studies the interaction of a planar shock wave with a random vorticity field. The turbulent spectrum is assumed to be isotropic and full account of the gas compressibility is taken. At first, the much simpler problem of the interaction with a single-mode 2D perturbation upstream is considered. It serves as a natural building block with which to construct later on the more complex 3D model. The wave equation in the compressed fluid is linearized and is exactly solved for the case in which the shock travels isolated into the turbulent fluid. The Rankine-Hugoniot equations are linearized and closed-form exact analytical expressions are derived for the quantities of interest: the shock pressure perturbations, the shock ripple corrugation, and the downstream rotational velocity components, as well as the vorticity in the compressed fluid. The sound waves emitted by the corrugated shock front are analyzed in detail. It has been found that the boundary that separates the initially quiescent fluid with the turbulent half-space is subject to RMI instability growth, once the shock enters the turbulent region. The detailed evolution of that instability is given together with the asymptotic value of its rate of growth. The interaction with a full spectrum of 3D modes is considered, assuming that the shock interacts independently with each single mode. The best way to characterize the upstream spectrum consists in decomposing it as a superposition of shear waves. Each shear wave defines a plane on which rotational/incompressible velocity perturbations are prescribed, with a given wave-number vector  $\vec{k}$ . The shear wave plane can be described in space in terms of the angles that specify the orientation of the vector  $\vec{k}$  in front of the shock. By properly rotating the coordinate axis, to exploit the isotropy of the upstream perturbations, all the important statistical averages can be easily calculated integrating over the solid angle defined by  $\vec{k}$ . In this way, explicit analytic expressions in terms of elementary functions of  $\gamma$  and  $M_1$  are derived. The results of the model presented here compare very well with the experimental/numerical data available in the published literature [30,35,40]. It is found that in some limiting regions of the parameter space ( $\gamma \rightarrow 1, M_1 \rightarrow \infty$ ), the turbulent kinetic energy is actually reduced. This apparently paradoxical result is understood with the tools developed in the 2D model: the more compressible the fluid and the stronger the shock, the more shock ripple amplitude decreases, decaying to zero, which means that the longitudinal motion (normal to the shock) is suppressed downstream. Hence, only 2/3 of the initial kinetic energy is passed as kinetic translational energy into the compressed fluid. The sound energy radiated by the shock is fully discussed in both the shock and compressed fluid reference frames. The predictions of the model for the sonic strength emitted downstream are compared quite well with previous results obtained by Ribner [17]. A detailed discussion of the dependence of the sonic flux on the shock strength in the very weak-shock limit

for is presented, highlighting the partial agreement and/or disagreement with the previous estimates of Lighthill and Ribner [13,17]. The amplification of the transverse vorticity is calculated, and its behavior as a function of  $\gamma$  and  $M_1$  is studied. Good agreement with previous direct numerical simulations [30] is observed. The exact analytic asymptotic expressions for the vorticity amplification factor are derived in the strong/weak-shock limits, and for highly compressible fluids. An anisotropy parameter is defined, in order to see how much the shock alters the upstream isotropy of the velocity perturbations. It is found that for some regions in the parameter space the velocity field may remain isotropic after shock/turbulence interaction. However, the compressed vorticity perturbations are always laterally anisotropic, with their vectors pointing essentially parallel to the shock surface. This is because the shock/turbulence interaction shortens, by a factor  $1/R$ , the characteristic length of the upstream eddies in the direction normal to the shock surface. This effect is stronger for stronger shocks and highly compressible gases. Finally, the same model is applied to a much simpler spectrum, consisting of isotropic random perturbations in 2D. The agreement with existing numerical simulations [19] is also very good. All the statistical averages shown in this work can be calculated with exact analytical functions of the governing parameters (gas compressibility and shock strength). Exact asymptotic formulas can be derived to study those quantities in the physical limits of weak shock, strong shock, and highly compressible gases.

It is clear that the calculations shown here can be used to deal with other types of interaction (which have also been studied previously in the published literature): such as the interaction with an isotropic spectrum of density/entropy perturbations ahead of the shock, or with a random field of acoustic waves. The potential of the model developed here is the possibility of getting exact analytical scaling laws. This fact is quite important, as it may be certainly useful to the scientific community working on similar problems which use sophisticated hydrodynamic simulation codes. The model may also be extended to deal with more complicated boundary conditions downstream, such as the presence of a true piston, reflecting the sound waves from behind toward the shock. Besides, it might also be possible to apply this formalism to study the effect of a second shock launched into the compressed turbulent spectrum.

#### ACKNOWLEDGMENTS

The authors would like to thank G. Dimonte (LANL) for suggesting this problem and for very useful discussions during the development of the work. J.G.W. and C. H.R. de L. have received support from MEC under Grant No. FIS2006-05389 and JCCM under Grant No. PAI08-0182-3162 from Spain. C. H. de L. acknowledges support from UCLM Contract 2007-COB-1744, from MICINN (Spain) AP2007-02745, and a Grant No. (AT20091285) from UCLM. A.L.V. has received support from DoE, USA.

- [1] A. E. Roberts, Los Alamos Scientific Laboratory Report No. LA-299 (unpublished). See National Technical Information Service Document No. PB2004-100597.
- [2] N. C. Freeman, Proc. R. Soc. London, Ser. A **228**, 341 (1955).
- [3] S. P. Dyakov, Zh. Eksp. Teor. Fiz. **27**, 288 (1954).
- [4] V. M. Kontorovich, Akust. Zh. **5**, 324 (1959).
- [5] P. M. Zaidel, J. Appl. Math. Mech. **24**, 316 (1960).
- [6] Iu. M. Nikolaiev, J. Appl. Math. Mech. **29**, 785 (1965).
- [7] R. D. Richtmyer, Commun. Pure Appl. Math. **13**, 297 (1960).
- [8] E. E. Meshkov, Fluid Dyn. **4**, 101 (1969).
- [9] M. G. Briscoe and A. A. Kovitz, J. Fluid Mech. **31**, 529 (1968).
- [10] G. Fraley, Phys. Fluids **29**, 376 (1986).
- [11] N. J. Zabusky, Annu. Rev. Fluid Mech. **31**, 495 (1999).
- [12] F. K. Moore, Natl. Advis. Comm. Aeronaut, Report 1165 (1953).
- [13] M. Lighthill, Proc. Cambridge Philos. Soc. **49**, 531 (1953).
- [14] H. S. Ribner, Natl. Advis. Comm. Aeronaut, Report 1164(1954).
- [15] H. S. Ribner, Natl. Advis. Comm. Aeronaut, Report 1233 (1954).
- [16] H. S. Ribner, AIAA J. **25**, 436 (1987).
- [17] H. S. Ribner, J. Fluid Mech. **35**, 299 (1969).
- [18] J. L. Kerrebrock, Ph.D. thesis, California Institute of Technology, 1956.
- [19] D. Rotman, Phys. Fluids A **3**, 1792 (1991).
- [20] K. Mahesh, S. Lee, S. K. Lele, and P. Moin, J. Fluid Mech. **300**, 383 (1995).
- [21] K. Mahesh, Ph.D. thesis, California Institute of Technology, 1996.
- [22] Y. Andreopoulos, J. H. Agui, and G. Briassulis, Annu. Rev. Fluid Mech. **32**, 309 (2000).
- [23] A. L. Velikovich, J. G. Wouchuk, C. Huete Ruiz de Lira, N. Metzler, S. Zalesak, and A. J. Schmitt, Phys. Plasmas **14**, 072706 (2007).
- [24] S. B. Berndt, J. Fluid Mech. **26**, 433 (1966).
- [25] W. D. Hayes, J. Fluid Mech. **2**, 595 (1957).
- [26] C. Truesdell, J. Aeronaut. Sci. **19**, 826 (1952).
- [27] N. K.-R. Kevlahan, J. Fluid Mech. **327**, 161 (1996).
- [28] N. K.-R. Kevlahan, J. Fluid Mech. **341**, 371 (1997).
- [29] F. Ducros, V. Ferrand, F. Nicoud, C. Weber, D. Darracq, C. Gacherieu, and T. Poinso, J. Comput. Phys. **152**, 517 (1999).
- [30] S. Lee, S. K. Lele, and P. Moin, J. Fluid Mech. **340**, 225 (1997).
- [31] K. Mahesh, S. K. Lele, and P. Moin, J. Fluid Mech. **334**, 353 (1997).
- [32] S. Lee, S. K. Lele, and P. Moin, J. Fluid Mech. **251**, 533 (1993).
- [33] K. Sinha, K. Mahesh, and G. V. Candler, Phys. Fluids **15**, 2290 (2003).
- [34] G. H. Miller and T. J. Ahrens, Rev. Mod. Phys. **63**, 919 (1991).
- [35] G. Dimonte and R. Tipton, Phys. Fluids **18**, 085101 (2006).
- [36] G. Palma, A. Mignone, M. Vietri, and L. Del Zanna, Astrophys. J. **686**, 1103 (2008).
- [37] L. D. Landau and E. M. Lifshitz, *Fluid Mechanics* (Pergamon, New York, 1987).
- [38] O. Schilling, M. Latini, and W. S. Don, Phys. Rev. E **76**, 026319 (2007).
- [39] J. Keller and W. Merzkirch, Exp. Fluids **8**, 241 (1990).
- [40] S. Barre, D. Alem, and J. P. Bonnet, AIAA J. **34**, 968 (1996).
- [41] L. Jacquin, C. Cambon, and E. Blin, Phys. Fluids A **5**, 2539 (1993).
- [42] H. S. Ribner, AIAA J. **36**, 494 (1998).
- [43] S. Barre, D. Alem, and J. P. Bonnet, AIAA J. **36**, 495 (1998).
- [44] G. Hazak, A. L. Velikovich, J. H. Gardner, and J. P. Dahlburg, Phys. Plasmas **5**, 4357 (1998).
- [45] A. D. Kotelnikov and D. C. Montgomery, Phys. Fluids **10**, 2037 (1998).
- [46] A. Y. Poludenko, A. Frank, and E. G. Blackman, Astrophys. J. **576**, 832 (2002).
- [47] B. Canaud, F. Garaude, P. Ballereau, J. L. Bourgade, C. Clique, D. Dureau, M. Houry, S. Jaouen, H. Jourden, N. Lecler, L. Masse, A. Masson, R. Quach, R. Piron, D. Riz, J. Van der Vliet, M. Temporal, J. A. Delettrez, and P. W. McKenty, Plasma Phys. Controlled Fusion **49**, B601 (2007).
- [48] A. L. Velikovich, Phys. Fluids **8**, 1666 (1996).
- [49] A. L. Velikovich, J. P. Dahlburg, A. J. Schmitt, J. H. Gardner, L. P. Phillips, F. L. Cochran, Y. K. Chong, G. Dimonte, and N. Metzler, Phys. Plasmas **7**, 1662 (2000).
- [50] J. G. Wouchuk and K. Nishihara, Phys. Plasmas **3**, 3761 (1996).
- [51] J. G. Wouchuk, Phys. Rev. E **63**, 056303 (2001).
- [52] J. G. Wouchuk and J. Lopez Cavada, Phys. Rev. E **70**, 046303 (2004).
- [53] D. Zwillinger, *Handbook of Integration* (Jones and Bartlett, Boston, 1992).
- [54] W. R. LePage, *Complex Variables and the Laplace Transform for Engineers* (Dover, New York, 1980).
- [55] B. Davies, *Integral Transforms and their Applications* (Springer, New York, 1984).
- [56] I. S. Gradshteyn and I. M. Ryzhik, *Table of Integrals, Series, and Products*, 5th ed. (Academic, San Diego, 1994).
- [57] See EPAPS Document No. E-PLLEE8-79-060906 for the Appendices to this work. For more information on EPAPS, see <http://www.aip.org/pubservs/epaps.html>.
- [58] L. D. Landau and E. M. Lifshitz, *Mechanics*, 2nd ed. (Butterworth-Heinemann, Oxford, 2000).
- [59] H. Goldstein, *Classical Mechanics* (Addison-Wesley, Reading, 1980).